Data Acquisition, Event Building and Signal Reconstruction for Compton Camera Imaging

Vom Fachbereich Elektrotechnik und Informatik
der Universität Siegen
zur Erlangung des akademischen Grades

Doktor der Ingenieurwissenschaften
(Dr.-Ing.)

genehmigte Dissertation

von

Dipl.Ing. Kıvanç Nurdan
geb. am 25. Nov. 1969 in Adana, Türkei

Tag der mündlichen Prüfung: 16.Februar.2006
urn:nbn:de:hbz:467-2115

1. Gutachter: Prof.Dr.rer.nat. habil. Albert Heinrich Walenta
2. Gutachter: Prof.Dr.-Ing. habil. Otmar Loffeld
Vorsitzender: Prof.Dr.-Ing. habil. Bernd Freisleben

To my dearest love and wife Tuba
my precious light Nurperi
and my parents Doğan and Günal Nurdan.

Zusammenfassung

Die Compton-Camera ist ein neues Detektorsystem zur bildlichen Darstellung von radioaktiven Markierungssubstanzen im Bereich der Gammastrahlung, das prinzipiell eine besonders gute Ortsauflösung und hohe Empfindlichkeit liefern kann. Die ist von grosser Bedeutung für die moderne bio-medizinische Forschung oder für darauf basierende diagnostische Verfahren.

Dafür ist ein neues Konzept einer software-basierten Koinzidenzmessung entwickelt worden, das auf den bereits vorhandenen Datenaufnahmesystemen der Hochenergiephysik aufbaut, bei denen die Information von mehreren Tausend Kanälen von verschiedenen Detektortypen zusammengefügt werden. Auf der Basis der Digitalisierung analoger Signale durch FADCs (flash analog to digital converters), einer modernen Struktur einer ersten Stufe von Prozessoreinheiten, realisiert durch FPGAs (field programmable gate arrays) und einer erweiterbaren schnellen Busstruktur, wurde ein System aufgebaut, bei dem die Signale von einem 19-kanaligen Streudetektor und einem Absorptionsdetektor (Anger-Camera) eindeutig zusammengefügt werden konnten. Die Verwendung von Zeitmarkierungen spielte dabei eine zentrale Rolle, um die Zuordnung der Signale der Detektorkomponenten von der asynchronen Erzeugung in den synchronen Teil der weiteren Verarbeitung zu erhalten. Mit diesem Datenaufnahmesystem ist es erstmals gelungen, Signale von Silizium-Drift Detektoren, die durch Compton-Elektronen erzeugt wurden, und Signale des gestreuten Gamma-Quanten, die in dem zweiten Absorptionsdetektor erzeugt werden, zu Paaren zusammenzusetzen und damit die Streuereignisse zu rekonstruieren, wobei eine Winkelgenauigkeit von etwa 1° erreicht wurde. Diese Genauigkeit liegt nahe an dem theoretisch erwarteten Wert.

Bisher gab es keine Anhaltspunkte über den Einfluss eines Prozessors auf die erzielte Qualität bei einer Bildaufnahme. Der übliche Weg über die Beschreibung einer "Detective Quantum Efficiency" (DQE) wurde daher auf diesen Prozess erweitert. Dazu wurden mit Hilfe des Monte-Carlo-Verfahrens Simulationen mit Zeitmarken über das Totzeitverhalten dieses "software"-basierten Koinzidenzsystems durchgeführt.

Es konnte gezeigt werden, dass das neue System sich im Wesentlichen so verhält, als würde es durch eine "paralysierende" Totzeit bei höheren Raten limitiert. Genauere Untersuchungen zeigen, dass dafür die Zeitdauer zur Verarbeitung eines Ereignisses in dem Prozessor und die Tiefe des Puffers massgebend sind , was für spätere Echtzeitanwendungen und Weiterentwicklungen von Bedeutung ist. Die zur Zeit verfügbare neuester Generation von Prozessoren sind aber durchaus in der Lage ohne allzu grosse Verluste den Anforderungen eines komplexen Detektors zu genügen.

Abstract

The Compton camera is a new detector system for imaging radioactively labeled nuclides in the range of γ-rays that can in principle provide extremely good resolution and high sensitivity. This is invaluable for the modern bio-medicine research or diagnostic studies based on it.

For this system a new concept of software based coincidence measurements has been developed; inspired by the data acquisition systems built for high energy physics, where the information from thousands of channels of various detectors has to be merged. A data acquisition system based on digitizing analog signals with FADCs (flash analog to digital converters) has been built consisting of a modern structure of first level processor unit realized with FPGAs (Field Programmable Gate Arrays) and an extendable fast data bus. The developed data acquisition system is capable of collecting the signals from a 19-channel scatter detector and an absorption detector (Anger camera) unambiguously. Here the usage of time stamping plays a central role in order to attribute the asynchronous signals of detector components to synchronous event fragments for further processing. With this data acquisition system it is shown for the first time that the signals from the silicon drift detector that are generated through Compton electrons and signals of scattered gamma quants produced in the second absorption detector can be put in pairs to reconstruct scattering events where an angular resolution of approximately 1° is achieved. This precision is close to the theoretically expected value.

There has been no clue on the influence of a processor on the quality of the image acquisition till now. The usual way of defining "Detective Quantum Efficiency" (DQE) has been enhanced to this process. For this purpose, Monte Carlo simulations with time stamps over the deadtime relation of this software based coincidence system have been performed.

It could be shown that this new system behaves as if it was limited with a paralyzable deadtime at high rates. More detailed analysis shows that the duration of processing an event in the processor and the depth of the buffers are decisive parameters that are for future real-time applications and further development essential. However, today's available newest generation processors have the performance of fulfilling the requirements of complex detectors without considerable losses.

Contents

Chapter 1

Introduction

This dissertation is focused on the development of a novel data acquisition system, signal and event reconstruction for the prototype Compton camera constructed at the University of Siegen. The camera system was designed to investigate new methods to increase the performance of the Compton camera imaging.

Medical Imaging has grown to be a major part of medical practice during the past century. Unlike 100 years ago when x-ray diagnosis first appeared, there is now a palette of different techniques available which effectively cope with diverse problems that need to be dealt with. In any case the supreme objective is to produce medical images with as much functional and anatomical information as possible which permits the medical doctors to make their diagnosis in individual cases, to evaluate the impact of therapy, and permit screening of large populations, some of whom are affected with serious diseases (e.g. cancer). Moreover, medical imaging plays an increasingly vital role in medical research and in the development and testing of new pharmaceuticals.

All this requires a diversity of imaging systems, each of which provide different unique kinds of information with varying degrees of precision. In many cases they act in a complimentary way, as will be explained below.

Today, there are four major groups of imaging techniques used in clinical applications: Ultrasound Imaging, Magnetic Resonance Imaging, X-Ray Transmission Imaging, and Gamma-Ray Emission Imaging (including positron annihilations, i.e. PET and SPECT Imaging).

Ultrasound Imaging (USI): In ultrasound imaging high frequency acoustic waves are sent into the patient's body. They are reflected partially and the reflected waves are recorded together with the elapsed time with respect to the emission time. The degree of reflection depends on the kind of a tissue. Together with the recorded time of propagation of the acoustic waves, one obtains images of organs and parts of organs. USI has the advantage of being non-invasive, but its spatial resolution is limited. In particular it is impossible to resolve different components when they are closely mixed (e.g. a small tumor in a soft tissue). Also they convey mainly an anatomic information, not a functional information (an exception is the measurement of velocities of blood in veins or artery).

Magnetic Resonance Imaging (MRI): This diagnostic radiological modality uses nuclear magnetic resonance technology, in which the magnetic nuclei (especially protons) of a patient aligned in a strong, uniform magnetic field absorb energy from tuned radio frequency pulses, and emit radio frequency signals as their excitation decays. These signals, which vary in intensity according to nuclear abundance and molecular chemical environment, are converted into sets of tomographic (selected planes) images by using field gradients in the magnetic field, which permits 3-dimensional localization of the sources of the signals. It is good for imaging anatomy and partially used for understanding physiology. MRI provides nowadays astonishingly precise anatomical information with a spatial resolution which is almost unbeatable. Recently, functional information can be extracted by either using suitable contrast agents (with paramagnetic atoms attached to it) or special techniques for blood flow measurements (e.g. BOLD MRI for measuring the blood throughput in parts of an organ). Nevertheless the functional information is still and will most likely be always limited with respect to the sensitivity achieved with emission imaging which is explained below.

Transmission Imaging: An external γ-ray-source illuminates the patient and the transmission (attenuation) of the γ-rays, while passing through the patient, are recorded by a detector. This technique is mainly used to image anatomical features. It is the oldest of the four techniques mentioned and has dramatically improved since the time of Röntgen by using more sensitive detectors, replacing the film by digital imaging devices and using contrast agents. Still, its main advantage is the fast imaging of anatomic features and irregularities whereas functional information is limited. Unlike the first two methods it is partially invasive since the patient has to be exposed to ionizing radiation.

Emission Imaging: In this technique, parts of the patient organs or certain functional parts of the body (e.g. lymph nodes, bone marrow) are labeled by applying suitable radioactive tracers. The tracer substance is chosen such that it is preferentially taken up by the organ or a functional part, which has to be investigated, i.e. imaged. After the uptake, these parts are radioactively labeled, that means they emit radiation, which is recorded by detectors around the patient and used to reconstruct the image of the radiating part (e.g. a tumor). The intensity of this emission image provides valuable additional information (e.g. an intensity of the brain activity). The other advantage is very rich functionality of this method given by the large number of tracer substances, ranging from simple colloids to various proteins to enzymes, antibodies, neurotransmitters by which the radioactivity can be directed in a very function dependent manner. It is this functional information, which makes the emission imaging indispensable despite its non-negligible invasive characteristic, due to the administrated radioactivity.

All these methods have been either developed and/or dramatically improved through the enormous developments in computer science, physics and electronics in the last four decades. Among these four groups of methods, very active and interesting research is going on in the

development of emission tomography imaging devices, since they allow one to visualize not only the anatomy of a living organism but also the physiology and metabolism processes.

Emission imaging can be divided further into two major branches:

1. Positron Emission Tomography (PET): Utilizes annihilation of positron with an electron which generates two back-to-back γ-rays. A cylindrical absorption detector captures the emitted γ-rays to reconstruct the line along which the annihilation occurs.

2. Single Photon Emission Computer Tomography (SPECT)

   - Gamma (Anger) Camera: This type of imager uses a passive collimator and an absorption detector in order to visualize incoming γ-rays from the patient. The collimator which is the weakest point of this type of camera, stops 99.99% of the incoming γ-rays and only 0.01% is used for imaging. However, it is cheap, commercially available and can be found in most of the hospitals.
   - Compton Camera : The collimator of the gamma camera is replaced by an active detector in this type of camera. The γ-rays emitted from the patient first undergo a Compton scattering in the scatter detector, which replaces the collimator and the scattered photon is absorbed in the absorption detector. The efficiency can be increased dramatically with respect to the Anger camera but imaging requires complex algorithms. The development of clinically applicable Compton camera is still ongoing.

In cancer studies, a very high spatial resolution ($x \ll 1$ mm) is required in emission imaging for early diagnosis, where even well performing PET cameras are not sufficiently effective because of their intrinsic resolution limit of $x = 1 \ldots 2$ mm due to the positron range in tissue. Therefore SPECT could be the solution to overcome this limitation. However the use of a collimator in Anger camera imposes an inverse relation between sensitivity and spatial resolution. In addition, for higher gamma energies the intrinsic position resolution of gamma detectors is limited due to the collimator septal penetration and the range of secondary radiation (fluorescence, the range of a secondary electron and Compton scattered radiation). In order to overcome the limitation imposed by the collimator, the concept of Compton coincidence imaging was introduced.

1.1 History

The history of SPECT started in the late 1940's. In 1951 Ben Cassen invented the rectilinear scanner [Cas50]. This device was using a PMT attached to a NaI(TI) crystal that was focused to a small area with a lead collimator. The area of interest then had to be scanned point-by-point. Images were recorded on a paper with a mechanical pen. The deficiency of the system was the very long imaging time because of the sequential nature of the apparatus. The invention of the Anger camera by Hal Anger in 1958 [Ang58] overcame this deficiency. This device consists of a single large NaI(TI) crystal coupled to multiple photomultiplier tubes (PMT), and a collimator containing many parallel holes whose axes are othogonal to the crystal surface. The signals

coming from the PMT's are coupled in such a way that it is possible to capture an image of the distribution of radioisotopes at once, rather than point-by-point as the rectilinear scanner had done. Later in 1963, Kuhl and Edwards presented first tomographic images produced by the Anger Camera.

Developments in radiopharmaceuticals and especially the introduction of ^{99m}Tc with a simple generator as a marker, enabled economical every-day clinical usage of Anger cameras starting from late 1960's. The primary problem with these systems is the low efficiency due to the fact that only 1 photon out of 10000 may reach the detector since only photons which are perpendicular to the collimator plane are admitted while others do not reach the detector at all. Reducing the photon energy, which may lead to a reduction of the collimator thickness, is also not favourable, as low energy photons scatter more inside the body which decreases the contrast and resolution of the images. The usage of single photon emitting tracers having energies greater than 361 keV of ^{131}I was not possible as it needs a thicker collimator and a higher patient dose. Another intrinsic problem for the Anger camera is that a stationary detector can provide only planar images and it does not deliver the information on the distance between the detector and the source. In order to get a 3-D information the camera must scan around the entire object.

A possible solution to these problems was introduced in 1973 [Sch73] in astronomy where the sources are assumed to be at nearly infinite distances. This solution incorporates one of the interactions of γ-rays with matter, namely Compton scattering, that is dominant in the gamma-ray energy range of 100 kev to 20 MeV. This range perfectly suits to the requirements mentioned above. The application of Compton scatter imaging or shortly Compton Camera (CC) to medical imaging was demonstrated in 1974 [Tod74]. *A significant difference between the CC system and the Anger camera system is that the data processing is an integral part of the γ-ray optics in the CC system.*

Singh and his co workers presented a series of papers in the 80's where they demonstrated the feasibility of the method for medical applications [Sin83, Sin84]. They focused on 140 and 662 keV energy using a High Purity Germanium (HPGe) front end scatter detector, an Anger camera as the absorption detector and developed image reconstruction methods. In 1981, Brookhaven Natioanl Laboratory (Walenta and Brill) [Wal81] proposed to build a high pressure multi wire plane gas detector as the front end detector with an Anger camera [San88, Geb90]. A collaboration between Singh and the University of Michigan has resulted in a number of important tests of different approaches. A series of papers investigate discrete counting [Mar93], and imaging probes (SPRINT) [Rog88] surrounding a central scatter detector. Much attention has been given to the mathematically challenging image reconstruction problems [Sau98]. The University of Michigan has pursued an intensive series of investigations simulating the expected results using pixelated front end detectors and anger type logic in the cylindrical geometry of the SPRINT system. The clinical imaging initially directed at low energy nuclides (140-392 keV), and sources embedded in patients (10-15 cm depth). The results are described in contemporary theses of students in this program [LeB99, Hua00a]. Despite all these efforts, no camera system, completely fulfilling clinical requirements concerning efficiency and resolution, has been developed by now.

1.2 Problem Definition & Objectives

The crucial difference of the CC method to all other imaging methods lies in the fact that a complex event caused by the emitted quanta has to be kinematically reconstructed.

As we look at the history of the Compton camera systems and their possible application to medical imaging, several possible problems have been encountered in designing a system involving a typical reaction pattern consisting two or more newly generated quanta. The salient features of such a system can be summarized as follows:

- Detector Systems and Data Acquisition System: This can be very complicated for a given Compton camera system. In order to capture Compton interactions where two different detector systems with different requirements are needed, and will be described in greater detail in the next chapter. In the first detector the incoming photons interact with the atomic electrons of the detector material and scatter. In the second detector, these scattered photons need to be absorbed.

  One should also consider that due to the probabilistic nature of the interactions of photons and electrons with matter, multiple events may occur in both detectors. In addition, cosmic rays and other types of radiation may contribute to these unwanted events. If it is not possible to make use of these multiple events, they should be identified and eliminated .

- Event Reconstruction: The events coming from different detectors should be analysed and Compton event candidates should be selected as quickly as possible in order to reduce unnecessary data transmissions to the data processing unit.

- Image Reconstruction: This is also a very complex problem, as the geometry of the detector system has an influence on the image reconstruction. Recently it has been shown that it is mathematically possible to solve the image reconstruction problem directly with filtered backprojection methods for some detector geometries [Gun03].

All of these problems mentioned above are inherently coupled to each other. Any system designer working on the image reconstruction should be aware of all these aspects. For example, the direct reconstruction is mathematically possible and is proven to work for a spherical Compton camera system where the camera surrounds the object to be imaged, but it is not feasible to build a fully spherical Compton camera system practically and commercially. Instead we will pursue the concept of building a planar primary detector and hemispherical secondary detector.

In order to describe the performance of a complex recording system as the Compton camera, the performance of a single detector concept such as the signal to noise ratio or the time resolution will not be useful. A system performance measure including the event reconstruction efficiency is required. In this thesis the above technique is proposed and it is shown in detail that the concept of "Detective Quantum Efficiency" (DQE) is appropriate performance measure for such a system.

The DQE is defined as;

$$\mathrm{DQE} = \left(\frac{(SNR)_{\mathrm{output}}}{(SNR)_{\mathrm{input}}} \right)^2$$

where SNR denotes the signal to noise ratio. In nuclear medicine the input of the imaging system is given by the intensity of complex nuclear decays and the output is mainly given by the counting statistics and event reconstruction of a clean dataset. In order to compare the precision of different imaging systems, DQE provides a system-independent measure. This concept has been used for presenting the theoretically calculated, experimentally measured and simulated results. There are two types of problems for any given coincidence system.

- Random Coincidences: This problem can be overcome only partially by making the coincidence window as small as possible

- Deadtime: This is a combined parameter of a detector system and its readout electronics, which can not be made smaller than the underlying physics process governing the signal generation.

With complex detectors used in Compton camera systems, it is not possible to use simple hardware coincidence method to record the events, especially for high rate applications. This problem can be solved by digitizing, time stamping and digitally processing the coincidence events online. To achieve this, a data acquisition system that captures, digitizes and time stamps events from different detector systems asyncronously, followed by a buffered pipelined digital coincidence processing system, has been designed and implemented for the Compton camera prototype. An asynchronous time coincidence data acquisition concept has been developed where event fragments from different detectors are time stamped and buffered for further processing. The hardware design is based on field programmable gate arrays (FPGA) and the reprogrammable nature of the hardware enables the testing of different configurations. This thesis focuses on the design and construction of this data acquisition system.

With this system data fusion from two different detector components of the Compton camera has been accomplished. A soft processor is implemented in VHDL (Very High Speed Integrated Circuits Hardware Description Language) as a proof of concept which eases implementation of processes that are not time critical; like buffer allocation, initiation of data transfers and communication with the remote data acquisition computer. A system simulator is developed for predicting the scalability of the developed system. Upper processing limit of the system is extrapolated using the design parameters.

Measurements and final reconstruction results are presented for the data gathered with low rate prototype. Monte-Carlo (MC) simulations have been performed using the algorithmic model of the data acquisition system. Finally MC models for two complex detectors have been developed and the results are discussed.

1.3 Organization

The thesis is organized as follows. In Chapter 2, the necessary theoretical background is given, in Chapter 3 an overview of the Compton camera prototype hardware is given, describing the essential features of the components that are being used. Chapter 4 is devoted to the data acquisition system which has been developed for the prototype Compton camera system. Full details of the system, the manifold studies and tests are given in this chapter. The study of the dead time with some Monte Carlo simulation results is discussed in Chapter 5. This chapter covers also the discussion and extension of the Monte Carlo simulation for different detector types and it is followed by Chapter 6 where conclusions and a future project are discussed.

Chapter 2

Theoretical Background

This chapter provides an overview of theoretical concepts required for developing a Compton camera prototype. The Compton effect and the physics behind it will be presented in the first part. Then the image reconstruction is introduced followed by the discussion of the imaging process, its connection to single photon counting systems and coincidence systems. Finally, dead-time concept and its application to coincidence measurements are summarized.

The radio-pharmaceuticals emitting γ-rays in the energy range of 100 keV to 3 MeV are especially interesting for medical imaging due to the minimal interaction within the body which results in the usage of most of them for imaging. Unfortunately, it is not possible to focus γ-rays for imaging as one can do with electromagnetic radiation in the visible range using lenses. In order to overcome this difficulty, thick collimators are used traditionally. The geometry of the collimator determines the direction of the incoming γ-rays. In Fig. 2.1 a sketch of an Anger camera with a parallel hole collimator is presented which demonstrates the idea of a collimation.

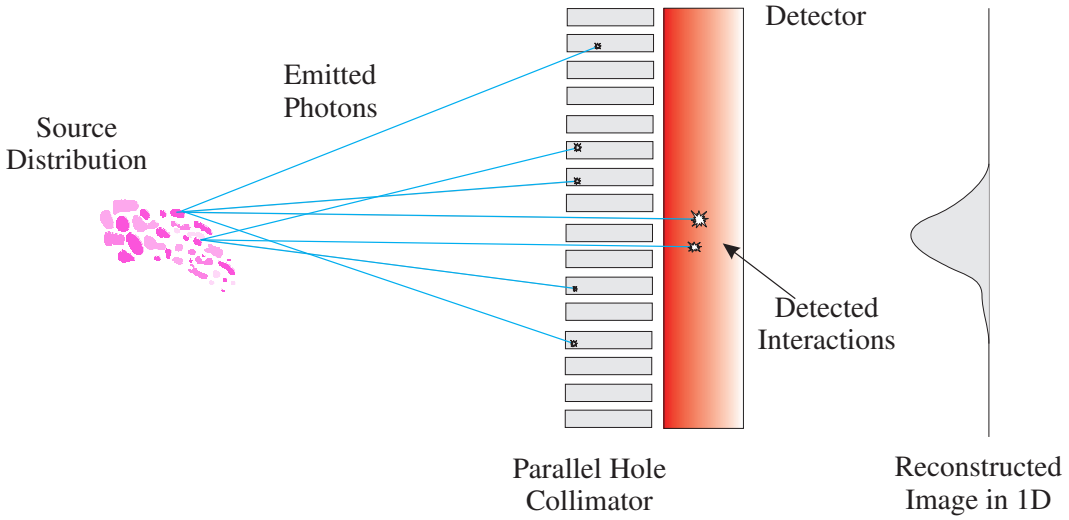

Fig. 2.1: Operation principle of the Anger camera

Materials with high atomic numbers like lead or tungsten are used commonly for collimators due to their high photo-absorption capability. Major deficiencies of Anger cameras can be

summarized as follows:

- Most of the γ-rays emitted by the source can not be used for imaging due to their absorption in the collimator. The efficiency of a typical Anger camera is of the order of 10^{-4}, which corresponds to the ratio of the detected γ-rays to the total number of emitted γ-rays.
- The resolution of the image is limited by the hole diameter of the collimator.
- The spatial resolution improves only at the expense of reduced efficiency as follows:

$$g \propto R_c^2 \tag{2.1}$$

  where g is the geometrical efficiency and R_c is the collimator spatial resolution .
- The useful energy range, in which the Anger camera can be used, is limited by the thickness of the collimator.

Despite these deficiencies, Anger cameras became the instrument of choice for radioisotope imaging since their invention in 1950's.

A better way of *focusing* γ-rays may be achieved by using a well known phenomenon, the Compton scattering of γ-rays, where a kinematical relation allows an angular measurement of the incoming γ-ray . It transfers some of its energy to an electron which results in a change of its direction as it traverses the material. Although it is not possible to control the scattering angle of γ-ray one can make use of it by having two detector components; namely the scatter detector and the absorption detector. A photon emitted from a source undergoes Compton scattering in the scatter detector, where the recoil electron is absorbed and its energy and the location of interaction are determined. The scattered photon leaves the scatter detector and is absorbed in the absorption detector, where the energy and impact position are determined. From this information the source of the incident photon is found to lie on the surface of a cone which is called the backprojected cone. By using this data and image processing techniques, the incoming direction of the original photon is found to be located on the surface of a cone. The location of the source can be determined by the intersection of cones at a certain location when many such events are collected. The principle of operation of the Compton camera is presented in Fig. 2.2.

2.1 Compton Scattering

For photon energies between 100 keV and a few MeV the dominant interaction is the Compton scattering , which is described by the scattering of photons off quasi-free electrons:

$$\gamma + e \rightarrow \gamma' + e' \tag{2.2}$$

The kinematics of Compton scattering is presented in Fig. 2.3. All particles participated in this interaction lie on the same plane.

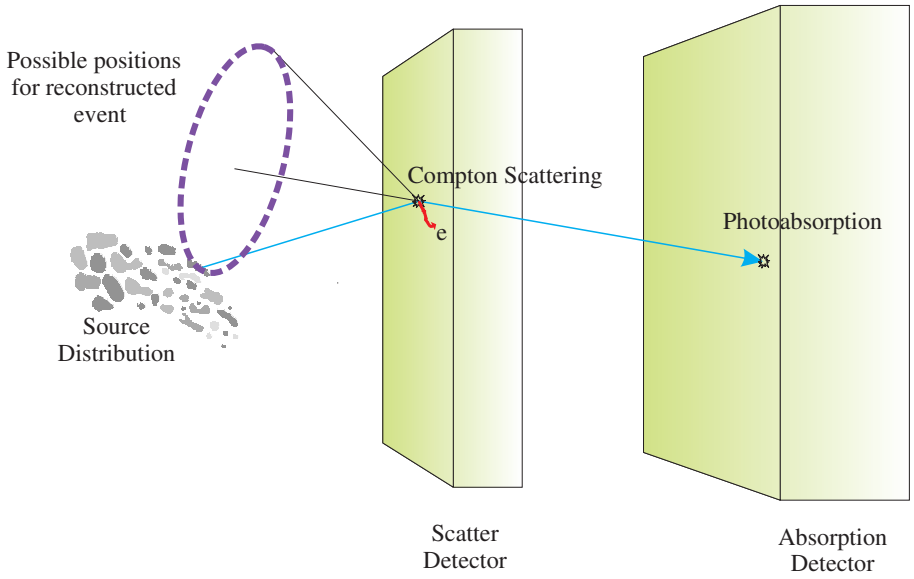

Fig. 2.2: Operation principle of the Compton camera

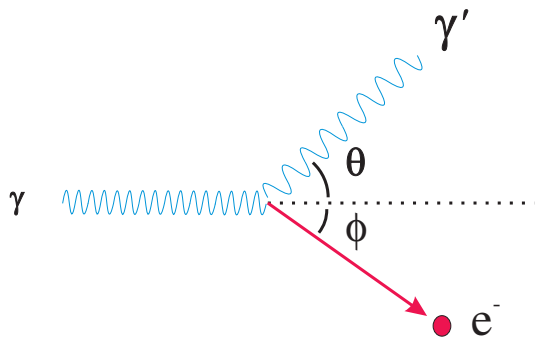

Fig. 2.3: Compton Scattering

The energy of the scattered photon can be calculated using the formula below,

$$E_{\gamma'} = \frac{E_\gamma}{1 + \epsilon(1 - \cos\theta)} \tag{2.3}$$

where E_γ is the energy of the incoming photon, $E_{\gamma'}$ is the energy of the scattered photon, θ is the scattering angle of the incoming photon and ϵ is the reduced photon energy defined as $\epsilon = \frac{E_\gamma}{m_e c^2}$ with $m_e c^2$ being the rest mass of the electron. The derivation of this formula is presented in Appendix A. A more useful formula for determining the Compton scatter angle can be derived using this equation which is given as:

$$\theta = \arccos\left(1 - \frac{E_e}{E_\gamma - E_e} \times \frac{1}{\epsilon}\right) \tag{2.4}$$

where E_e is the kinetic energy of the scattered (recoil) electron. This equation is very important for Compton camera systems, where the energy of the recoil electron can be used to determine the scattering angle.

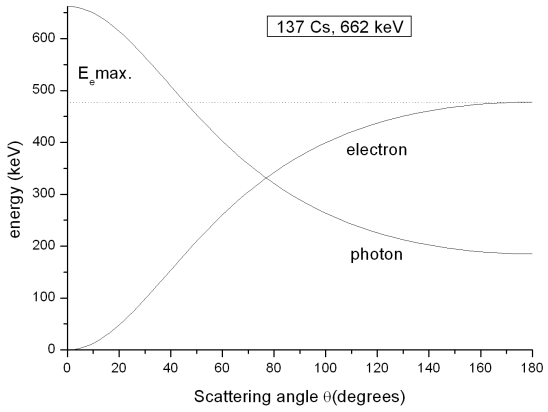

Fig. 2.4: The distribution of scattered photon and recoil electron energies as a function of the scattering angle for ^{137}Cs source emitting photons of 662 keV energy

In Eq. 2.4, setting θ to π maximizes the energy transfer to the electron which can be written as:

$$E_{e_{\max}} = \frac{2\epsilon^2}{1+2\epsilon} m_e c^2 \tag{2.5}$$

This energy corresponds to the *Compton edge*. Typical curves for absorbed photon energy and recoil electron energy with respect to Compton scattering angle for ^{137}Cs is plotted in Fig. 2.4. The Compton edge energy for this source is around 477 keV.

The discovery of the Compton scattering effect is an important event in the history of modern physics. At a time (early 1920's) when the particle (photon) nature of light suggested by the photoelectric effect was still being debated, the Compton experiment gave clear and independent evidence of the particle-like behavior. The final evidence for this hypothesis was obtained by Compton when he observed the track of the ejected electron in a cloud chamber. An earlier experiment of Geiger and Bethe had shown that the scattered photon and the ejected electron came from the same scattering process. They applied for the first time the coincidence measurements using fast "Geiger" counters. It provided the confirmation of the validity of Planck's quantum hypothesis that electromagnetic radiation came in discrete massless packets with an energy that is proportional to the frequency. Compton was awarded the Nobel Prize in 1927 for the discovery of this effect named after him.

In 1929 Klein and Nishina calculated the angular distribution of the Compton scattering and this was one of the first applications of quantum electrodynamics (QED). The differential cross section for Compton scattering defined by the scattering angle θ per solid angle is given by;

$$\frac{\partial \sigma_c}{\partial \Omega} = \frac{r_e^2}{2} \frac{1}{[1+\epsilon(1-\cos\theta)]^2} \left[1 + \cos^2\theta + \frac{\epsilon^2(1-\cos\theta)^2}{1+\epsilon(1-\cos\theta)} \right] \tag{2.6}$$

where ϵ is the reduced photon energy and r_e is the classical electron radius, which is equal to $e^2/4\pi\epsilon_0 m_e c^2 = 2.818 \cdot 10^{-15}$ m. By integration over the whole 4π solid angle, the total cross

section;

$$\sigma_c = 2\pi r_e^2 \left[\left(\frac{1+\epsilon}{\epsilon^2} \right) \left\{ \frac{2(1+\epsilon)}{1+2\epsilon} - \frac{1}{\epsilon} \ln(1+2\epsilon) \right\} + \frac{1}{2\epsilon} \ln(1+2\epsilon) - \frac{1+3\epsilon}{(1+2\epsilon)^2} \right] \; [cm^2/electron] \tag{2.7}$$

is obtained. This cross section assumes an unpolarized γ-ray at the input.

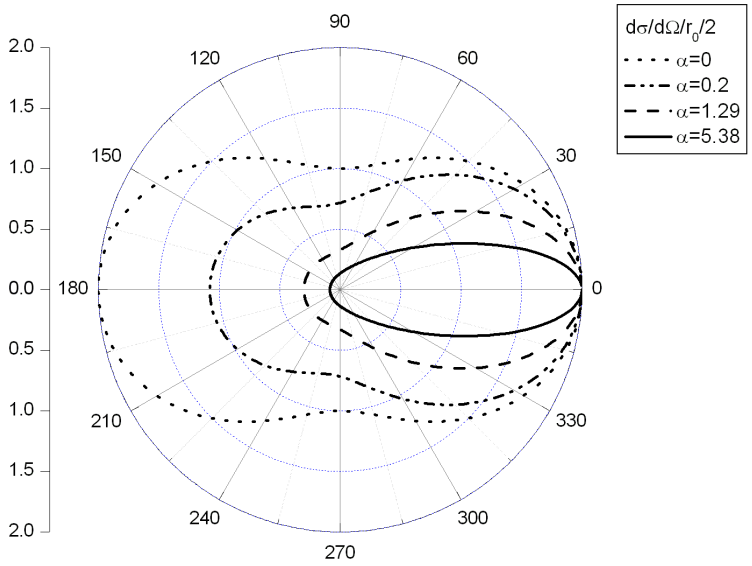

Fig. 2.5: Differential cross section for Compton scattering given by the Klein Nishina formula in a polar diagram

It is instructive to plot the Klein Nishina formula in polar coordinates where the radius is given by the differential cross section $d\sigma/d\Omega$ (Fig. 2.5). At low E_γ (or small ϵ), the well known $1 + \cos(2\theta)$ distribution is obtained which progressively deforms in the forward direction with an increasing ϵ.

2.2 Image Reconstruction

Although the image reconstruction is not the focus of this thesis, an overview of the inherent problems and solutions found by other groups and the group in Siegen (where the author of this thesis contributed) is given in order to allow a full appreciation of the complexity of the Compton camera systems, and to provide a relationship with the final experimental results of this thesis.

The Compton camera image reconstruction is a complex problem which is only partially solved up to date. The main difficulty of the reconstruction is that the possible source position lies on a surface of a cone, unlike Anger cameras where the possible source location lies on a line. In Fig. 2.6 image reconstruction principle of the Compton camera is demonstrated. A Compton coincidence event provides four parameters which are:

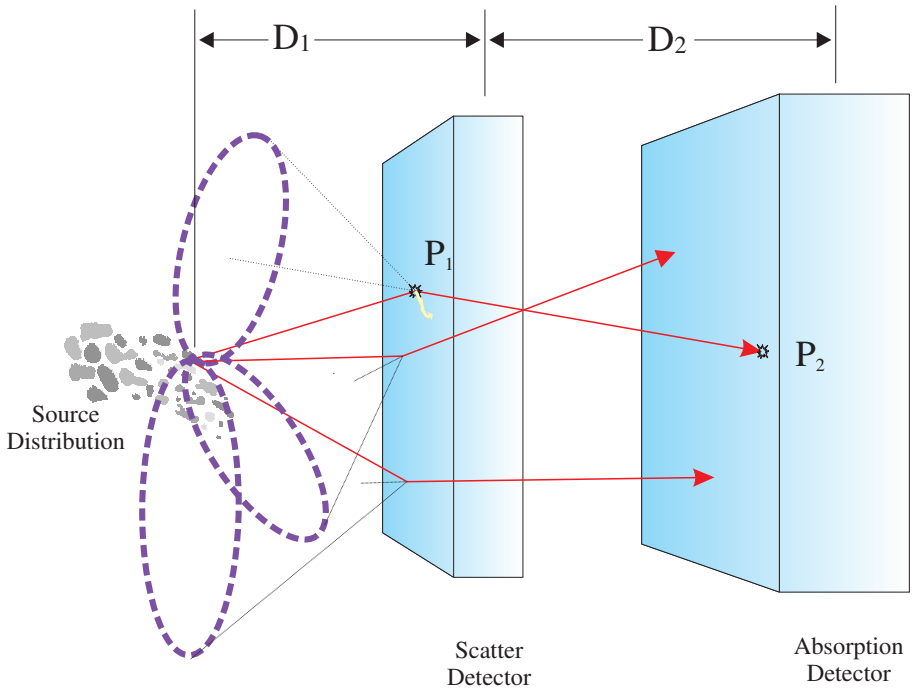

Fig. 2.6: The imaging principle of the Compton camera

P_1 interaction point of the coincident event in the scatter detector, which is defined as (x_1, y_1, z_1) in cartesian coordinates.

E_e energy information of the coincident event in the first detector; that is the captured energy of the recoil electron in the scatter detector.

P_2 interaction point of the coincident event in the absorption detector, which is also defined as (x_2, y_2, z_2) in cartesian coordinates.

$E_{\gamma'}$ energy information of the coincident event in the second detector; that is the captured energy of the scattered photon in the absorption detector.

Total γ-ray energy E_γ equals to $E_e + E_{\gamma'}$. If the energy of the incoming γ-ray is known which is the case for some applications utilizing monoenergetic radionuclides, this information can be used to eliminate partial interactions that may increase the reconstruction noise. Eq. 2.4 gives the relation between the Compton scattering angle and recorded energies. Using position information of the interactions and the scattering angle, it can mathematically be shown that all incoming γ-rays which satisfy the conditions above, lie on a surface of a cone. The source of the γ-ray should be somewhere on this cone whose apex is at P_1, axis vector is $(P_1 \vec{-} P_2)$ and the axis angle is the Compton scattering angle.

The simplest way for image reconstruction is creating projections of the backprojected cones to the region of interest and quantize the space as desired. For example if the source space is limited into a 2D image plane, backprojected cones create elliptical traces on this plane. This method is called a *s*imple backprojection method. In Fig. 2.7 an example of the image

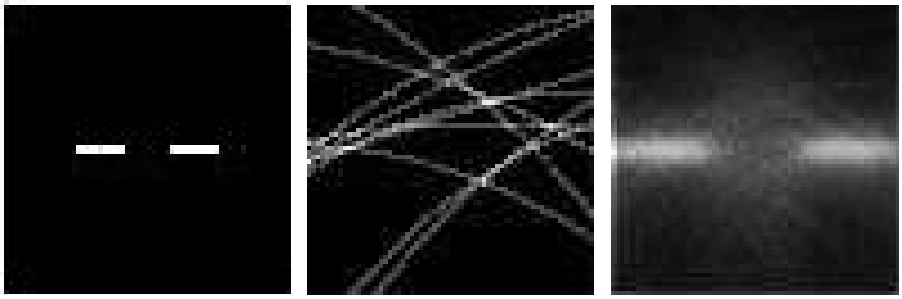

Fig. 2.7: Original image, reconstructed image using simple backprojection method with a few events and with more statistics

reconstruction with this method is demonstrated. As can be observed from this demonstration, simple backprojection usually creates blurry images due to the uncertainities in the recorded energies and positions, therefore, they are not good enough for useful medical diagnostics.

Many Compton camera reconstruction methods have been developed for the reconstruction of images from Compton camera data which can improve the quality of the simple backprojection significantly. They can be divided into two groups; which are called as iterative and direct reconstruction methods. The fundamental difference between these groups lies in how they treat the event data.

Iterative algorithms formulate the reconstruction problem as a deconvolution problem of a particular type where the 3D source distribution is deconvolved from its measured 2D projections. The reconstruction is then performed by throwing each projected 2D density distributions back to the 3D space with iterative corrections, which then brings the estimated 2D projections back that are in agreement with the measured data set [Gor74].

Singh and Doria [Dor82] who pioneered this field, proposed several iterative methods for 3D Compton camera image reconstruction, including simultaneous iterative reconstruction technique (SIRT), algebraic reconstruction technique (ART), iterative least squares (ILS), maximum likelihood estimation (MLE). They suggested that 3D reconstruction can be implemented in two stages. In the first stage, each pixel in the first detector is assumed to be a pin hole and for the γ-rays Compton scattered in this pixel the projection image is reconstructed with the events absorbed in the second detector. In the second stage, all these slightly different views (pin hole images) are merged to reconstruct the 3D source distribution.

In late 90s, list mode expectation maximization likelihood methods were proposed by Wilderman et al. [Wil98] as state of the art iterative methods which were efficient both computationally and storage wise.

Recently a new iterative algorithm, Imaginary Time Expectation Maximization (ITEM), has been proposed by Pauli [Pau02] and it has been further optimized by I. Chiosa [Chi04]. The main difference of this reconstruction algorithm, opposed to others, is that incremental dataset is sufficient to perform the reconstruction that allows real time continuous acquisition and imaging.

There are also direct methods developed in the last decade by Parra [Par00] and Gunter

[Gun03]. They provide solutions using a filtered backprojection of the the whole data set for a well defined geometrical setting.

Iterative methods are more flexible for the study that has been performed, as the geometry of the prototype system has not yet been fixed and these methods don't require explicit assumptions on geometry and data.

The ITEM method has been used for the image reconstruction to demonstrate the measurements obtained with the constructed Compton camera prototype system.

2.3 Basic Features of the Imaging Process

After introducing the concept of the Compton camera the theoretical description of the system is best explained going back to a general consideration of the imaging process.

Radiographical images can be defined as the result of applying an isomorphous function $\vec{y} = f(\vec{x})$ to a set of elements $\vec{x} \in S$ (finite or infinite) with a defined metric (vector space) such that the inverse function exists $\vec{x} = f^{-1}(\vec{y})$ with $\vec{x} \in D$. In the physical world, however, this general definition is restricted and softened at the same time. The restriction concerns mostly the use of non-deforming functions (leaving the ratio of distances and angles constant) and using physical means of creating the image with an optical system directing radiation from an object to a detection system via adequate optics. The essential change to the general mathematical description is due to the fact that radiation is used to perform the image such that in general the intensity of radiation in the image is used as a signal. As an example and as a basis for further discussion, the process of an x-ray exposure (e.g. for medical application) is considered.

The imaging function projected onto the image plane loaded with an x-ray sensitive layer (film) that is recording the impact of the x-ray quantum can be defined as

$$\vec{r'} = \alpha \cdot \vec{r} \tag{2.8}$$

It reflects the usual procedure of a point like source **S** and an object plane **A** projecting the point P on the film B in P'. A view of this arrangement is shown in Fig. 2.8(a) and also in the direction of the optical axis in Fig. 2.8(b) which reveals immediately the imaging function 2.8 with $\alpha = \frac{b}{a}$.

Fig. 2.8 shows at the same time another important feature of physical imaging. If the contents of the image is represented in the intensity of radiation in a given point P, then there must be an area defined around this point P' in order to collect a non-vanishing number of quanta since a single quantum hits only a δ-funtion like point (stochastic point process), while the intensity is given by the accumulation of a number of quanta. The intensity in this case is given by

$$I(x_v, y_v) = \iint\limits_{pixel} n(\vec{r}) dx dy \tag{2.9}$$

where $n(\vec{r})$ is the radiation flux and the integration is carried out over a square area $x_v - \frac{1}{2}\xi < x < x_v + \frac{1}{2}\xi$ and $y_v - \frac{1}{2}\xi < y < y_v + \frac{1}{2}\xi$ of size $a = \xi^2$ which is called a pixel.

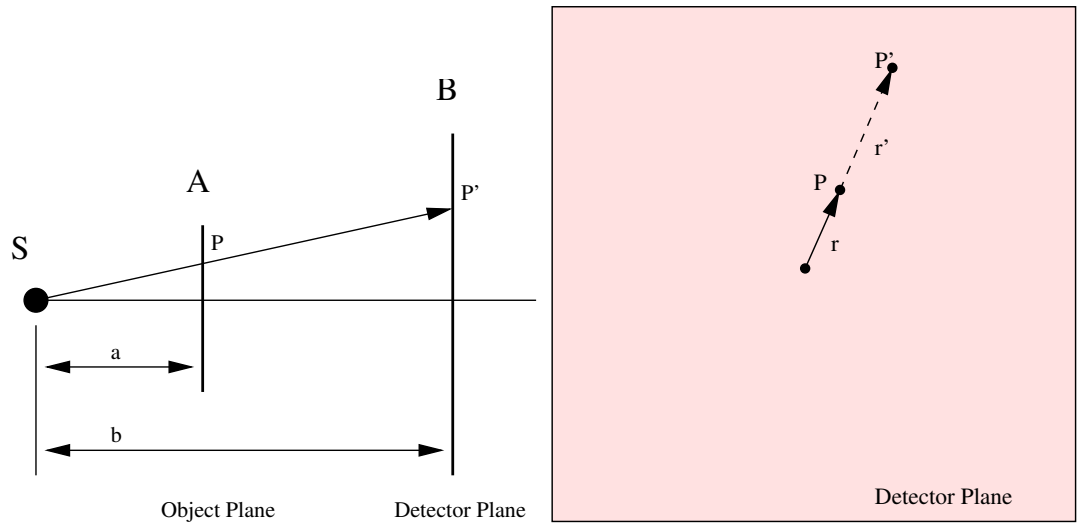

(a) (b)

Fig. 2.8: A simple imaging function

Since the collection of quanta is inherently a property of quantum mechanics, it can be modelled with probability of a quantum mechanical transition. This transition probability, P_{trans}, is given by the square of the matrix element between the final state f and the initial state i under control of the transition operator H_{if}.

$$P_{trans} \propto \langle f|H_{if}|i\rangle^2 . \tag{2.10}$$

In a spontaneous transition the probability is rather small for a single quantum system. Since there is a very large number of atoms involved in the radiation process, the transition probability defined above can almost perfectly be desribed by a Poisson process.

$$P_x(n) = \frac{\rho^n}{n!} e^{-\rho} \tag{2.11}$$

with the expectation value and variance defined as:

$$E[x] = \rho \text{ and } V[x] = E[x] = \rho \tag{2.12}$$

This feature of imaging with radiation imposes the principal limit of achievable precision which can not be overcome by engineering, it only can be approached. Therefore, basic measures reflecting the quality of an imaging detector are the spatial resolution and the detective quantum efficiency (DQE) which will be presented in detail below.

2.3.1 Spatial Resolution

For modern tomographic imaging, the imaging property discussed up to now is extended to three dimensions defining so called voxels (volume elements), instead of area-like pixels, such that the

appropriate imaging intensity is the collection of quanta being attributed to this volume as the origin of interaction. For the general precision of the quantum process, this does not change the arguments and therefore, the discussion will be restricted to the two dimensional case as introduced above. The discussion will follow the basic concepts as described in the literature [Dai74] since they apply to the problem which is the subject in this thesis.

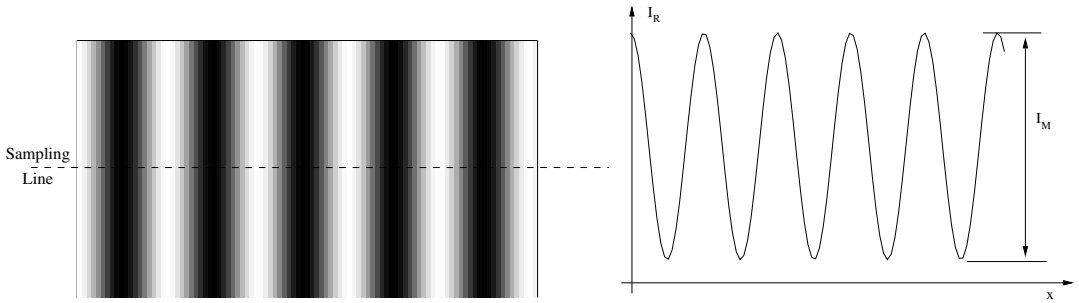

(a) (b)

Fig. 2.9: 2D bar pattern used as an input with its cross section

In the simplest case, the spatial resolution is given by the pixel size $a = \xi_x \cdot \xi_y$ as quite well found in CCD imaging devices. For simplicity, in the following it is sufficient to consider only the one dimensional case. Then a bar-pattern in y-direction with a pitch d as shown in Fig. 2.9(a) will cause a modulation of the radiation intensity $I_R(x)$ as a function of x which is given by an harmonic function:

$$I_R(x) = I_o + I_M \cos(2\pi\nu x) \tag{2.13}$$

where I_o is a constant contribution, I_M is the amplitude of the modulation and $\nu = \frac{1}{d}$ is the spatial frequency.

Ideally, the detector reproduces the image with an intensity variation given by I_M, but since there is no ideal detector, this variation will be smaller and the detected intensity $I_D(x)$ can be given as:

$$I_D(x) = I'_o + I_{M'} \cos(2\pi\nu x) \tag{2.14}$$

with $I_{M'} < I_M$ approaching occasionally the ideal value. It turns out that the ratio $R_I = \frac{I_{M'}}{I_M}$ is a function of the spatial frequency which can be tested by changing the frequency of the cosine-pattern correspondingly.

The magnitude of the imaging system response in spatial frequency domain is described by a modulation transfer function (MTF) which is commonly used in radiological physics. It can also be shown [Dai74] that R_I is given by the modulation transfer function (MTF), which is, in the present case, the magnitude of the Fourier transform of the line spread function (LSF). LSF is the one dimensional representation of the point spread function and for an ideal system it can be defined as follows;

$$\mathrm{LSF}(x) = \begin{cases} \frac{1}{\xi} & \text{for } |x| < \frac{\xi}{2} \\ 0 & \text{otherwise.} \end{cases} \tag{2.15}$$

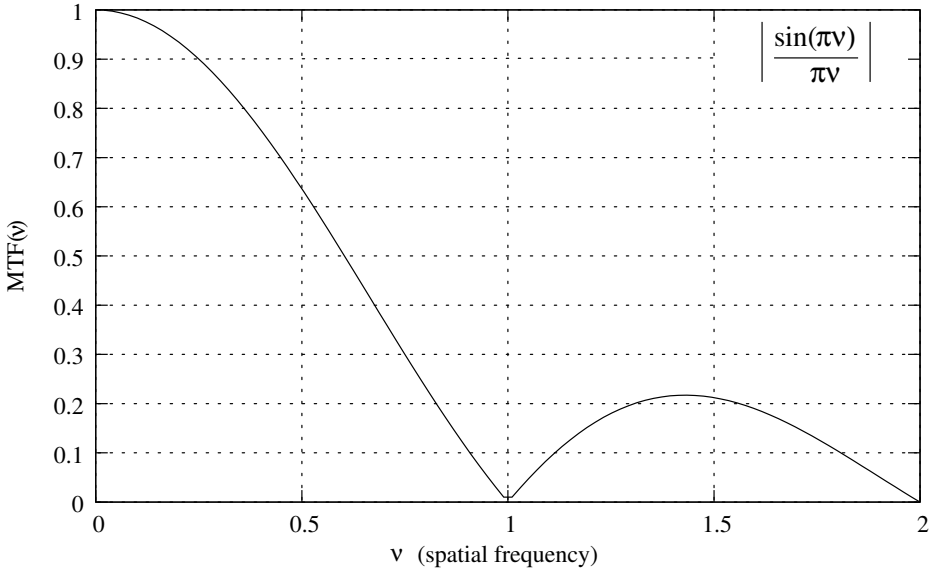

Fig. 2.10: MTF of an ideal pixelated system

Then the following can be obtained:

$$R_I = \mathrm{MTF}(\nu) = |\int_{-\infty}^{\infty} \mathrm{LSF}(x) e^{-2\pi i \nu x} dx| = |\frac{1}{\xi} \int_{-\frac{\xi}{2}}^{\frac{\xi}{2}} e^{-2\pi i \nu x} dx| = |\frac{\sin \pi \nu \xi}{\pi \nu \xi}| \tag{2.16}$$

The result is the well known $\mathrm{sinc}(\nu\xi)$ (sinus cardinalis) function. Mathematically appearing oscillating parts give rise to image distortions and will not be considered here. In the two dimensional case the two dimensional point spread function is defined (PSF) and MTF is obtained again by a two dimensional Fourier transform.

Although the PSF or LSF is not a box function and approaches more a Gaussian or a sum of Gaussians with different weight for most single quantum detectors, an MTF having a maximum at $\nu = 0$ and falling monotonically off for larger values is sufficient for the disccussion in the context of this thesis.

2.3.2 The Precision of An Intensity Measurement

The second important parameter to describe the precision of an imaging detector concerns the intensity measurement and hence, the contrast which produces a different image for different measurements. The detective quantum efficiency (DQE) is defined as;

$$\mathrm{DQE} = \frac{(\frac{S}{R})^2_{out}}{(\frac{S}{R})^2_{in}} \tag{2.17}$$

It is the ratio of the signal, S, to noise, R, at the output of the system squared divided by the same quantity squared at the input. For detectors, where the performance due to noise is close to the theoretical quantum limit, the noise at the input, R_{in}, is known:

$$R_{in} = \sqrt{E[N_{in}]} \tag{2.18}$$

since a Poisson process is assumed, where N_{in} denotes the number of quanta and $E[N_{in}] = \rho t$, where ρ is defined as the rate which is constant for a homogeneous Poisson process. The signal to noise ratio at the input is obtained as follows:

$$\left(\frac{S}{R}\right)_{in} = \frac{N_{in}}{\sqrt{N_{in}}} = \sqrt{N_{in}} \tag{2.19}$$

Since a quantum detector has a limited probability for absorption (which is the reverse process of the quantum generation discussed earlier) an efficiency ε has to be defined:

$$\varepsilon = \frac{E[N_{absorbed}]}{E[N_{in}]} < 1. \tag{2.20}$$

where $N_{absorbed}$ denotes the number of absorbed quanta.

In order to discuss the noise properties of the detector alone, it is useful to separate it from the absorption efficiency. Assuming a detector being ideal, except for the absorption efficiency $\varepsilon < 1$, the noise at the output is determined by the Poisson process and the signal to noise ratio is given by;

$$\left(\frac{S}{R}\right)_{out} = \frac{E[N_{abs}]}{\sqrt{E[N_{abs}]}} = \sqrt{E[N_{abs}]} = \sqrt{\varepsilon E[N_{in}]} \tag{2.21}$$

and for the DQE the following expression is obtained:

$$\mathrm{DQE} = \frac{\varepsilon N_{in}}{N_{in}} = \varepsilon. \tag{2.22}$$

Consequently, for the general case of an imperfect quantum detector, the following equation holds:

$$\mathrm{DQE} = \varepsilon \frac{(\frac{S}{R})^2_{out}}{E[N_{abs}]} = \varepsilon \cdot g(E[N_{abs}]) \tag{2.23}$$

which shows that the absorption efficiency ε can be separated from the rest of the DQE. Since the absorption of radiation detectors is a separate, and for the Compton camera a rather complicated subject, which has been extensively treated in another thesis [ÇN04a] related to this project. While discussing the effect of the digital signal processing in this thesis, it will be assumed that $\varepsilon = 1$, without sacrificing the most important insights. This is the case for any detector where the available quantum flux is the limiting parameter.

Unlike the noise for the input signal being assumed to be the variance of the theoretical quantum counting process, this assumption is not correct while estimating the noise for the observed counting at the output channel. This is due to the non-linear detector function $h(q)$ where the variable q is used for the number of quanta, but could be the exposure for other imaging systems, as well. For any imaging system, the detected signal is a function of this exposure q, and $h(q)$ is used as a calibration curve.

The noise at the output can be found as follows: If the detected signal is defined as $S_{out} = h(q)$, the noise will depend on S_{out} and therefore on q as well. The minimum noise at the output will be the quantum noise of the input $(R)_{in} \propto \sqrt{q}$ transformed to the output signal which yields $(\frac{S}{R})_{out} \propto \frac{h(q)}{\sqrt{q}} s$ where s is the slope of the calibration curve ($s = \frac{dh(q)}{dq}$). Finally, for the DQE, the following relation can be obtained:

$$\mathrm{DQE} \propto \frac{h(q)^2}{q} s^2 \tag{2.24}$$

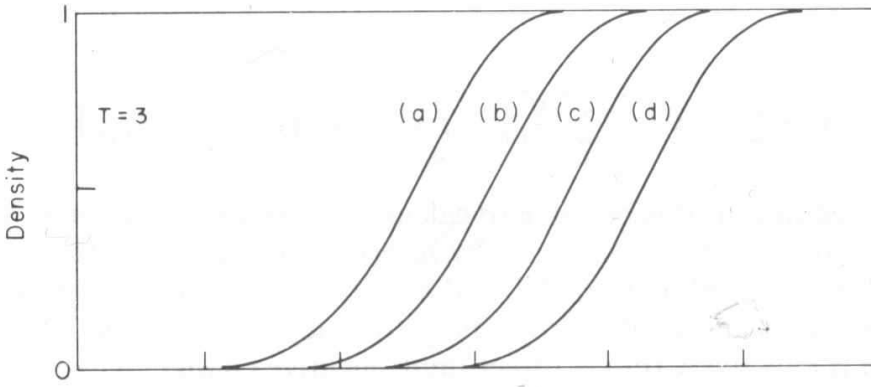

Fig. 2.11: Density as function of log exposure in film a) m = 1, b) m = 2, c) m =4, d) m = 8 [Dai74]

This is a remarkable result showing that the slope s of the calibration curve has a decisive impact on the DQE. Each time the slope drops to small values, the DQE drops as well. This is the case even for small signals, since q in the denominator disappears against $h(q)^2$ in the nominator which should drop to zero faster than q^2. The maximum of DQE is expected to be near the maximum of s where input counts are equal to the ouput counts and $s = 1$.

The concept of the DQE has been originally developed in the process of investigating the imaging properties of a photographic film and the finding in Eq. 2.24 will be illustrated using a simple model [Dai74] for a film, where the sensitivity and spatial resolution are found to be strongly coupled. As every photographer has learned, the speed of the film and the graininess are not independent of each other. The signal is represented by the optical density due to the silver grains reduced in the development process and the noise is represented by the fluctuation of the latter.

Starting from a statistical concept where T photons have to hit a silver halide grain for producing a latent nucleus and a probability p = 1/m (m = 1, 2, ... an integer), the density-exposure relations can be derived as shown in Fig. 2.11 for T = 3 and m = 1,2,4,8. The typical s-shaped exposure curve for the film is observed and it is recognized that the parameter m represents a quantity that is directly related to the number of grains per volume of the film. For an increased m the curves are shifted towards a higher exposure, which is exactly the effect of a fine grained film.

The dependence of the DQE on the exposure (proportional to N_{abs}) for a photographic film is shown in Fig. 2.12 and can be understood using Eq. 2.24. For a very low exposure the chance to absorb T photons in one grain decreases quickly and therefore, s vanishes and consequently the DQE as well. For a high exposure the number of silver halide grains forming the latent image will be so large that a further increase of the exposure is not possible and therefore s tends to zero again and the DQE decreases reaching ultimately zero (a completely over exposed black film does not contain an image information).

For other detection systems (eg. image plates) a similar dependence is observed and simple

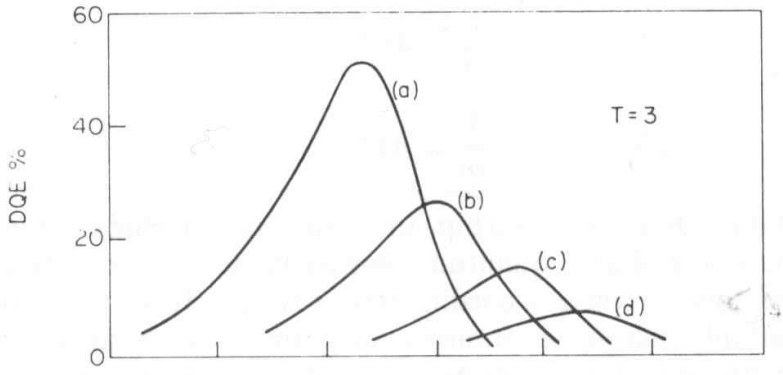

Fig. 2.12: DQE Example (film) a) m = 1, b) m = 2, c) m =4, d) m = 8 as above [Dai74]

quantitative models for a film-like detectors and a quantum detector will be introduced below.

Finally, it is useful to compare the whole system with an ideal detector, because any imperfection of the detector has the effect to raise the required quantum flux in order to reach the same performance as the ideal detector, thus making the waste of flux transparent. This is important for a number of imaging applications of which two are briefly discussed for illustration.

Assume a poor detector where a desired signal to noise at the output $\frac{S}{R_{out\_min}}$ is needed for a given performance. Then the required number of input photons is given by:

$$E[N_{in\_min}] = \frac{1}{\mathrm{DQE}} \left[\left(\frac{S}{R} \right)_{out\_min} \right]^2 \tag{2.25}$$

On the other hand, for a given photon flux the number of incoming photons is proportional to the time interval Δt of the measurement $E[N_{in}] = \rho \cdot \Delta t$, where the parameter ρ denotes the rate. Assume further that this time interval determines the resolution for dynamic measurements in the system:

$$\Delta t = \frac{1}{\mathrm{DQE}} \frac{\left[\left(\frac{S}{R} \right)_{out\_min} \right]^2}{\rho} \tag{2.26}$$

It can immediately be seen that the time resolution degrades with $\frac{1}{\mathrm{DQE}}$.

In the second case, the radiation dose D administered to a patient for an X-ray diagnosis is considered:

$$D = \gamma \cdot E[N_{in}] = \gamma \frac{\left[\left(\frac{S}{R} \right)_{opt} \right]^2}{\mathrm{DQE}} \tag{2.27}$$

It is seen that any value of DQE$<$ 1 increases the radiation dose to no useful purpose.

2.3.3 DQE and MTF

The two decisive parameters of an imaging detector, the spatial resolution and the detective quantum efficiency are not independent of each other. When the limit of the spatial resolution is approached, the MTF is decreasing (see above) and consequently the radiation flux must be increased in order to reach the same contrast as before. Since the highest value occurs

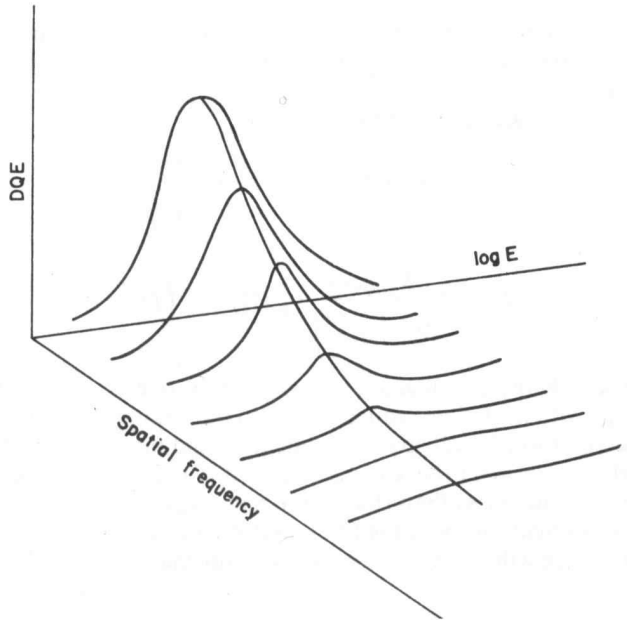

Fig. 2.13: DQE as a function of $\log(E[N_{in}])$ (which is denoted as an exposure (E) in this graph) and spatial frequency [Dai74]

at $\nu = 0$ this point is used for normalization and in a good approximation the physics of the processes allows the separation of the whole expression of two variables into a product of functions depending only on one at a time:

$$\mathrm{DQE}(\nu, N_{in}) = \mathrm{DQE}(0, N_{in}) \cdot h(\nu). \tag{2.28}$$

This behavior is illustrated in Fig. 2.13, where the dependence of $\mathrm{DQE}(\log(E[N_{in}]))$ with its maximum is reproduced and this shape is roughly maintained for higher spatial frequencies. As the frequency increases, the contrast reduces and finally any imaging information is lost in the noise. This effect of the MTF is mostly governed by the physics processes of radiation detection and signal generation in the detectors. It can be assumed that the readout electronics providing a sufficient dynamic range and resolution (effective number of bits) of the digitization process is independent of the design and performance of the readout electronics. Therefore, the investigation of the DQE is restricted and is focused on the dependence at zero spatial frequency.

2.3.4 Models for the DQE

The DQE of a quantum counting system can be calculated using Eq. 2.23, where the efficiency is usually constant and can be inserted later. Then the calculation for a given model only requires to find an expression for the signal to noise ratio at the output of the system as a function of the number of incident photons. For illustration purposes, two models are calculated representing the major classes of detector effects. The first model is an integrating detector with a parallel noise and the latter is a single photon counting detector with a paralyzable deadtime.

2.3.4.1 Integrating Detector with a Parallel Noise:

In an integrating detector (image plate, CCD, phosphor screen - image intensifier - combination) the energy E_p released by the absorbed photon is converted to a charge $Q_c = k \cdot E_p$ which is ultimately collected and stored in the detector capacity, where k is a conversion factor depending on the detector physics:

$$Q_{tot} = \sum_{\nu} Q_{c\nu} = \int_{t_o}^{t_o+\Delta} i(t)dt \tag{2.29}$$

This charge is accumulated for a given time, the exposure time, in which a certain number of photons are collected. Assuming that the charge liberated from one photon is spread out in time, the charge can be considered to generate a current $i(t) = \frac{dQ_c}{dt}$ which is integrated on a capacitor, hence the name integrating detector as shown in Fig. 2.14. In practice a feedback amplifier is used and the charge is stored on the feedback capacitor C_{fb} while a reset switch defines the integration time.

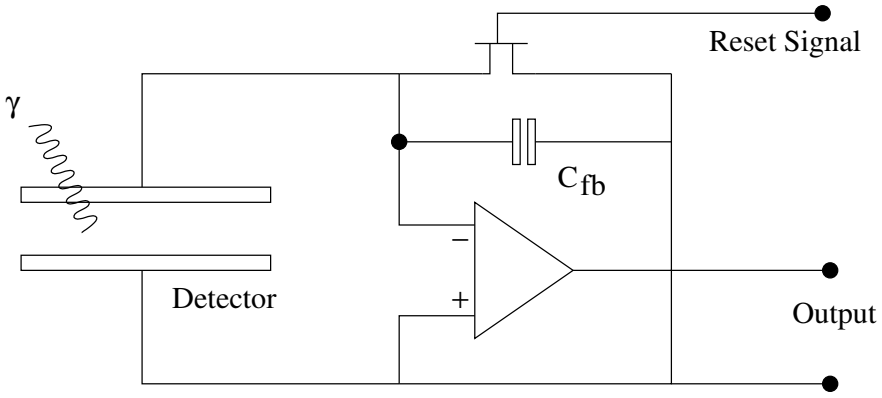

Fig. 2.14: An integrating detector system

Besides the inherent quantum noise (Poisson statistics with a contribution $k\sqrt{N_{in}}$), the fluctuations of the integrated charge depend on the fluctuation of the conversion process and noise added by the detector and the read out electronics, mostly the input stage. All these noise components ΔQ_i appear at the output of the system and are added in quadrature:

$$(\Delta Q_{tot})^2 = \sum_i \Delta Q_i^2 + k^2 N_{in} = k^2 \left(\sum_i \frac{\Delta Q_i^2}{k^2} + N_{in} \right) \tag{2.30}$$

If $\sum_i \frac{\Delta Q_i^2}{k^2}$ is set to be equal to N_{eq}^2, which expresses the additional noise sources in the equivalent units of charges generated by single photons, then the equation 2.30 can be rewritten as;

$$(\Delta Q_{tot})^2 = k^2 (N_{eq}^2 + N_{in}) \tag{2.31}$$

the signal to noise ratio at the output becomes;

$$\left(\frac{S}{R} \right)_{out}^2 = \frac{k^2 N_{in}^2}{k^2 (N_{eq}^2 + N_{in})} = \frac{N_{in}^2}{N_{eq}^2 + N_{in}} \tag{2.32}$$

and finally with N_{eq} being the constant equivalent noise, the DQE of such a detector can be given as:

$$\mathrm{DQE} = \frac{1}{\left(1 + \frac{N_{eq}^2}{N_{in}}\right)} \tag{2.33}$$

The dependence of DQE for several N_{eq} are presented in Fig. 2.15. It can be observed from this

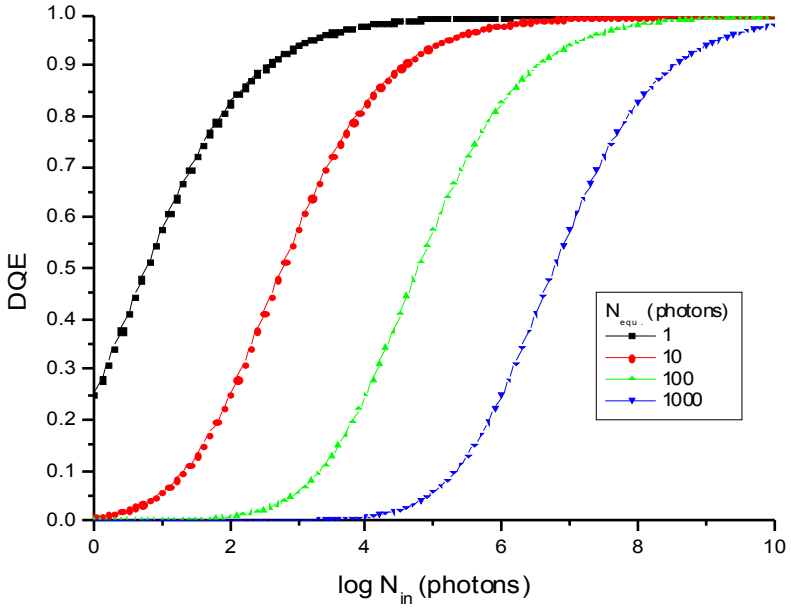

Fig. 2.15: DQE of an integrating sytem

figure that the noise level should be rather low in order to record a small number of photons. This is of importance for imaging with a very high dynamic range. Quantitatively, single photon recording sensitivity is required for the rates of 100 or more photons to achieve 90% DQE.

2.3.4.2 Single Photon Counting Detector with a Paralyzable Dead Time:

The second model represents the class of single photon counting detectors. The simplest case is given by a detector recording a monoenergetic radiation by converting single photons to electronic signals of charge $Q(t)$ with a well defined time structure which depends on the charge collection process in the detector as illustrated in Fig. 2.16. A good approximation for semiconductor detectors would be as follows;

$$Q(t) = Q_o \int_o^t \varphi(x)dx \tag{2.34}$$

where $\varphi(\sigma, x)$ is the Gaussian function of characteristic width σ. In the simplest case, this function which is proportional to the deposited energy, can be extacted by differentiation. Analog

pulse shaping using CR-RC filters reconditions the electrical signals within a certain duration before another pulse arrives. This time covers at least a duration of $\Delta t > 6\sigma$ in order to collect the full charge, but it may be substantially longer for achiving a better signal to noise ratio.

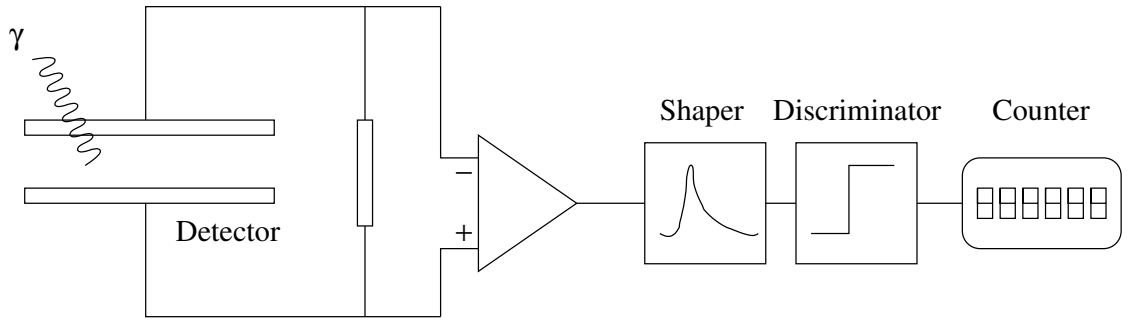

Fig. 2.16: A counting detector system

Obviously, a clean definition of one count can only be achieved when superimposed signals are avoided which introduces a deadtime τ. For most detector-shaper-discriminator combinations the deadtime behaviour is best described by a so called paralyzable deadtime which will be described in detail in section 2.4.

A measure of radiation intensity is the recorded counts in the counter and for simplicity, it is assumed that each photon arriving the detector produces a signal, but not necessarily a count due to the deadtime loss. The photon arrival process $N(t)$ and the counting process $L(t)$ are assumed to be stationary random processes and are defined as;

$$E[N(t)] = \rho \cdot t = \mathrm{N}$$
$$E[L(t)] = \lambda \cdot t = \mathrm{N}'$$

where ρ and λ are instantaneous rates of the arrival and counting processes and t is the measurement time. It is immediately clear that this counting process does not produce an additional noise as in the integrating detector described above, but the signal to noise ratio at the output is affected due to deadtime losses reducing ultimately the DQE. When the arrival process is a Poisson process, the measured number of counts of such a counting system is given by the following expectation value [ICR94]:

$$\mathrm{N}' = \frac{\chi}{\kappa} e^{-\chi} \tag{2.35}$$

where $\chi = \rho\tau$ and $\kappa = \frac{\tau}{t}$. The t represents the measurement time, τ is the deadtime of the detector and ρ is the instantaneous rate of the arrival process. In this formula and in the following calculations, the counted number and rates are understood to be mean values and not single measurements.

The rate behaviour is also studied with the assumption of long measurement times. It can be seen that the measured number of counts increases less than linear for higher input rates reaching eventually a maximum and this leads to the DQE loss. The error in the number of counts is represented by the variance [Yu00]:

$$V[L(x)] = \frac{\chi}{\kappa} e^{-\chi}[1 - (2\chi - \chi\kappa)e^{-\chi}] \tag{2.36}$$

Using the expectation value of Eq. 2.35 and the root mean square deviation given in Eq. 2.36, the following equation can be obtained:

$$\frac{\mathrm{N}'}{\Delta\mathrm{N}'} = \frac{E[L(x)]}{\sqrt{V[L(x)]}} = \sqrt{\frac{\chi}{\kappa}}\frac{e^{-\frac{1}{2}\chi}}{\sqrt{1-\chi(2-\kappa)e^{-\chi}}} \tag{2.37}$$

It is important to point out that the photon counting process deviates from a Poisson process, and it will be discussed in more detail. For the application discussed here this expression can be simplified further by observing that the measurement time is $t \gg \tau$ and consequently $\kappa \ll 1$:

$$\frac{\mathrm{N}'}{\Delta\mathrm{N}'} = \sqrt{\frac{\chi}{\kappa}\frac{e^{-\chi}}{1-2\chi e^{-\chi}}} \tag{2.38}$$

For the representation of an image, the real number of photons has to be estimated from the measured number of photons. This can be done by starting with Eq. 2.35:

$$\mathrm{N}' = \frac{1}{\kappa}f(\chi) \tag{2.39}$$

with $f(\chi) = \chi e^{-\chi}$. If a deadtime τ and a measurement time are known, then κ is known as well and Eq. 2.37 can be solved for χ which allows to produce an estimation of the input rate.

$$\mathrm{N} = \rho \cdot t = \frac{\chi}{\kappa} = \frac{1}{\kappa}f^{-1}(\kappa\mathrm{N}') \tag{2.40}$$

where f^{-1} is the inverse function of f.

The noise of the counting process $\Delta\mathrm{N}'$ can be calculated in the same way, which is not directly the square root of the variance given by Eq. 2.36, but the corrected given in Eq. 2.40.

Using the rules for the derivative of the inverse functions $x = f^{-1}(y)$, $\frac{d}{dx}f(x)\cdot\frac{d}{dy}f^{-1}(y) = 1$ and applying them to Eq. 2.39 and 2.40, the output noise can be derived using the standard method of error propagation:

$$\Delta\mathrm{N} = \Delta\mathrm{N}'\frac{e^{\chi}}{1-\chi} \tag{2.41}$$

This allows one to calculate the relative signal to noise ratio at the output.

$$\frac{\mathrm{N}}{\Delta\mathrm{N}} = \frac{\mathrm{N}'e^{\chi}}{\Delta\mathrm{N}'e^{\chi}}(1-\chi) = \frac{\mathrm{N}'}{\Delta\mathrm{N}'}(1-\chi) \tag{2.42}$$

Finally the DQE for a counting system is obtained as follows:

$$\mathrm{DQE} = \varepsilon\frac{(\frac{S}{R})^2_{out}}{E[N_{abs}]} = \varepsilon\frac{e^{-\chi}(1-\chi)^2}{1-2\chi e^{-\chi}} \tag{2.43}$$

In comparison to the DQE expression of an integrating system, it can be seen that the variables are different. In the integrating system, the converted photons are the decisive variable and the noise is determined by the photon equivalent noise, while in the photon counting system the deadtime τ determines the DQE. Consequently, the mean time difference ,$\lambda_t = \frac{1}{\rho}$, between the photon arrivals compared to the deadtime leads to the variable $\chi = \rho\cdot\tau$. This dependence is presented in Fig. 2.17, where the absorption efficiency is chosen to be one. This graph shows, in

addition to the theoretical result derived in Eq. 2.43, a few points which have been obtained by a Monte Carlo calculation confirming the assumptions in the derivation of Eq. 2.43 concerning the fluctuations and noise to be of minor influence. The slight deviation at the end for $\chi \approx 1$ is due to the fact that Monte Carlo calculation uses Eq. 2.40 for estimating the input rate as well. Since this function has a maximum at $\chi = 1$, the slope of this function becomes negative for $\chi > 1$ and ambiguous values for N are obtained. This has been excluded from the Monte Carlo calculation and therefore, the statistical distribution of the counted photons is truncated. This leads to a slightly larger DQE.

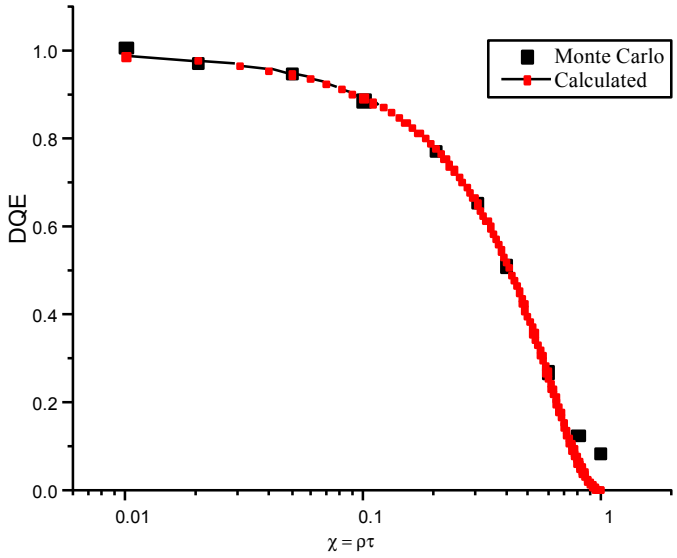

Fig. 2.17: DQE of a counting system

In order to compare integrating and photon counting systems, Eq. 2.43 is used and modified to display the number of input photons as variable. Then the measurement time or κ for a given rate has to be specified. This quantity enters as a parameter in Fig. 2.18. Again, the end point of the useful DQE curve is characterized by DQE = 0. Values beyond this point have no practical meaning since the output values are ambiguous and therefore, they should be ignored.

2.3.5 Comparison of Models

Comparison of Fig. 2.15 and Fig. 2.18 reveals already the most salient features of the two DQE models. Normally integrating detectors with modern electronics (FET input stages with an equivalent noise charge ENC = 400 e_0, $\Delta t = 10^{-6}...10^{-3}s$) can be operated with a one photon sensitivity and then they are very competitive in dynamic range and for high counting rates. At very high counting rates, space charge and saturation effects will finally lower the DQE. At very low counting rates and correspondingly long integration times, the 1/f noise and leakeage currents in the detector seriously degrade the performance.

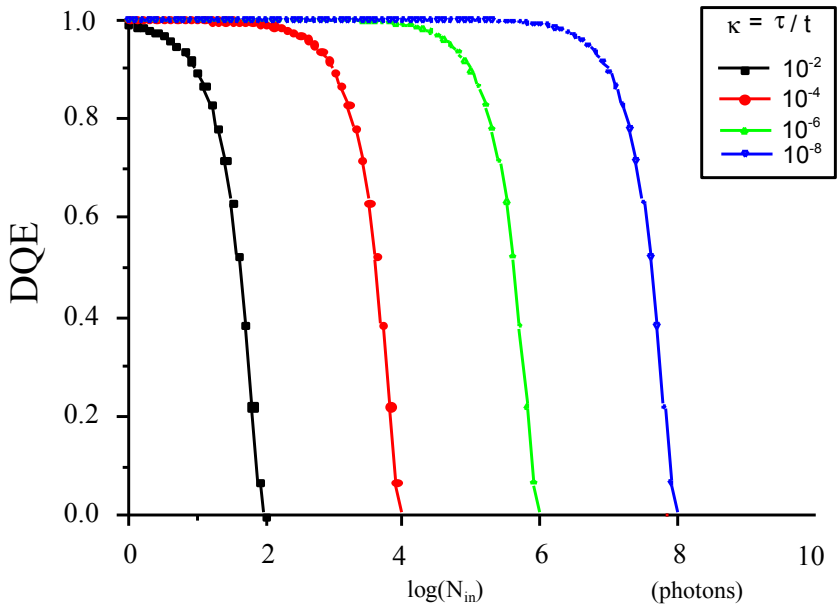

Fig. 2.18: DQE of a counting system with a parameter κ.

Single photon counting systems have advantages at very low counting rate and therefore, at very long measurement intervals (Δt), they are only limited by the absorption efficiency to achieve a reasonable DQE. This may be of importance for imaging in the field of astrophysics, where extremely faint objects are recorded or in the field of environmental monitoring, where small concentrations are detected.

On the other hand, at high counting rates the single photon detection principle is severely limited by deadtime effects and it is visible from the analysis (Eq. 2.43, Fig. 2.18) that the maximum count rate should be kept at least one order of magnitude below the inverse deadtime. For example, a deadtime of $\tau = .1\ \mu s$ (which is for complex counting systems already a good value), a rate of 10^5 counts/s should not be exceeded. This imposes a limit on the achievable resolution if a high input rate is required. For a measurement time of 10 ms (frame rate of 100 Hz), only 1000 counts are recorded with a resolution of 3%. Higher rates quickly degrade the resolution.

Therefore, it can be concluded that integrating systems are superior to counting systems for high speed and high intensity applications, while the opposite holds for low level imaging. However this is not the only difference between integrating and counting systems and there are good reasons to investigate the limits of the deadtime in order to render counting systems suitable for high count rate applications. In particular a counting system is able to record additional information such as the energy of the quantum recorded, the precise timing or even more complex information like the angle of incidence, the mass of the particle etc. The energy information of fluorescent X-rays is an important tool for identifying different elements in samples during

observation in an electron microscope.

The main advantage of quantum counting, however, becomes evident if complex events have to be recorded. The best known and very successful system of this category is the Positron Emission Tomography (PET), where the two annihilation quanta of the positron are recorded in coincidence and the reconstructed straight line connection between them is used for the image reconstruction. Up to now hard wired coincidence units are used for the event selection with the limitation of solid angle acceptance. The progress in the field of microbiology and genetic engineering has stimulated the demand for this type of a detection system for research as well as for medical diagnostics because it is best suited to image biological and physiological processes. Since the limited dose administration and the need for dynamic measurements are essential for these applications, the research and development concerning the next generation PET systems focuses on the increase of sensitivity, which means the increase of acceptance and hence the ount rate. Dead time effects occurring in the system are the main limitation at present. One direction of research investigates faster scintillation crystals, but first reports on parallel event processing are emerging as well.

2.3.6 Significance of the DQE Studies for the Compton Camera

The coincidence method of the PET represents the simplest way of correlation measurement, since it only requires equal timing which can easily be implemented electronically. The precision of the coincidence timing at the process of generation can be considered to be instantaneous, but the flight path may contribute $\Delta t = \Delta x/c \approx 1$ ns with $\Delta x = 30$ cm (size of the body), where c is the speed of light. Modern scintillation detectors may allow a similar precision such that coincidence windows of about 2 ns are achievable. Then the events defined as coincident are processed to obtain the image. This would not be sufficient in a Compton camera, since the additional information of the electron energy from the scatter detector has to be processed as well. A good amplitude measurement requires considerably larger time window (0.1 to 1.0 μs). This processing window may be even larger when additional constraints of position readout have to be considered. Theoretically a hard wired solution is conceivable and systems have been developed for particle physics experiments. This solution can not be transferred to imaging systems since it is a special property of particle physics and, almost without exception, very rare events in a large background are of interest. This allows an enormous sequential data reduction depending on successive trigger levels.

A possible solution for event selection and reconstruction with the necessary flexibility is the implementation of a signal capture in terms of phase (timing) and amplitude in a time window of interest which is given by the slowest component. This implementation can be achieved by using programmable processors.

The conditions for such a system for optimum processing are not known and a discussion of the behaviour is not found in the literature. Therefore, it is the main subject raised in this thesis whether the performance can be described in a global manner, while details of technical aspects (processing speed, detector time resolution, event recognition complexity) are not reflected . It

is found that the concept of DQE allows here a quantitative measure of the performance as well. The questions to be addressed are:

- What is the equivalent deadtime of such a system (or whether this concept is applicable at all)?
- What are the important parameters in the design of the readout electronics?
- Is it possible to derive general rules for the design of the signal processing system?

These will be answered in the following chapters.

2.4 Data Flow

The counting performance directly affects the DQE of the system which is introduced in the previous section. In this section a detailed analysis and characterization of counting systems and coincidence processing with the focus on relevance for readout electronics are presented.

2.4.1 Statistical Properties of Nuclear Sources

As it has been shown, the probability distribution of the nuclear disintegrations is assumed to be a Poisson random process. There is no known experimental result that contradicts this fundamental assumption [Kno99]. Therefore, the interval distribution between successive disintegrations shows an exponential-decay behaviour. To study the performance of the acquisition system, the disintegration process should be investigated first.

The disintegration of atomic nuclei fulfills the following conditions:

- The possibility of the disintegration of a single atom in a given time interval is the same for all atoms of the same type.
- The disintegration of an atom in a given interval doesn't effect the probability of other atoms also to disintegrate at the same time.
- The possibility of a disintegration is same for all equal time intervals.
- The number of atoms and time intervals are large.

The probability of observing n interactions for a given time interval τ is defined as follows:

$$P(n,\tau) = \frac{(\rho\tau)^n}{n!}e^{-\rho\tau} \tag{2.44}$$

where ρ is the average rate of appearance. Using Eq. (2.44) the interval distribution can be derived in the following way [Kno99]: The probability of having no events in the time interval t is,

$$P(0,t) = \frac{(\rho t)^0}{0!}e^{-\rho t} = e^{-\rho t} \tag{2.45}$$

and the probability of having an event in the time interval dt is ρdt. So, having no events in t and having an event in $t + dt$ is $\rho e^{-\rho t} dt$, which leads to:

$$I(t)dt = \rho e^{-\rho t} dt \tag{2.46}$$

where $I(t)$ is the distribution of intervals between successive random events as shown in Fig. 2.19.

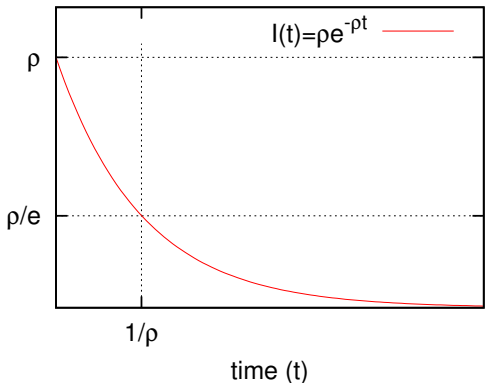

Fig. 2.19: Interval distribution

The integral of $I(t)$ is bounded and is equal to $\int_0^\infty I(t)dt = 1$. The average interval length is $\frac{1}{\rho}$, as expected.

The probability of having an event interval smaller than the average is $\int_0^{1/\rho} \rho e^{-\rho t} dt = \frac{e-1}{e} = .63$ and having an event interval longer than the average is $\frac{1}{e} = .37$. This shows that smaller intervals between successive events are more probable than longer intervals (Fig. 2.19). Using this model for the interval distribution, models for the system deadtime can be developed and characterized as given in the following section.

2.4.2 Classical Dead Time Models for Single Detectors

All counting devices used for counting single γ-rays or particles have a *deadtime* in which the device is not responsive to the successive pulse or pulses. Due to the random nature of nuclear disintegrations, there will always be events for which the device is unresponsive.

There are several deadtime models defined in the literature [Eva82, Kno99, Mue73, Yu00]. Although deadtime models depend mainly on the detector system of interest and can be a mixture of models, they are usually classified into two groups.

Paralyzable (or *Extended*[Mue73]) Deadtime[Eva82]: According to this model, an event always generates a characteristic deadtime regardless of whether the event is recorded or not. A paralyzable system almost can not record a single event if the average event interval is smaller than the characteristic deadtime. Geiger-Müller-based monitoring sys-

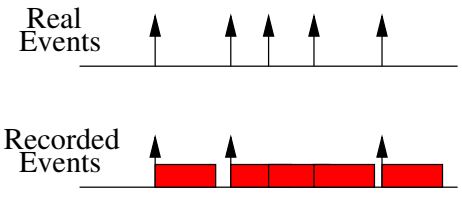

Fig. 2.20: Deadtime model of a paralyzable system where the deadtime is indicated as blocks.

tems are examples of such systems where, as the flux of events increases the count rate increases to a maximum point and then starts to decrease. This may lead to a significant underestimation of the source activity. Another example of the paralyzable deadtime is

a photomultiplier tube. Typically a shaping amplifier and a discriminator are used to convert the photomultiplier current into a pulse height. Duration of the signal above the discriminator threshold is a paralyzable deadtime due to the fact that additional pulses arriving in this period extend the signal as well as the deadtime, as illustrated in Fig. 2.20.

Nonparalyzable (or *Non-extended*) Deadtime: According to this model, only the events that are recorded, generate a characteristic fixed deadtime, in which any other event can not be recorded. Unrecorded events have no further effect on the deadtime of the system. This type of deadtime can be seen in Fig. 2.21. This model normally exibits itself on the registered outputs of the counters.

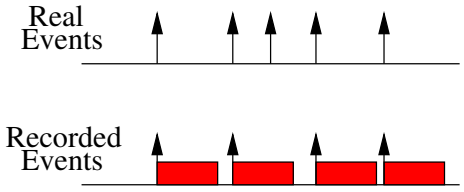

Fig. 2.21: Deadtime model of a nonparalyzable system where the deadtime is indicated as blocks.

Some researchers also suggest another model [Yu02] that is similar to the paralyzable model. This model is found to be useful for SPECT systems and is formulated as follows: If two events arrive within a time difference of τ, then they are rejected. It models the *pile-up* effect, where two or more events occur in the system within a time window τ and the system can not determine the correct spatial information from the events as they are superimposed.

The deadtime lowers the count rate by the loss of pulses. But the reduction of the count rate can not be measured directly as the true count rate is unknown, which is one of the essential parameter one would like to know. This perturbative effect of the deadtime on the original count rate can be described by considering the count rate, interval density or the statistics of the counts.

In general, deadtime modified interval density function $F(t)$ should be known before the observed count rate λ can be calculated since,

$$\lambda^{-1} = \int_0^\infty tF(t)dt. \tag{2.47}$$

Even for simple cases, it may be rather complicated to find $F(t)$ analytically depending on the original event interval distribution and the deadtime model. As an example, for an original Poisson process, the paralyzable deadtime τ leads to a modified interval density $F(t)$ which is given as,

$$F(t) = \sum_{j=1}^{J} u(t-j\tau)\frac{(-1)^{j-1}}{(j-1)!}\rho^j(t-j\tau)^{j-1}e^{-j\rho\tau}$$

where J is the largest integer below t/τ [Mue73] and $u(t-\xi)$ is the unit step function defined as $u(t-\xi) = 1$ if $t \geq \xi$, and $\quad u(t-\xi) = 0$ if $t < \xi$. Monte-Carlo simulations of the observed event

interval distributions for paralyzable and nonparalyzable systems are demonstrated in Fig. 2.22, where real event rate is defined as $\rho = \frac{1}{\tau}$. It will be assumed that the source of incoming pulses

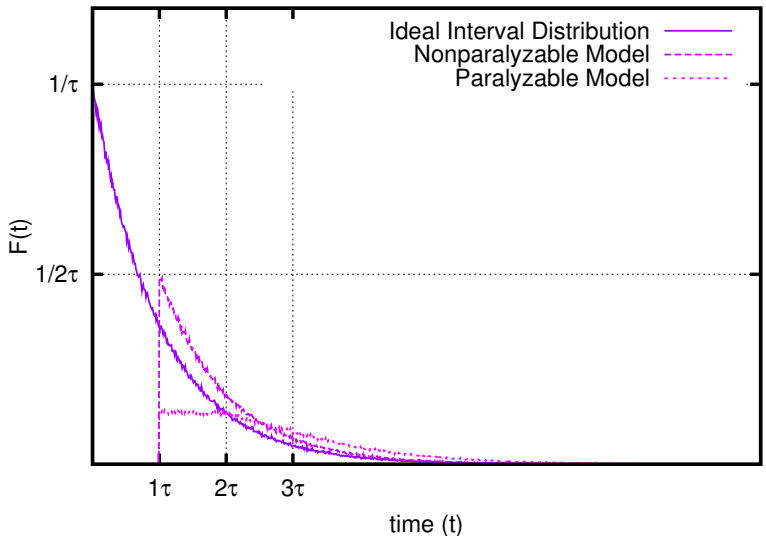

Fig. 2.22: Simulated interval distribution functions for paralyzable and nonparalyzable systems

are Poisson processes during the rest of the chapter. This is true virtually for all applications involving radioactive sources. The following definitions are made:

ρ : Real event rate
λ : Observed event rate
τ : Characteristic deadtime of the given system
t : Total observation time
r : Width of the coincidence window
κ : $\frac{\tau}{t}$
χ : $\rho \cdot \tau$
$E[]$: First moment of a given function
$V[]$: Second central moment of a given function
$N(t)$: Photon arrival process that counts the arrived photons in the (0,t] interval.
$L(t)$: Photon recording process that counts the detected photons in the (0,t] interval.

It is assumed that $N(t)$ is a homogeneous Poisson process, although $L(t)$ is not necessarily such a process as it will be shown. The counting processes $N(t)$ and $L(t)$ are assumed to be stationary and have the following property:

$$E[N(t)] = \rho \cdot t$$
$$E[L(t)] = \lambda \cdot t$$

2.4.2.1 Non-Paralyzable Model:

Time interval distribution function for this model, given that its input is a Poisson process, is as follows [Mue73]:

$$F(t) = u(t-\tau)\rho e^{-\rho(t-\tau)} \tag{2.48}$$

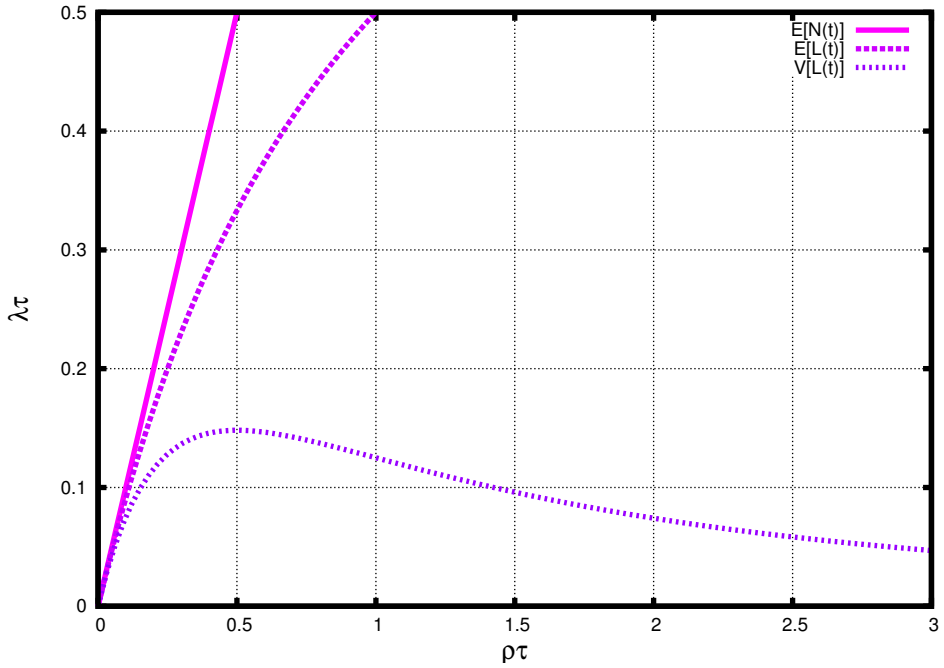

Fig. 2.23: Mean and variance for a nonparalyzing model where t=1

where $u(t-\xi)$ is the unit step function.

As it can be seen from the formula above, the time interval distribution of the recorded events at the output of a non-paralyzable detector is just a shifted version of the original distribution. Using Eq. 2.47 resulting count rate can be calculated as;

$$\lambda^{-1} = \rho \int_{\tau}^{\infty} t e^{-\rho(t-\tau)} dt = \rho^{-1} + \tau \tag{2.49}$$

and finally the observed event rate becomes:

$$\lambda = \frac{\rho}{1+\rho\tau} \tag{2.50}$$

The expected value and variance of the counting process are then given by;

$$E[L(t)] = \frac{\rho \cdot t}{1+\rho\tau}, \quad V[L(t)] = \frac{\rho \cdot t}{(1+\rho\tau)^3} \tag{2.51}$$

In practice we would like to determine the real count rate in terms of the observed rate and the known deadtime. This can be written as:

$$\rho = \frac{\lambda}{1-\lambda\tau}$$

In Fig. 2.23, the mean and variance of a detector with a non-paralyzable deadtime is shown. As it can be seen, even for $\chi \sim 0.05$ the mean and variance differ by at least 10% and the $L(t)$ process becomes non Poissonian.

2.4.2.2 Paralyzable Model:

The mean of $L(t)$ can be calculated for the systems with a paralyzable deadtime as will be described in this section. It can be observed in Fig. 2.22 that finding $F(t)$ may be complicated. An alternative way for this calculation will therefore be followed. It is known that only counts with an original time interval greater then the deadtime are recorded and all others are not recorded. This behaviour can be used to find the relationship between the observed rate and the real rate as follows;

$$\lambda = \rho \left[1 - \int_0^\tau f(t)dt \right] \tag{2.52}$$

where $f(t)$ is a Poisson process with $f(t) = u(t)\rho e^{-\rho \cdot t}$. When the counts that can not be recorded are eliminated, the equation becomes:

$$\lambda = \rho e^{-\rho\tau} \tag{2.53}$$

and E[L(t)] can be written as follows;

$$E[L(t)] = \frac{\chi}{\kappa} e^{-\chi} \tag{2.54}$$

where $\chi = \rho\tau$ and $\kappa = \frac{\tau}{t}$.

Although the mean value of $L(t)$ is calculated easily, deriving the variance of $L(t)$ is a lot more complicated. Here it is given only as a result and the derivation can be found in [Yu00].

$$V[L(t)] = \frac{\chi}{\kappa} e^{-\chi}[1 - (2\chi - \chi\kappa)e^{-\chi}] \tag{2.55}$$

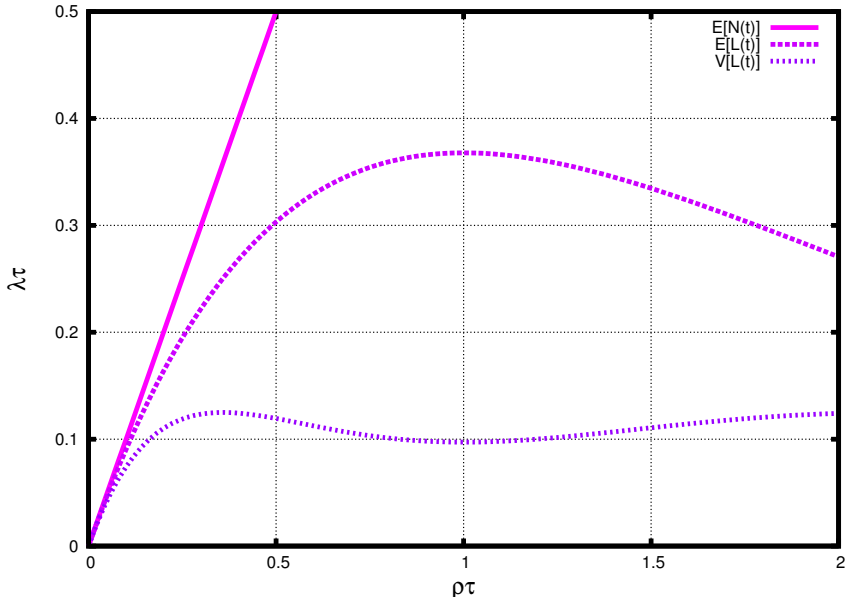

Fig. 2.24: Mean and variance of paralyzable systems where κ is very small ($< .01$)

The change of mean and variance of the paralyzable model with respect to the rate is presented in Fig. 2.24. Paralyzable systems show a non-Poissonian behaviour with the increasing rate as do nonparalyzable systems.

The real count rate of a paralyzable system with an observed rate and known deadtime can be calculated as follows:

$$\rho = \frac{\lambda}{1 - \lambda\tau \sum_{j=0}^{\infty} \frac{(j\lambda\tau)^j}{(j+1)!}} \tag{2.56}$$

In Fig. 2.25 observed rate normalized with a deadtime is plotted with respect to the real rate which is also normalized for both paralyzable and nonparalyzable systems. As the real count rate increases and reaches to a point where $\rho\tau = 1$, the paralyzable system literally saturates and the contrast information that it carries drops practically to zero. Under this condition the observed rate is only $\frac{1}{e}$ of the real event rate.

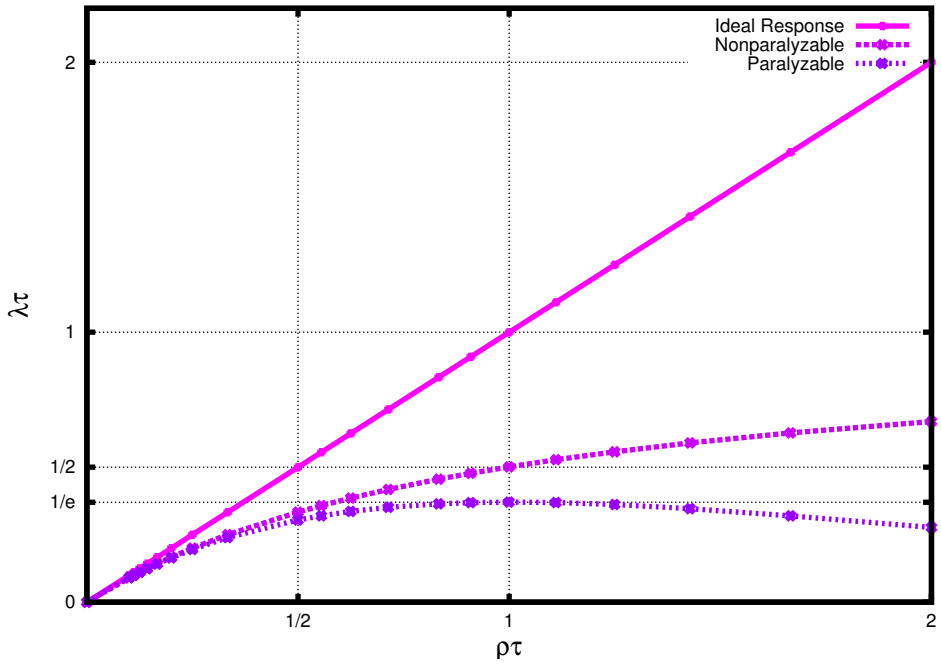

Fig. 2.25: Real events versus observed events for paralyzable and nonparalyzable systems

The observed event rate for the nonparalyzable system with the same condition is half of the real event rate. As the rate increases beyond $\rho\tau > 1$, the observed rate of the paralyzable system decreases and tends to zero asymptotically. On the contrary, the observed rate of the nonparalyzable system continues to increase and reaches to an asymptotic maximum of $\frac{1}{\tau}$. For low rates where $\rho\tau < \frac{1}{10}$, paralyzable and nonparalyzable systems are nearly equal and counting errors due to deadtime are less then 5%.

After this short review of the deadtime calculations for single detectors, the focus will be given on coincidence systems in the following section.

2.4.3 Coincidence Measurements

Coincidence measurement methods can be applied to many nuclear activity measurements as well as Compton systems. In its simplest form, the coincidence method requires two detectors (A and B) each of which would ideally respond to only one type of interaction. A coincidence then occurs if the time difference between an event in the detector A and an event in the detector B are smaller than a predetermined coincidence time window r. In Fig.2.26, a simple model for such a coincidence measurement system is illustrated.

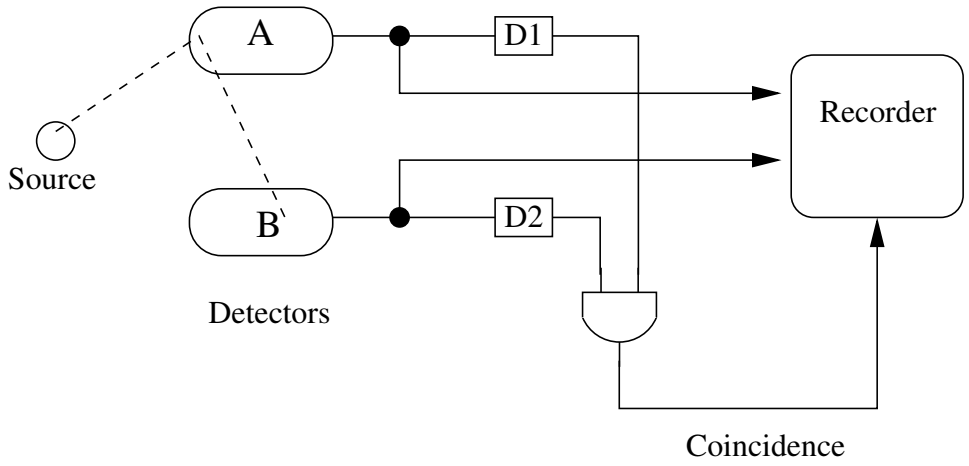

Fig. 2.26: Model for the coincidence method where D1 and D2 generate necessary time windows for coincidence that is implemented with the AND logic gate.

Coincident events are called genuine-coincidences in which the recorded events in both detectors originate from the same Compton event. All other coincidences are defined as accidental coincidences.

Traditional methods provide valid formulations for sufficiently low count rates and no formula is consistently superior over a wide rage of count rates and deadtimes [ICR94].

However, recently a more complete mathematical model for coincidence measurements has been proposed with certain constraints [Yu02]. In this study, two paralyzable detector models are used. The arrival processes X_1 and X_2 are defined to be Poisson and they satisfy the following model:

$$X_1(t) = N_c(t) + N_1(t) \tag{2.57}$$

$$X_2(t) = N_c(t) + N_2(t) \tag{2.58}$$

$N_c(t)$ is the counting process of the source generating genuine coincidences. $N_1(t)$ and $N_2(t)$ are the independent counting processes caused by random particles from other sources. The corresponding counting rates are ρ_c, ρ_1 and ρ_2.

If the recorded number of events are defined as $S_1(t)$ and $S_2(t)$ in time, then:

$$\Delta S_i(t) = 1 \text{ if and only if } \Delta X_i(t) \geq 1 \text{ and } X_i(t-\tau_i, t) - \Delta X_i(t) = 0$$

where $X(s,t) = X(t) - X(s)$ is the number of increments in the half open interval (s,t].

In this context deadtimes τ_1 and τ_2 are deterministic and are known, therefore, there is no uncertainity in time stamping the events, and the width of the coincidence window r satistifes the condition $2r < min(\tau_1, \tau_2)$. The coincidence condition can be defined as follows [Yu02]:

> If one particle is recorded by detector A at time t_1, and other particle is recorded by detector B at time t_2 and if $|t_1 - t_2| < r$, then this pair of particles are recorded as a coincidence event.

If the total number of coincidence events that are recorded in the interval (0,t] is denoted by $Y(t)$, then,

$$\Delta Y(t) = \Delta S_1(t) S_2(t-r, t) + \Delta S_2(t) S_1(t-r, t) - \Delta S_1(t) \Delta S_2(t) \tag{2.59}$$

The expected value and variance of $Y(t)$ is investigated under certain conditions.

2.4.3.1 Accidental Coincidences in Paralyzable Detectors

The mean and variance of a purely accidental coincidence process $Y(t)$ in the presence of paralyzable deadtimes in both detectors ($\tau_1 = \tau_2 = \tau$) can be given as follows:

$$E[Y(t)] = 2r\lambda_1\lambda_2 t \tag{2.60}$$

where $\lambda_i = \rho_i e^{-\rho_i \tau}$, which are the observable rates of singles for paralyzable detectors and r is the width of the coincidence window. The variance of accidental coincidences can also be given as;

$$V[Y(t)] = \lambda_c t(1 - \lambda_c \tau(2 - \frac{\tau}{t})) + \frac{\lambda_c^2}{24}(5r^2 - 16r(t-\tau)) \tag{2.61}$$

where $\lambda_c = 2r\rho_1\rho_2 e^{-(\rho_1+\rho_2)\tau}$.

2.4.3.2 Coincidences in Paralyzable Detectors

Following assumptions are made in order to find the mean and variance of all coincidences (genuine + accidental) of a coincidence system modeled with two paralyzable detectors. The real rates ρ_1, ρ_2 and ρ_c are constant in time and two deadtimes are chosen to be equal.

$$\lambda_c = \left[\left(\frac{2\rho_1\rho_2}{\rho_c} + \rho_1 + \rho_2 \right) (1 - e^{-\rho_c r}) + \rho_c e^{-(\rho_c+\rho_1+\rho_2)*\tau} \right] \tag{2.62}$$

then $E[Y(t)] = \lambda_c t$. In order to find the coincidence rate, ρ_c, with the observed and known parameters $(\lambda_c, \lambda_1, \lambda_2, \tau, r)$, Eq. 2.62 should be solved numerically.

The variance of the coincidence counting is given with the following boundary condition:

$$\lambda_c t[1 - \lambda_c(\tau + r)(2 - \frac{\tau + r}{t})] \leq V[Y(t)] \leq \lambda_c t[1 - \lambda_c \tau(2 - \frac{\tau}{t})] \tag{2.63}$$

2.5 Conclusion

The theoretical work on deadtime properties of coincidence systems are limited to very small subset of the possible values. For instance, no mathematical work has been done for the condition where r is greater than the deadtime of the detectors, which is a typical case for drift detectors.

In order to calculate detector quantum efficieny (DQE) for these cases theoretical work doesn't suffice, a Monte Carlo simulator has been developed and the results are presented in the following chapters.

Chapter 3

Prototype System

In this chapter, a prototype Compton camera system [ÇN04b] that has been constructed to study the various system parameters [ÇN02], will be described. This prototype is the first of its kind where Silicon Drift Detector (SDD) [Str98] is used as a scatter detector. Silicon is theoretically the optimal detector material as a scatter detector with a very high Compton scattering cross-section for the energy range of interest.

In a previous study [LeB99] silicon pixel detectors were used for this purpose, which couldn't exploit all of the desired potential of silicon. On the other hand, silicon drift detectors chosen for this prototype have excellent energy resolution characteristics. It has been shown that high energy resolution is critical for Compton camera systems, with the measurements. The

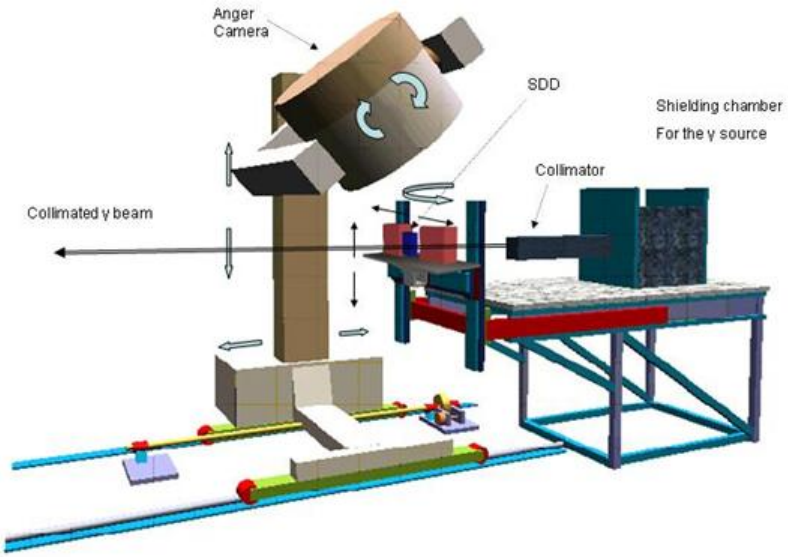

Fig. 3.1: Compton camera setup

second detector used in the prototype is a commercial Anger camera without a lead collimator.

Finely-collimated 1 Curie (Ci) ^{137}Cs source is used as a radioactive source. Signals produced by these detectors are transferred to the data acquisition (DAQ) system which follows the analog readout chain. Processed signals are converted to event candidates in the DAQ system and then transferred to the reconstruction computer.

3.1 Technical Parameters and Geometry

The mechanical setup designed for the prototype system is shown in Fig. 3.1. A radioactive source with a reasonably high activity is essential for all kinds of measurements in the laboratory. While radioisotopes with a short half-life are suitable for in vivo medical imaging, radioisotopes with long half-life are preferable for the repeatability of the measurements, longer event integration times and in order to keep costs as low as possible. Amongst the available sources, ^{137}Cs source with an activity of 1 Ci was found to be the best choice for the test system. ^{137}Cs source emits mainly γ-rays of 661.7 keV energy with a probability of 85.1% which is highly advantageous for Compton camera imaging due to a single energy peak. This makes the assumption of the known initial γ-ray energy possible. The half-life of this source is 30.07 years and this is long enough for all practical purposes mentioned above.

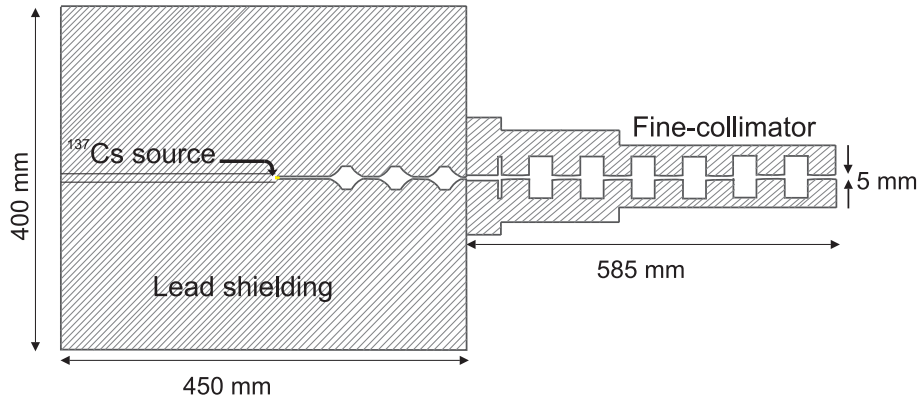

Fig. 3.2: Lead collimator used for the 1 Ci ^{137}Cs source

The ^{137}Cs source is in the form of a cylinder with a diameter of 5.5 mm and 7.1 mm height and radiates $2.5 \cdot 10^{10}$ photons per second. In order to shield and collimate this radiation, the setup shown in Fig. 3.2 is used. The background radiation caused by the beam scatter from the wall of the beam line is absorbed by a beam catcher consisting of a lead cylinder with a hole at the center which is mounted on the shielding wall. With all these precautions, the radiation level in the laboratory is measured to be of the order of the natural background radiation.

The intensity of the beam after collimation and the angular deviation of the beam has to be known for certain measurements. The beam profile is measured with a NaI(TI) scintillation detector which is placed 2.1 m away before the collimator. The beam-line is scanned with 1 mm steps using a 1 mm wide slit collimator. The measured beam profile is shown in Fig. 3.3. These measurements show that angular deviation of the beam is approximately 0.18°. The beam intensity is measured to be 120k photons per second.

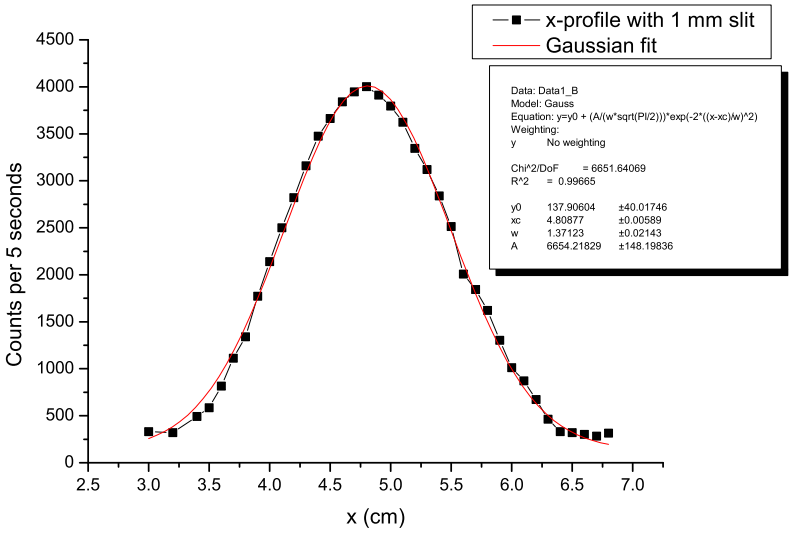

Fig. 3.3: Scanned beam profile obtained with a 1 mm wide slit collimator

3.2 Scatter Detector

The prototype Compton camera consists of a Silicon Drift Detector (SDD) as the scatter detector. SDD's have interesting properties which make them suitable for Compton cameras. Silicon by itself is the optimal material for Compton scattering at the γ-ray energy range of interest and the drift process permits lower readout channel density per unit active detector area compared to silicon pixel detectors.

3.2.1 Principle of Operation

The semiconductor drift detector was invented in 1983 by E. Gatti et al [Gat84] and it is based on a principle of sideward depletion. Depletion of the semiconductor is achieved by applying

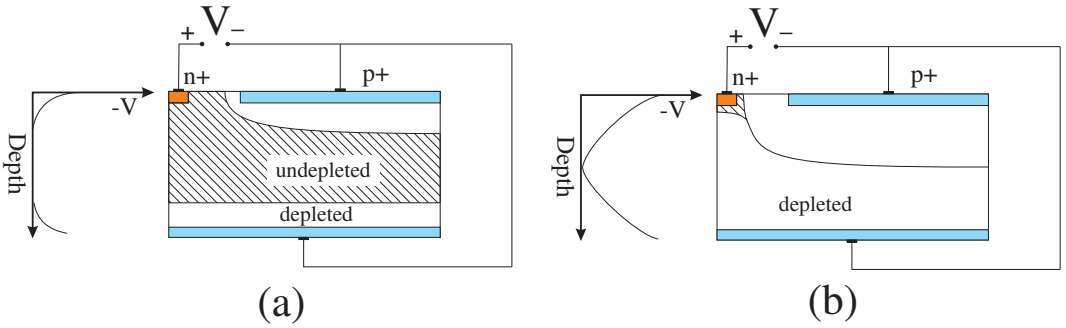

Fig. 3.4: (a) Partially depleted silicon drift diode and, (b) fully depleted drift diode.

a potential difference between the n^+ anode and p^+ contacts as shown in Fig. 3.4. Initially,

the depletion zone expands from the junctions but does not cover the whole volume of the semiconductor. As the potential difference increases the depletion zones expands from both sides of the semiconductor and joins together. Under this condition, the silicon wafer is fully depleted and the potential field, seen as crossection of the silicon wafer, has a parabolic shape as seen in Fig. 3.4(b).

The width of the depletion region can be approximated for the case where the acceptor concentration is very large with respect to the donor concentration $N_A >> N_D$ as follows:

$$w_d = \sqrt{\frac{\varepsilon_r \varepsilon_o V}{q N_D}} \tag{3.1}$$

where $\varepsilon_o = 8.8510^{-14}$ F/cm is the free-space permitivity, ε_r is the relative dielectric constant which is 11.9 for silicon, V is the bias voltage applied and N_D is typically 10^{12} cm^{-3}. The bias voltage required for fully depleting a 300 μm thick silicon wafer is around -70 Volts.

Using the depletion principle described above, this type of detector can be extended to cover large areas with additional electric field component parallel to the surface of the silicon. This additional field creates a potential valley in the anode region of the detector as shown in Fig. 3.5. This field can be created by dividing the upper surface of the silicon into multiple p^+ regions and applying a potential difference distributed by a resistor array at each of these regions.

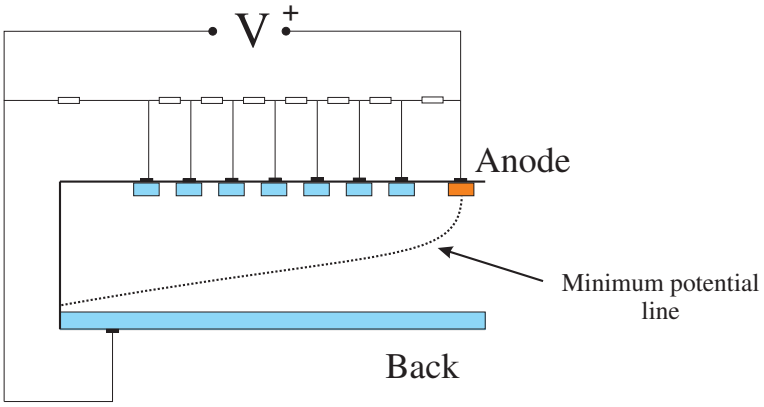

Fig. 3.5: Silicon drift detector and the potential minimum

Signal generation in a silicon drift detector is similar to gas drift chambers. When a γ-ray interacts within the detector's sensitive volume, electron hole pairs are generated as shown in Fig. 3.6. The number of electron-hole pairs is proportional to the energy deposited by the interaction. As the detector volume is fully depleted, electrons move quickly to the potential minimum and holes move to p^+ regions, especially to the back side as it is at the most negative potential, and generate weak induced signal on the negative electrode. Electrons drift toward the anode due to the drift field.The low noise "count" of the collected electrons provides a precise measurement of the energy deposited in the detector volume after the drift time. The moment of interaction can be calculated by considering the mobilities of electrons and holes for a given silicon wafer and measuring arrival times of the back and anode signals assuming that no other

interaction occurs during the drift time. Typical drift times for 300 μm thick n-type detector grade silicon wafer is .1 to 1 ns per 1 μm depending on the drift potential.

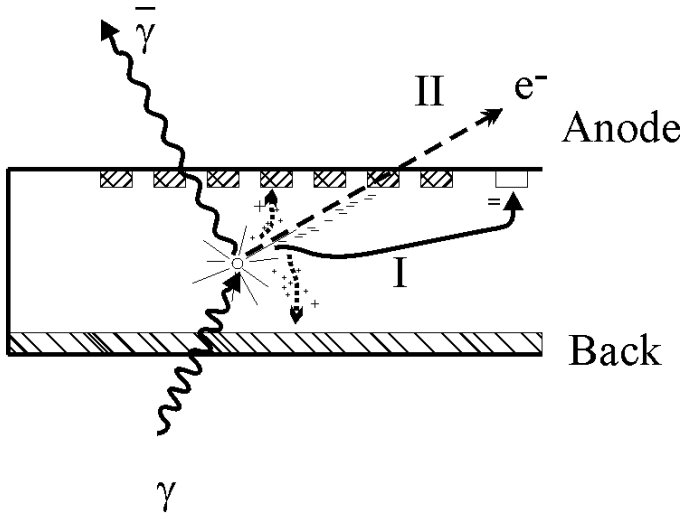

Fig. 3.6: A Compton interaction in the SDD and the path of the electrons

3.2.2 19 Cell Silicon Drift Detector

The silicon drift detector (SDD) used as a scatter detector is a monolithic array of 19 cells with an on-chip junction field effect transistor (JFET) for the first amplification integrated on each cell. It has been produced by the Max Planck Institute Semiconductor Laboratory (MPI/HLL) [MPI]. The most significant feature of this detector is the on-chip integrated JFET which serves to reduce the stray capacitance and therefore provides a better noise performance compared to other silicon detectors (Fig. 3.7). Integrated JFET provides the initial amplification as follows.

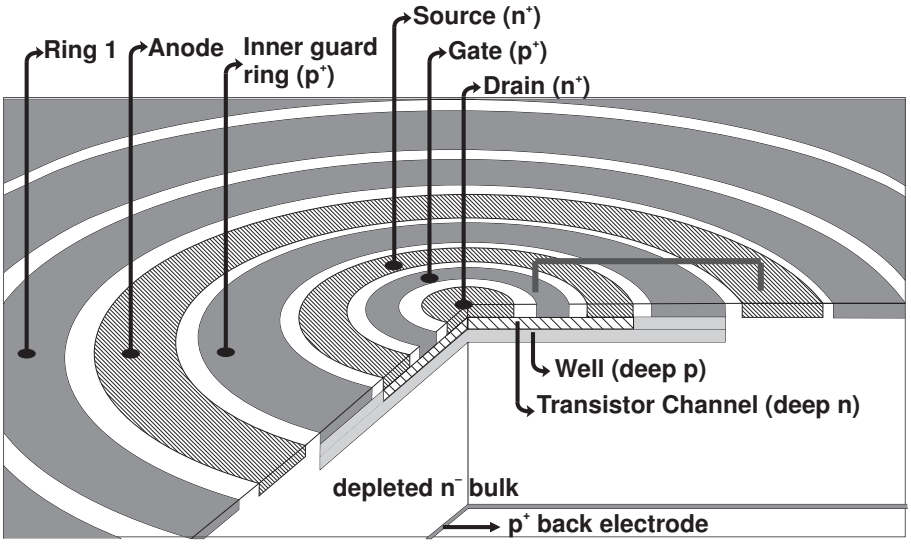

Fig. 3.7: Silicon drift detector with integrated JFET

The readout node, where the electrons arrive, is coupled directly to the p^+ gate of the n-channel

JFET. Due to the negative potential on the gate, the channel of the transistor starts to turn off resulting in a current drop through the transistor which can be measured precisely when it is operated with a constant current source.

The energy resolution of each drift cell can be defined empirically as follows [Str00]:

$$\Delta E_{FWHM} = 2.355 \times e_p \times \sqrt{ENC^2 + \frac{F \times E}{e_p}} \tag{3.2}$$

where E is the total γ-ray energy, e_p is the pair creation energy which is the average energy required to create an electron-hole pair, ENC is the equivalent noise charge in electrons rms, F is the Fano factor and 2.355 is the conversion factor between the standard deviation and the full width at half-max (FWHM). The energy resolution of the SDD can be as high as 150 eV with $F = 0.115$, $e_p = 3.65$ eV, an incident γ-ray energy of $E = 6$ keV, and a readout noise of 10 electrons rms (root-mean-square) at room temperature. The readout noise is mainly defined by the characteristics of the on chip JFET and cooling improves its properties. By reducing the temperature to -20 degress the readout noise reduces to 5 electrons rms and the energy resolution becomes 125 eV FWHM which is considered to be excellent for this type of detector.

3.2.3 Mechanical Setup

The mechanical setup has been designed to meet the following requirements:

1. The material along the beam-line should be minimized except in the active detector area itself. Any material along the beam-line leads to the multiple scattering of photons and may result in some unwanted radiation in the laboratory which is not allowable in terms of radiation safety requirements.

2. The scatter detector chip should be mounted such that it should be possible to replace it easily if the need arises.

3. The scatter detector frame and surrounding electronics should allow us to cool the whole detector system down to zero degrees, and to have a temperature controlled environment in order to study temperature effects and the effect of changes in the leakage current on the detector performance.

4. The scatter detector system should be placed on a computer controlled moving stage in x and y coordinates in the laboratory frame as proposed in Fig. 3.1. This is needed in order to make measurements on each detector cell and to scan the whole detector surface with extra finely-collimated γ-rays.

The implementation of the first requirement is achieved by designing the setup for the scatter detector chip and the readout electronics surrounding it. The layout plan of the 19-cell silicon drift detector wafer provided by Max-Planck Institute (MPI) semiconductor laboratory can be seen in Fig. 3.8. As no experimental setup has previously been build with the mechanical

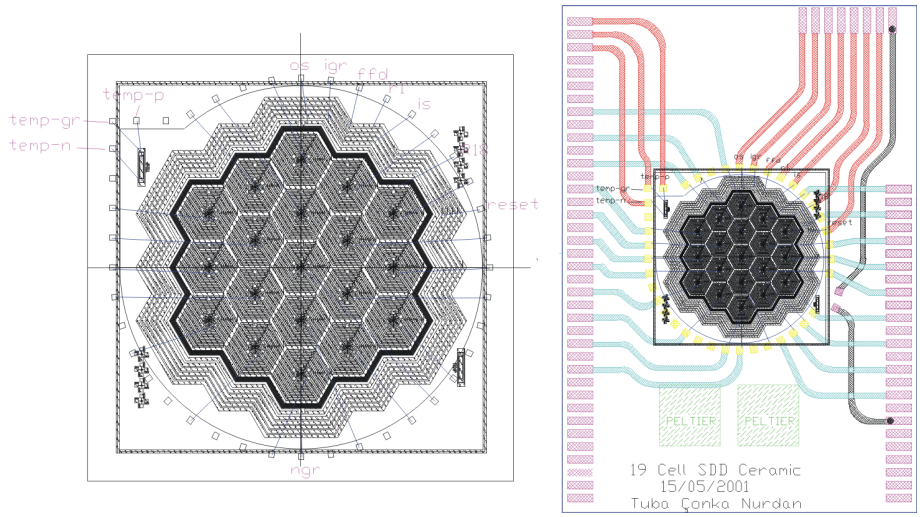

Fig. 3.8: SDD cell bonding plan and the ceramic board designed for detector mounting

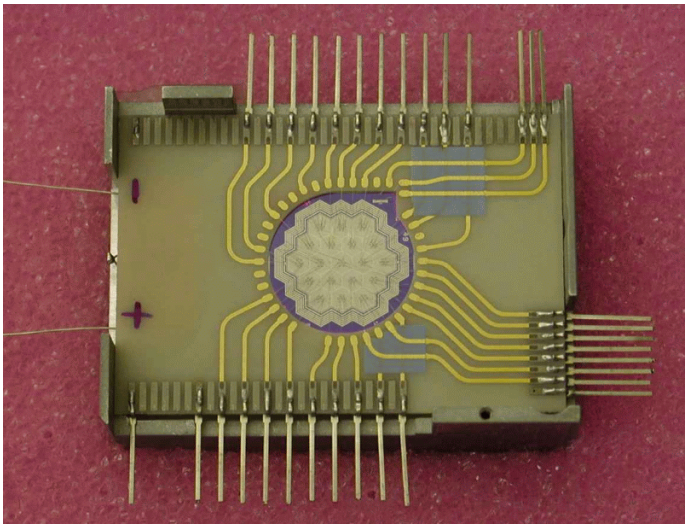

Fig. 3.9: Silicon detector as it has been received from MPI

requirements of the Compton camera prototype, a new bonding plan and the carrier ceramic had to be designed in Siegen.

After a careful study of the pad positions on the detector and power requirements, a suitable bonding plan and a carrier ceramic with gold plated signal tracks have been designed as shown in Fig. 3.8. The bonding was first performed on a dummy wafer [Hon00] successfully and with the help of this sample the real detector chip was bonded at Ketek [KET]. This design allows both faces of the detector to be open and minimizes the unwanted material such as the mechanical frame and low-noise readout electronics along the path of incoming and scattered γ-rays.

The ceramic material itself is chosen to be Aluminum-Nitride (AlN) which has a heat expansion constant very close to that of a silicon and a very good heat conduction coefficient. This makes the thermal control of the detector easier using small peltier elements which are thermally coupled to the ceramic. Measurements performed with two different ceramic materials showed

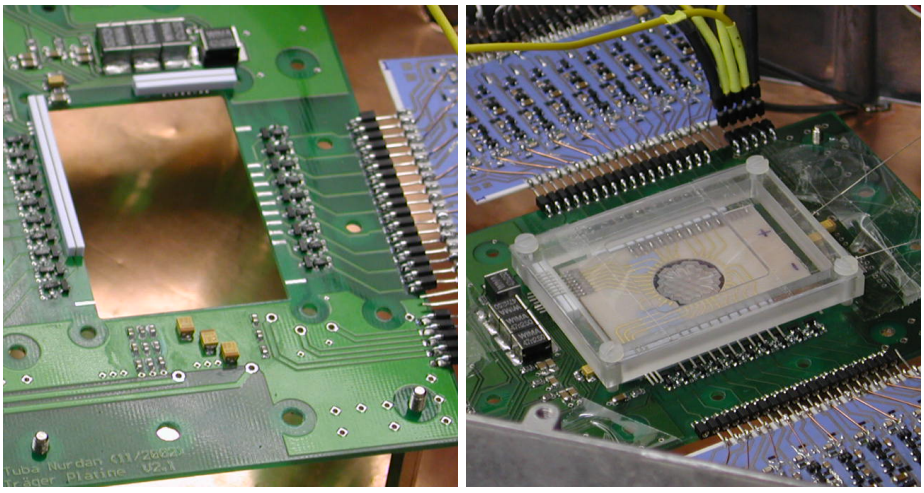

(a) Carrier PCB with two white rubber interconnectors

(b) Carrier PCB with the detector mounted in the test box

Fig. 3.10: Two detail images showing how rubber interconnects are applied to the detector and carrier PCB

a temperature gradient of the order of 9 degrees with a standard Aluminum-Oxide (Al_2O_3) ceramic, while only few degrees of temperature gradient was observed with AlN. The gold signal tracks and pads provided efficient connection for the bond wires. The final detector chip bonded on the AlN carrier ceramic is presented in Fig. 3.9. In order to fulfill the second requirement a carrier printed circuit board (PCB) with the first stage front-end readout electronics and power supply regulators has been designed (Fig. 3.10).

At the initial design stage, zero-force connectors were thought to be a practical choice for connecting the detector ceramic to the carrier PCB. The commercial connectors could not fulfill the area and size requirements for the design as they were too large to be used in the mechanical setup designed for the detector housing. The alternative solution was to use special interconnection rubbers used for LCD displays. These rubbers have a single row of gold plated brass rods of 30 μm width with a spacing of 100 μm between the rods. The height of the rubber can be between 1-10 mm, thickness is 3 mm and the length can be as long as it is desired (Fig. 3.10(a)).The detector ceramic is then placed between a transparent plexiglass frame and rubbers and compressed with the help of plastic screws from the edges as shown in Fig. 3.10(b).

In order to study the temperature dependence of the detector, a special housing is designed which enables the assembly to be watercooled. The CAD design of the housing can be seen in Fig. 3.11. The carrier PCB is positioned inside this metal housing with O-rings which provides also a gas tight environment. Pure nitrogen gas is flushed into the housing in order to prevent condensation of water on the detector when the detector is cooled below the dew point. The final mechanical setup with the whole front end electronics and the detector housing is placed on an X-Y motor stage which is computer-controlled. In Fig. 3.12 the silicon detector housing can be seen at the center, two metal boxes on the left and right hand side contain 10 channels

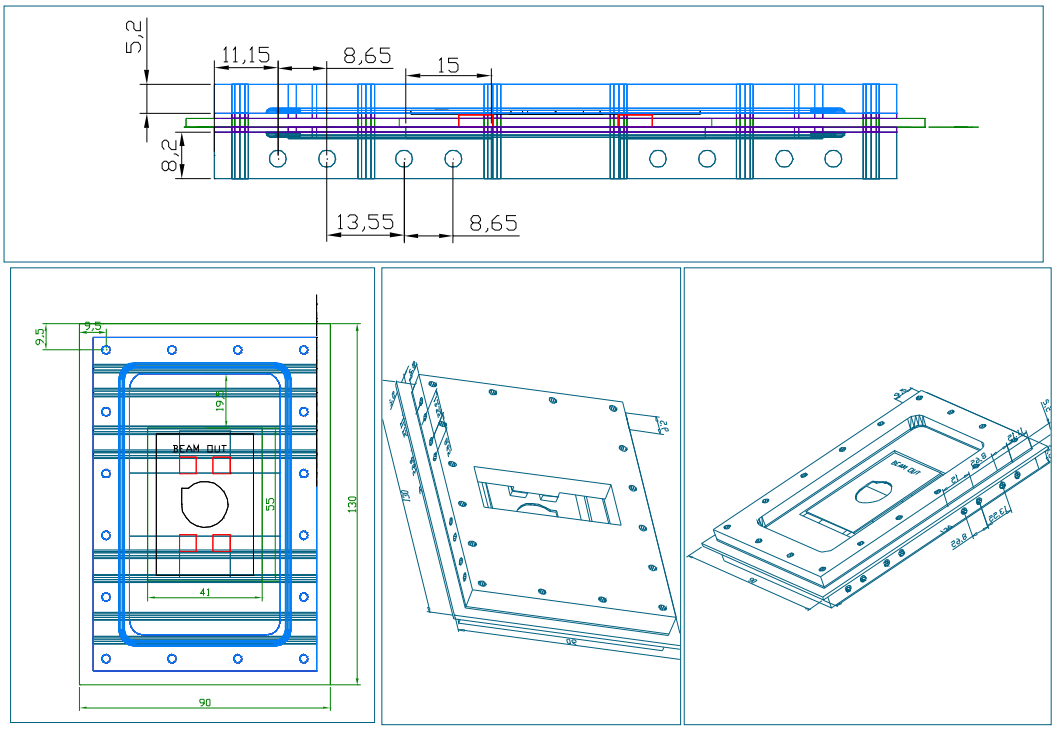

Fig. 3.11: CAD design of the gas-tight housing enabling water flow for cooling the hot side of the peltier elements

of low noise preamplifiers and shapers each. These metal boxes protect the low noise electronics from external electro-magnetic interference.

3.2.4 Front-end Electronics

Front-end Electronics (FeE) carries and manipulates signals starting from the detector's on-chip JFET to the point where the signal has been amplified, shaped and ready for conversion into digital words. Several requirements for achieving a good system performance have been considered in designing the FeE. First of all, the energy of the recoil electron should be measured as precisely as possible since this precision improves the quality of the reconstructed image. For this reason, the FeE for the scatter detector should add as little noise as possible to the original signal. Also, the cross-talk between the channels of the readout electronics and an external interference to them should be avoided. SDDs are usually used for an x-ray spectroscopy where the energy of the photon is at most around 60 keV. However, for the Compton camera application, the energies to be measured are much higher than this range (as high as few hundred keV) and this requires an electronics with a dynamic range which is wide enough to enable the measurement of the whole spectrum of energies. The time resolution of the scatter detector is another important parameter which helps to effectively eliminate accidental coincidences. Therefore, the FeE should provide good time resolution. The FeE is divided into three major parts as it can be seen in Fig. 3.13 and the details of each part can be found in the PhD thesis of T. Çonka Nurdan [ÇN04a].

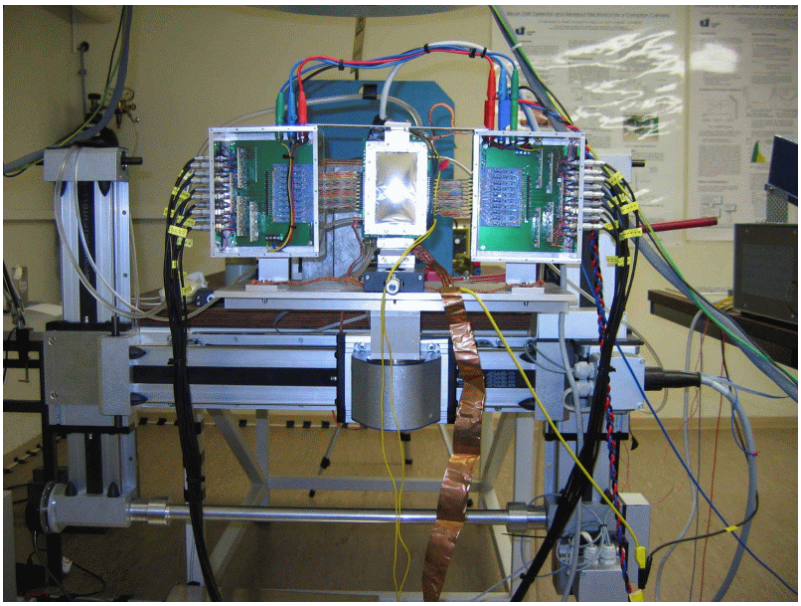

Fig. 3.12: Stage of the silicon detector

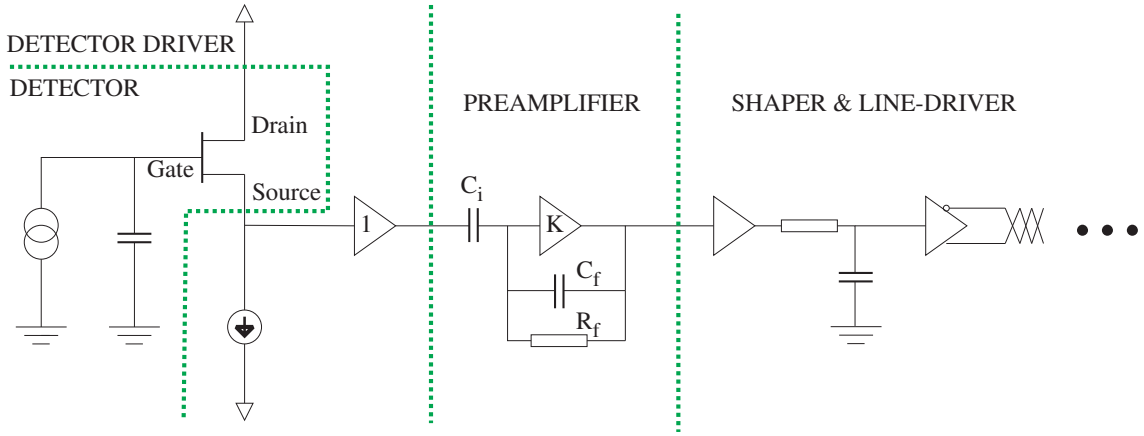

Fig. 3.13: Block diagram of the front-end electronics

1. Detector Driver: This part provides the required bias voltages to the on-chip JFET and includes an impedance converter stage.

2. Preamplifier: This is a low noise voltage sensitive amplifier (VSA). It acts as a high-pass filter and amplifies voltage changes.

3. Shaper: It consists of a differentiator and an integrator. Integration is essential due to the fact that the total energy is proportional to the number of electrons produced by the interaction. The shaper converts voltage steps into semi-gaussian shaped pulses where the amplitude of the pulses are proportional to the deposited energy of the interaction in the SDD.

3.2.4.1 Detector Driver

The SDD can be modeled as a current pulse generator that is attached to the gate of the on-chip JFET. In order to sense these current pulses the on-chip JFET is driven by a constant current source. When there is no signal, the V_{ds} (drain-source voltage) of the on-chip JFET is constant, which is defined by the transconductance (g_m) of the JFET times the constant current. When there is a signal, the V_{ds} changes proportionally.

Traditionally the source of on-chip JFET is connected directly to a voltage sensitive preamplifier in order to amplify the signal. This produces a signal rise time of around 300 ns which is approximately formulated as:

$$t_r = 2.2 \times \frac{1}{g_m} \times [C_{\text{parasitic}} + C_{\text{preamp}}] \tag{3.3}$$

where $C_{\text{parasitic}} \approx 3$ pF and $C_{\text{preamp}} \approx 20 - 40$ pF depending on the desired amplification. The g_m of the on-chip JFET, which is the effect of the gate voltage upon the drain to source current ($\partial I_{ds}/\partial V_{gs}$), is given to be approximately 0.3 mho. The rise-time of the detector had to be improved in order to meet the design criteria.

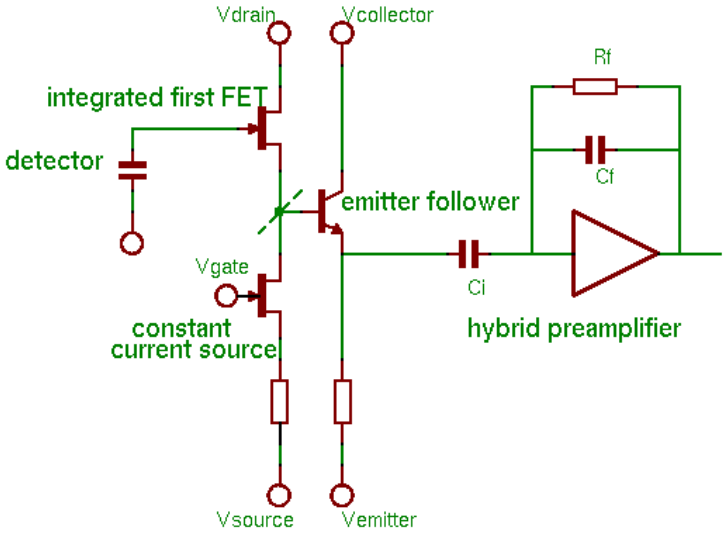

Fig. 3.14: The new readout architecture for the SDD with an additional emitter follower stage following the on-chip JFET

An alternative detector driving architecture shown in Fig. 3.14 has been introduced [ÇN04a] which had been used successfully for gas proportional counters [Far83]. An emitter follower stage is inserted between the preamplifier and the source of the on-chip JFET. The advantage of this stage is, if implemented properly with a low-noise bipolar transistor, that the overall capacitance given in Eq 3.3 can be reduced significantly. The base capacitance $C_{\text{be}} \approx 2$ pF of the emitter follower stage now replaces the C_{preamp} which shortens the rise time nearly 5 times as shown in Fig. 3.15.

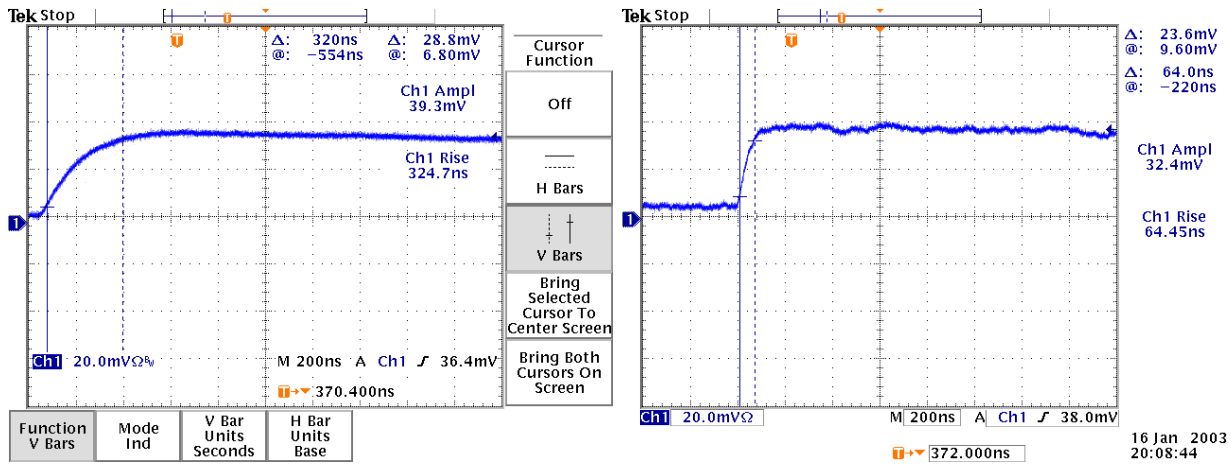

(a) Preamplifier output without the emitter follower stage

(b) Preamplifier output with the emitter follower stage

Fig. 3.15: The output of the preamplifier with and without the emitter follower stage

3.2.4.2 Preamplifier

The preamplifier is a modified version of a preamplifier which was used for one of the first prototype SDDs [Ch.96]. The gain of the preamplifier is approximately the ratio between the

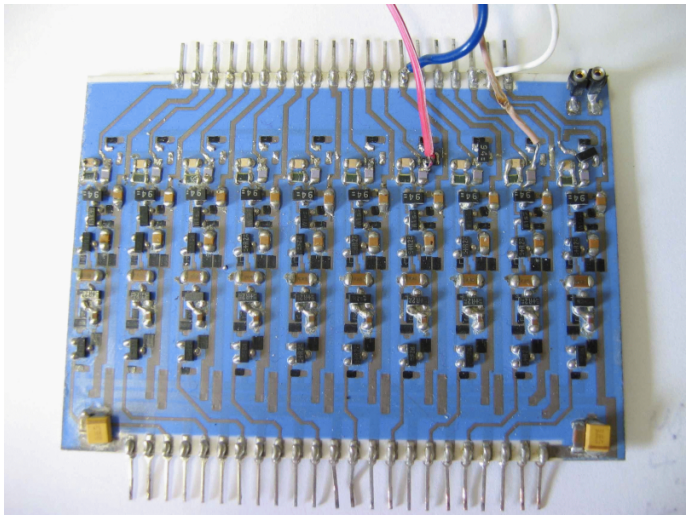

Fig. 3.16: Hybrid preamplifier implemented on a ceramic with thick-film and SMD technologies

injection capacitor (C_i) at the input and the feedback capacitor (C_f) as illustrated in Fig. 3.13. The voltage step at the output of the preamplifier decays with a time constant of $R_f \cdot C_f = 100\mu s$.

Ten channels of the preamplifier have been implemented on a hybrid board using thick film technology. One of the ceramics that has been built can be seen in Fig. 3.16. The power consumption of each preamplifier is around 130 mW and the total power consumption is around 1.4 W according to the SPICE simulations. As the ceramic material is very good at conducting

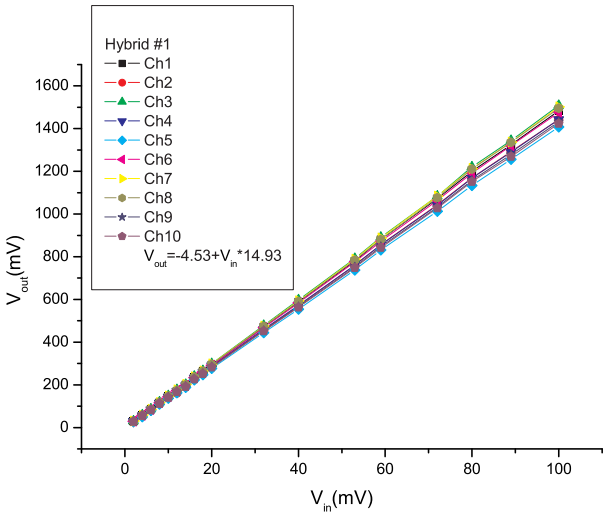

Fig. 3.17: Linearity of the 10-channel preamplifier board

the heat, there is no need for extra cooling. The linearity of the 10-channel preamplifier is shown in Fig. 3.17. The deviation from linearity is 0.5% in the worst case and better than 0.2% on the average. These measurements were done by applying a voltage step at the input of each preamplifier channel and measuring the output. The average voltage gain is around 15. The simulations show that the dynamic range of the preamplifier system corresponds to an energy range of 0-400 keV. This energy range was acceptable for the measurements as the maximum possible energy deposition for an 662 keV γ-ray is around 430 keV which is rare. Also, because of the geometrical constraints of the prototype system, it was not possible to capture Compton interactions with recoil electron energies greater than 300 keV.

3.2.4.3 Shaper

An in house developed hybrid shaper shown in Fig. 3.18 is used for the measurements. The shaper is a CR-RC shaper with an adjustable pole-zero cancellation and gain. The hybrid board has two shaper channels and 10 of these boards have been used for the 19-cell SDD setup.

The block diagram of the shaper is shown in Fig. 3.19. There is a differential amplifier with a variable gain (g) at the first stage. It is followed by a pole-zero (pz) filter and an integrator (int) and finally a differential output stage follows. Certain aspects were taken into account when choosing the appropriate shaping time. The rise time of the preamplified signal is about 60 ns. The shaping time should not be much shorter than this value in order to avoid loss of signal due to ballistic deficit. The sampling rate of the ADC system is 66 MHz and at least 4 samples should be taken at the region of highest signal to noise ratio. The leakage current of this detector is not the dominating factor, therefore the energy resolution improves with an increasing shaping time. However, it can not be made very long, since fast signals are needed for an accurate coincidence measurement. Considering these constraints a peaking time of 100

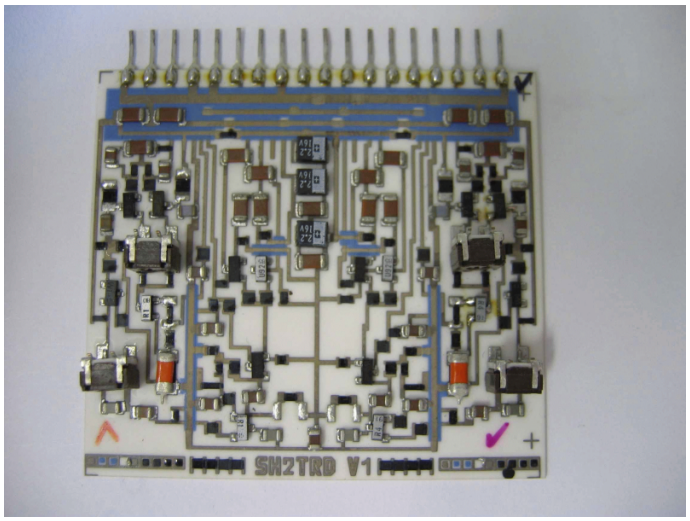

Fig. 3.18: Shaper Ceramic

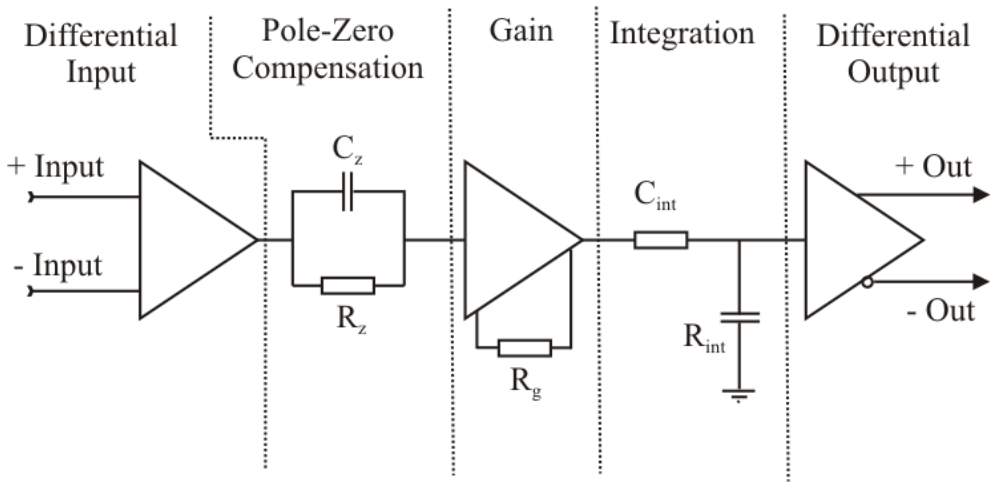

Fig. 3.19: Block diagram of the shaper

ns was chosen.

The FeE is followed by a data acquisition (DAQ) system which is developed for this Compton camera prototype [Nur03b, Nur03a] and this system will be explained in greater detail in the next chapter.

3.2.5 Measurements & Calibration

The calibration measurements have been performed in order to find the relationship between measured values and the related physical quantities. The quality of the measurements and the overall performance of the signal pipeline starting from the SDD to the final data file transferred to a DAQ computer have also been verified. The calibration process is performed for all the channels. This process requires at least two known radioactive sources whose energy spectra are to be measured. These measurements are then compared with the reference spectra for

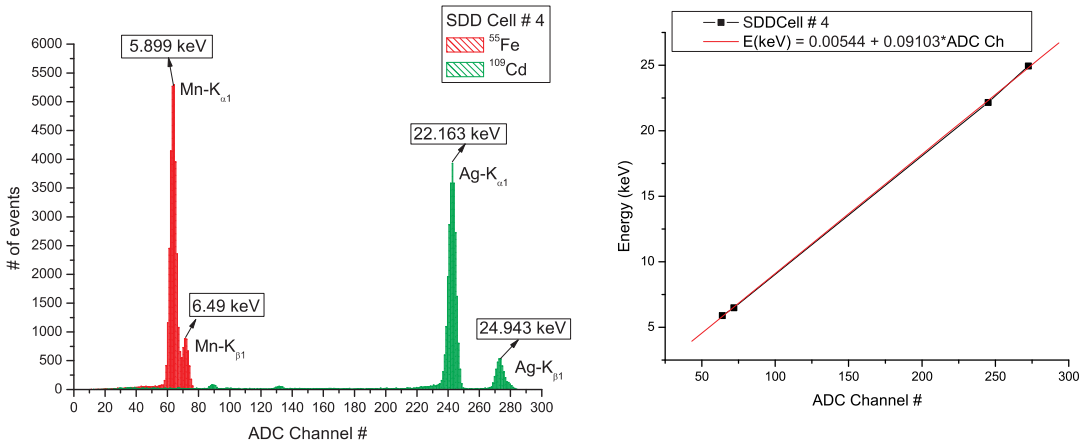

(a) ^{55}Fe and ^{109}Cd spectrum measured with SDD channel 4

(b) Energy resolution as a function of a shaping time

Fig. 3.20: Spectrum measurements and the calibration curve obtained for one of the SDD channels

extracting the relation between the data points and the energy values.

^{55}Fe and ^{109}Cd sources are used for the calibration of all the SDD channels as they are available in the laboratory. Two typical spectra measured with the SDD channel 4 are shown in Fig. 3.20(a), where both Mn K_α and K_β peaks of ^{55}Fe can be seen clearly. The calculation of

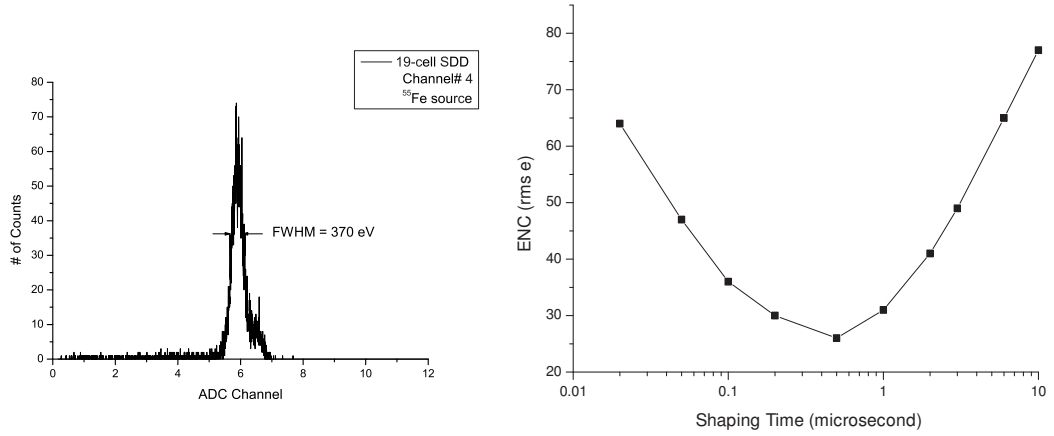

Fig. 3.21: Energy spectrum of ^{55}Fe measured with a shaping time of 100 ns and the variation of the ENC with respect to the shaping time

the linearity is performed by first fitting gaussian functions to the energy peaks in the measured data, then taking their mean values and pairing them with the known energy peaks from the reference spectra. The result of a typical energy calibration curve is shown in Fig. 3.20(b).

The equivalent noise charge (ENC) is about 33 electrons rms at 10°C which includes noise contributions from the detector and the electronics. Fig. 3.21 shows the energy resolution at 5.9 keV as a function of the shaping time. The FWHM value is about 250 eV at a shaping time

of 250 ns and increases with shorter and longer shaping times.

3.3 Absorption Detector

A refurbished Anger camera is used as the absorption detector of the prototype Compton camera system. The Anger camera has been chosen due to the fact that it covers a large solid angle for the scattered photons, the readout of the camera is very simple and refurbished Anger cameras can be obtained at a reasonable cost.

3.3.1 Operation Principles

The Anger camera consists of a single scintillation crystal of NaI(Tl) which is coupled to photomultiplier tubes. The scintillators emit light in the visible wavelength range which is proportional to the amount of energy deposited in the material. Unfortunately the efficiency of this process is rather low and the statistical fluctuations in the number of emitted photons influence the time and energy resolution of the measurements. Therefore very sensitive photo detectors have to be used. Photomultiplier tubes (PMT) have single photon sensitivity and are suitable for this purpose.

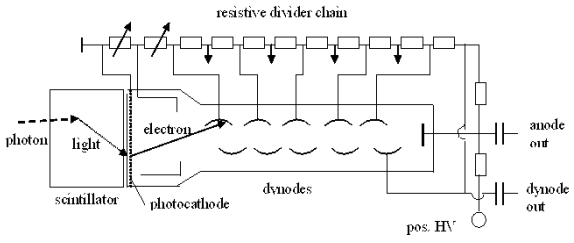

Fig. 3.22: Photo Multiplier Tube with a scintillator material attached to it.

The principle of operation of a scintillator detector is shown in Fig. 3.22. The incoming γ-ray when interacting within the scintillator, creates many low energetic (≈ 3 eV) scintillation photons in the visible light spectrum. These photons are transmitted via a light guide to the PMT which is carefully coupled to the scintillator using optical grease. As they arrive at the PMT, each of them has the possibility of producing a single electron at the photocathode via the photoeffect process with an efficiency of the order of 20%. For the generation of these low energy photons in a NaI(Tl) scintillator an energy deposition of about 25 eV is required.

The electrons that are generated in the photocathode of the PMT are guided to the first dynode and accelerated at the same time by the electric field generated between the photocathode and this electrode where they undergo multiplication via secondary electron emission. Since the focusing and accelerating properties at the first dynode are the most critical for the performance of the tube, the voltage of this stage is usually accessible and can be externally adjusted. The voltages at the following dynodes vary in an increasing manner (mostly realized by a resistor chain) and they multiply the number of arriving electrons further. The gain of the whole dynode chain can be regulated by the total applied voltage to the resistor chain and it is around $10^6 - 10^8$.

3.3.2 Anger Camera

The absorption detector used in the prototype is a refurbished Anger camera previously used for SPECT applications. It consist of a NaI(Tl) crystal which is 15 inches in diameter and

Fig. 3.23: Anger camera without a collimator

3/8 inches thick. This crystal is coupled to 37 PMTs of 3 inches in diameter. The PMTs are arranged in a hexagonal grid in order to maximize the covered area of the scintillator. The Anger camera can be seen in Fig. 3.23.

In Anger camera position information is generated as follows: PMT pulses are fed through a summing matrix where four analog signals are generated. These signals are called x^+, y^+, x^- and y^-. The summing matrix combines the signals in such a way that relative amplitudes of the four generated signals are proportional the position of the interaction which takes place in the scintillator. This method is called center of gravity or Anger logic which can be defined for a signal instance as follows:

$$x^+ - x^- = \frac{\sum s_i w_i}{\sum s_i} \tag{3.4}$$

where s_i is the i'th PMT signal and w_i is the positional weight assigned for the i'th PMT. The same formula applies for all of the signals. After this initial process, the signals are amplified and shaped again for further decoding. The schematics of the signal flow is shown in Fig. 3.24.

The energy signal is inherently coupled with the position signals generated by the analog front-end of the Anger camera. In order to calculate the position, independent of the energy signal, the following formulation has been used,

$$x = k_x \times \frac{X}{E_{cor}} \tag{3.5}$$

$$y = k_y \times \frac{Y}{E_{cor}} \tag{3.6}$$

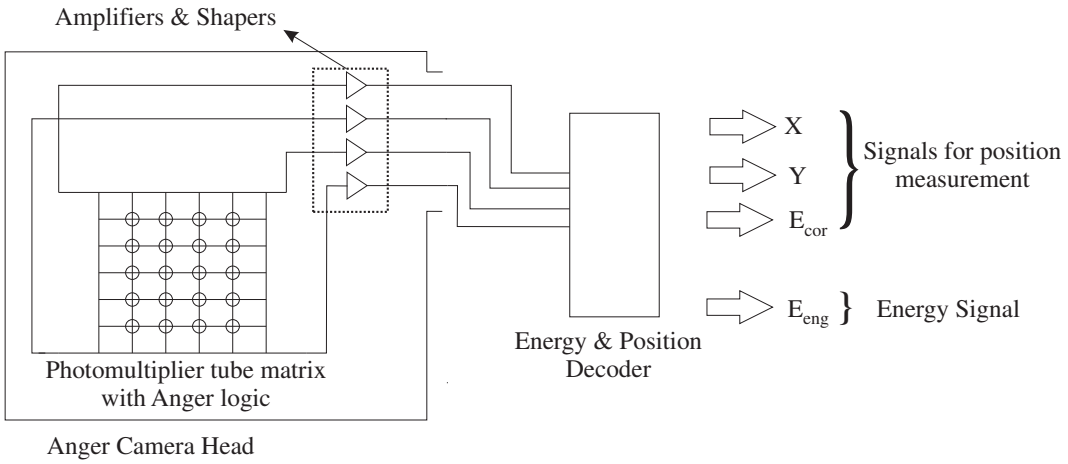

Fig. 3.24: The conceptual view of the Anger camera frontend electronics

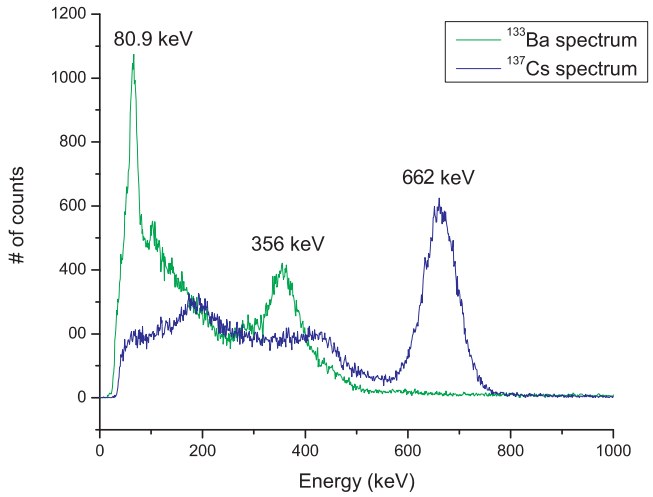

Fig. 3.25: ^{137}Cs and ^{133}Ba energy spectra measured with the Anger Camera

where E_{cor} is the corrected energy signal, k_x and k_y are empirical constants that need to be determined experimentally. The energy spectrum of the incoming γ-rays are obtained by using the energy signal (E_{eng}) signal.

3.3.3 Measurements & Calibration

The calibration measurements for the Anger camera are performed in two steps. In the first step energy signal is scaled and calibrated using two different radioactive sources. The primary source was a ^{137}Cs source which is also used for coincidence measurements, and the secondary source was a ^{133}Ba source which has energy lines in the middle of the desired energy range. The spectra obtained from both sources are superposed in Fig. 3.25. The mean energy resolution measured from these spectra is around 11% at the photopeak of ^{137}Cs source.

After the energy signal is calibrated, it is possible to calibrate the X-Y position signals in order to get 2D position information. Using the intrinsic position resolution of the Anger camera

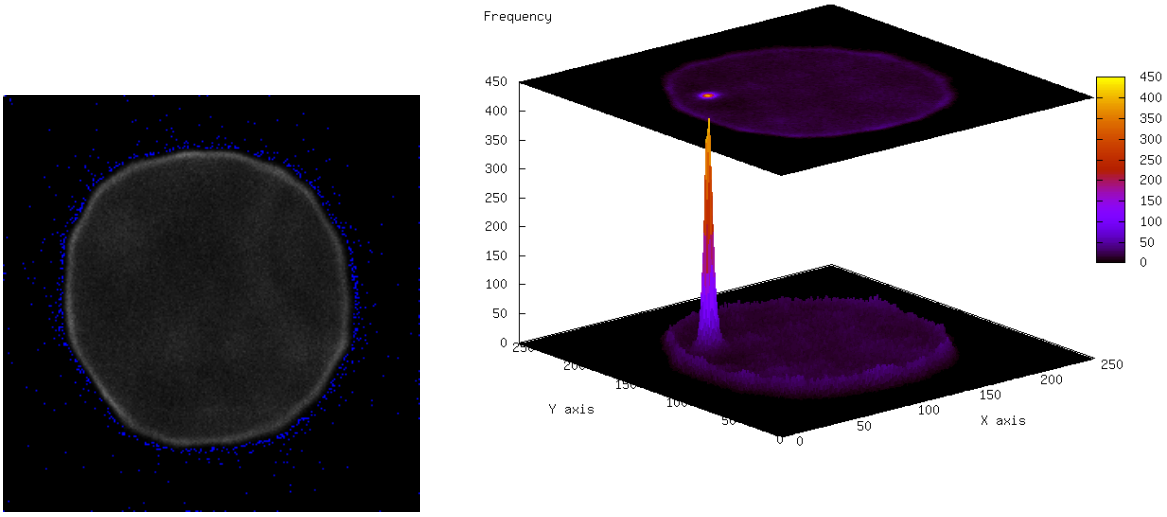

(a) (b)

Fig. 3.26: Two positional images obtained from the Anger camera. In (a) 2D image of the background noise and in (b) a point like source positioned at PMT 10 can be seen.

which was given to be around 3 mm in the users manual, and considering the diameter of the detector which is 400 mm, it has been determined that quantizing the position information into 133 quantization levels would be enough as it is not possible to get a better resolution than the intrinsic resolution. The nearest power of 2 greater than this number was 256, so it has been decided to use 256 $\times$ 256 matrix to represent the 2D position.

After collecting enough statistics and assigning an empirical value of 1.7 $\times$ 256 to k_x and k_y in Eq 3.6, the results shown in Fig. 3.26 have been obtained. A more precise correction algorithm using the result of these measurements performed for each of the 37 PMTs, will be available in the master thesis of J. Lu [Lu05].

3.3.4 Timing Properties of the Anger Camera

Timing properties and timing uncertainty in determining the interaction time in the Anger camera has been studied with the setup illustrated in Fig 3.27. As the silicon drift detector has a maximum drift time of 300 ns before the event is registered which translates directly into timing uncertainty, it is important to know how much the Anger camera will contribute to the overall timing uncertainty. This setup is also a coincidence measurement setup where the silicon detector is replaced with a plastic scintillator detector which is much faster than the silicon detector. The plastic scintillator is a cylinder with a diameter of 19 mm and it is 6 mm thick. The Anger camera provides a fast trigger signal as well as the energy and coordinate signals. The coincidence measurements were performed both with the fast trigger signal and the energy signal of the Anger camera. In the coincidence measurements with the silicon detector

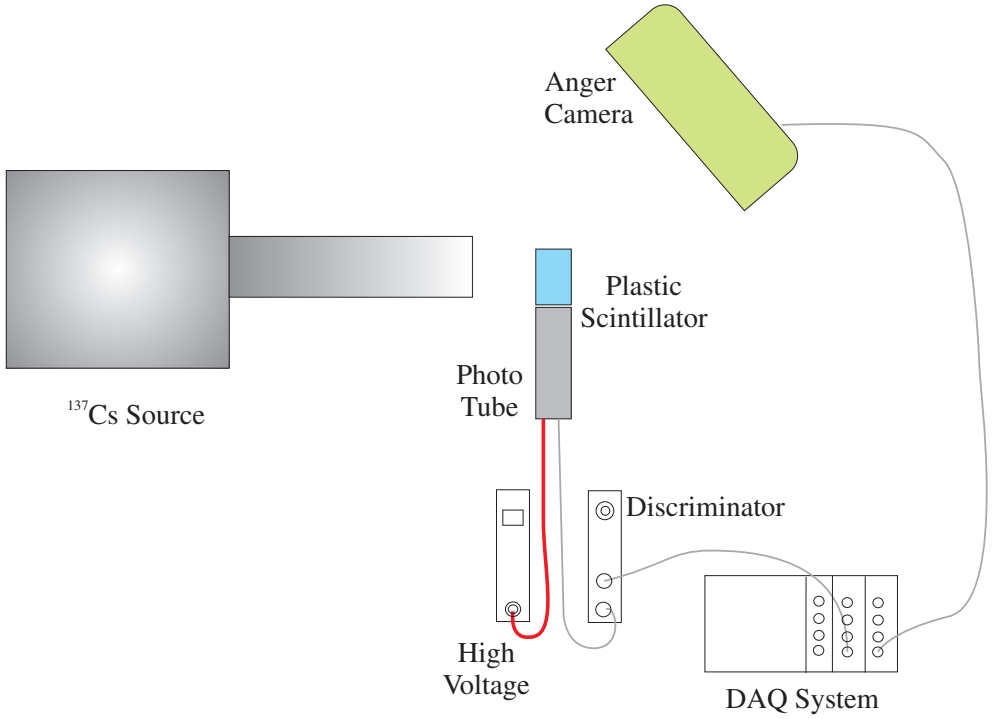

Fig. 3.27: Experimental setup for the measurement of the Anger camera's timing characteristics

it has been decided that the Anger camera timing is determined from the energy signal, so this measurement should also show the additional timing uncertainty contributed by the energy signal as well. For these measurements, the DAQ system is programmed to acquire all the events from both detectors without applying the time-coincidence logic. After the acquisition of the data, the time stamps from both detectors are subtracted and the time coincidence curve shown in Fig. 3.28 has been obtained. Due to the slower nature of the Anger camera electronics, the Anger camera signals arrive approximately 200-250 ns after the signals of the plastic scintillator. It should be noted that the fast trigger signal arrives 60 ns before the energy signal. The FWHM of both distributions are approximately 45 ns which corresponds to the time resolution of the Anger camera. It is also observed that the timing information of the energy signal can be used since it does not degrade the timing distribution and additional delay which can be compensated easily. The DAQ system has digital delays and it is possible to compensate delays up to $\pm 3\mu$sec.

3.4 Final Prototype System

The final Compton camera prototype with the 19-cell SDD and the Anger camera is shown in Fig. 3.29. A ^{137}Cs source is placed in a lead collimator which provides both the shielding and the fine collimation for the photons emitted. The silicon detector and its front-end electronics placed in metal boxes are mounted on a motor-controlled stage which enables their rotational and 2D translational motion. In this way, Compton electrons in all directions and kinematics can be studied. The distance between the source and the surface of the scatter detector is around 120

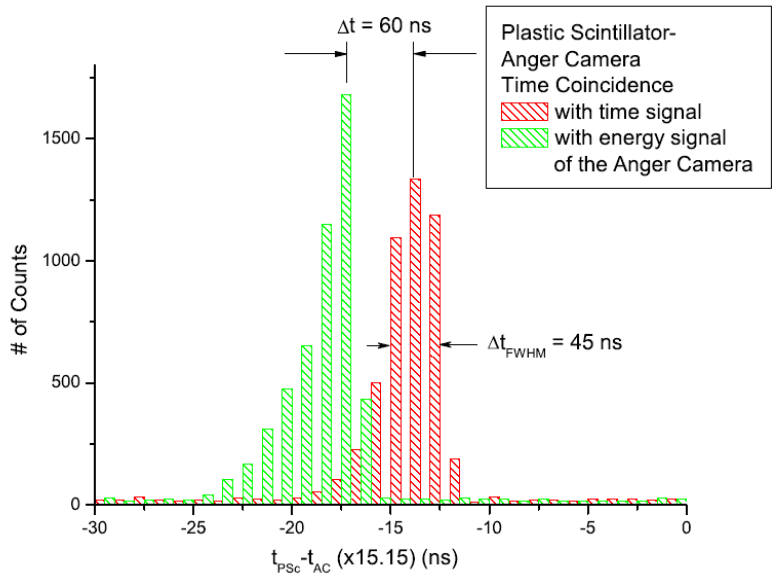

Fig. 3.28: Time coincidence curve obtained by subtracting the time stamps of the events occuring in the plastic scincillator from the time stamps of the Anger camera events

cm. In addition to the embedded motor system of the Anger camera, another degree of freedom is added to its motion by placing it on a moving stage which provides translational motion of the camera as a whole. In this way, the inter-detector distance can be varied easily and not only forward scattering region but also the back-scattering region can be covered. The complete chain of analog and digital readout electronics for the SDD and the Anger camera has been tested and calibrated in order to measure Compton coincidences from which the reconstruction of events and images are to be obtained.

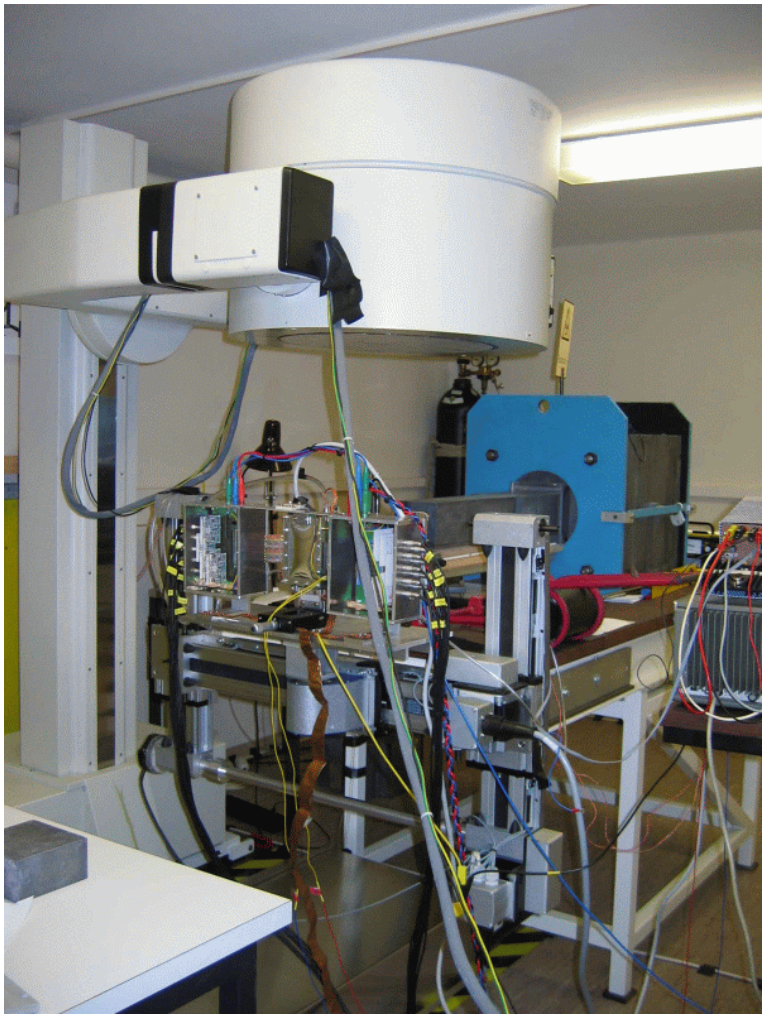

Fig. 3.29: Overview of the prototype system

Chapter 4

Data Acquisition System

In this chapter the data acquisition system designed for the Compton camera prototype is presented.

Time coincidence processing is the heart of any Compton camera data acquisition system. In the previous Compton camera designs [Hua00b] coincidence processing was performed by a hardwired logic. This reduces the processing requirements but it may not fulfill the timing requirements of the detector systems having drift detectors like the Compton camera prototype system discussed in this work. The coincidence processing based on the hardwired logic is definitely not appropriate for Si(Li) detectors [Pro04] where the interaction time can only be calculated after processing the multiple signals coming from silicon drift detectors with large drift times.

A novel data acquisition concept has been introduced in order to fulfill these timing and coincidence requirements and a data acquisition hardware supporting this concept has been designed. This new concept is based on time tagging each event fragment in any detector and identifying Compton events later with the help of a coincidence processor. Although this concept requires more processing power, and a high speed data transmission between detector subsystems and the coincidence processor, its benefits surpass these requirements. It is even possible to add certain energy and geometrical constraints to the coincidence processor which improves the quality of the output and reduces the number of false coincident events. To our knowledge this idea has not been applied to any other Compton camera system and here it is shown that in this work it has successfully been implemented and it fulfills the expected performance.

4.1 High Level Design

Within this framework a Compton Camera DAQ system [Nur03b, Nur03a] has been designed and constructed which consists of two detector subsystems for the scatter and absorption detectors, and an event builder (EB) unit. Each detector subsystem may also be divided into smaller detector subsystems. The realization of such a scenario is performed in three major parts;

- Channel Processors: They process incoming analog detector signals. These signals are

fragments of an event and may carry position and/or energy information of the interaction occurred inside the detector.

- Data interconnect: It creates a reliable and fast digital connection between different parts of the data acquisition system for the data configuration and control signals.
- Event Builder: It retrieves event fragments from channel processors, combines fragments belonging to the same event by a time-coincidence method, reformats and stores reconstructed events for more advanced processing and image reconstruction. It then transfers reconstructed events to the data acquisition computer.

The parts of the conceptual DAQ system and the interactions between the components are illustrated in Fig. 4.1. During event data flow from detectors to the event builder, the control and configuration signals are initiated by the event builder. Signals that may be used for monitoring the status of the DAQ system may be added to this illustration.

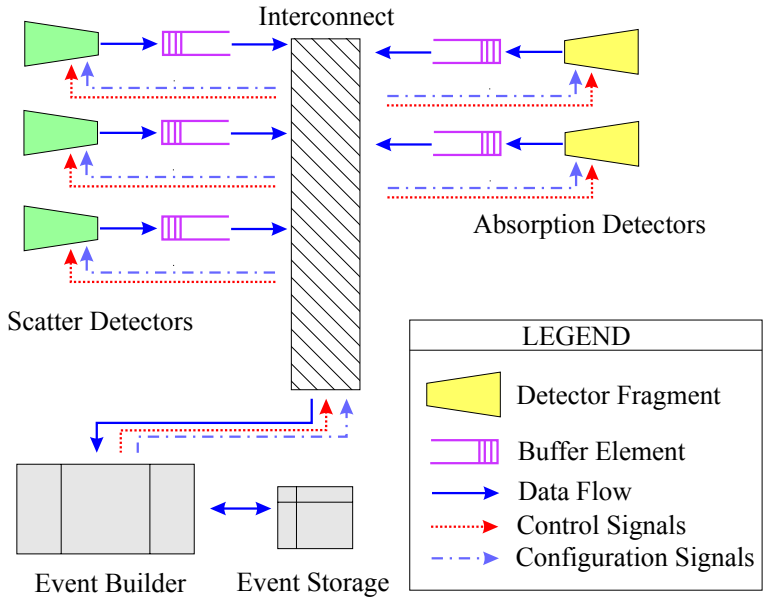

Fig. 4.1: Conceptual design of the data acquisition system

Proposing a high level design requires a possible scenario for the detection and record of Compton events. Such an event building scenario is presented as below:

1. A real Compton event produces at least two event fragments in scatter and absorption detectors.
2. If the energies of these event fragments are high enough (depending on the energy thresholds defined during data taking), these fragments are processed with channel processors (CP) independent of each other. CP's are responsible for digitizing the incoming analog signal from detectors, extracting desired features from the recorded event fragment, adding timing information to the extracted features, signaling the event builder unit about the presence of the event fragment, and storing data for further processing.

3. The event builder unit continuously listens channel processors for possible event fragments recorded by them. If there are event fragments in channel processors, they will be transferred to the event builder. Each fragment is checked for the Compton requirement. As there should be at least two fragments from different detector subsystems belonging to a single Compton event, the event fragment is either rejected and discarded or accepted and paired with its counterpart to form a fully reconstructed Compton event.

4. The collection of event fragments which belong to a single event is called an *event reconstruction*. The reconstructed events are passed afterwards to the image reconstruction computer for final processing and filtering of the acquired data. An event is assumed to have several fields that describe the information it encapsulates. These are time, channel number, measured digitized value(s) for the event and its coincident data pair from the other detector.

5. Images are reconstructed using the final filtered data.

Other important aspects of the Compton camera DAQ system (CCDAQ) can be summarized as follows:

Data quality: This part of the design depends on the analog front-end and the analog to digital conversion process. It defines the resolution sampling speed and puts an upper limit to the event rate to be processed.

Digital data flow: The digital data flow part is concentrated on how efficiently the event fragments can be transferred and processed within the system.

Also any decent DAQ system should provide the following functionality in order to be characterized properly:

Control: Initiation of the system, master start, stop and pause signals, transfer and channel selection signals can be included in this category.

Configuration: Configuration data including depth of buffers, thresholds, channel identifications, requested signal features for the current run, etc. can be included in this category.

Monitoring: Collection of on-line statistics about the proper functionality of the system is important when the runs continue over days.

Debugging: It is invaluable to have a debugging information that shows what happened under which conditions, especially in the development phase of the system .

In the following sections, the development of the real system, based on these concepts, will be shown.

4.2 System Design Requirements

There are two types of considerations which needs to be taken into account for the system design. First the problem has to be defined analytically and the sensitivity required for the measurements has to be calculated. These theoretical calculations may tell nothing about the implementation. Then there are technological limitations due to the availability of the detectors. It is essential to make a good compromise between measurement goals and technological limitations. Theoretical requirements and technological limitations due to the detectors solely are presented in [ÇN04a]. Here, requirements and design parameters with the whole CCDAQ chain will be studied through the engineering point of view.

Analog signals are generated at the detectors when an event occurs. These signals are continuous both in time and amplitude. In order to process them in computers, they have to be quantized. Quantization in time is called sampling, and the quantization of the amplitude is called digitization. The design parameters that are required for processing analog data coming from detectors can be specified as follows:

- Sampling Rate: A maximum sampling rate should be defined that will be used to digitize incoming detector signals. Sampling rate depends on the shape of the signals.
- Resolution: Minimum number of bits required for the digitization of the signals should be defined depending on the dynamic range of the detector signals.

Theoretical aspects of the sampling rate and the resolution are studied in Appendix B.

Finding a limit for the sampling rate requires the use of Nyquist-Shannon sampling theorem [Opp89] which defines a fundamental connection between a continuous signal and its sampled counterpart.

> When an analog signal $f(t)$ is sampled at a fixed frequency of f_s, it can be reconstructed exactly from the sampled signal $f_s(t)$, if maximum frequency content of the $f(t)$ is lower than $\frac{f_s}{2}$

In the following section measurements are presented, which are performed in order to determine the required parameters.

4.2.1 Signals of the Scatter Detector

Signal formation and the analog front-end of the silicon drift detector has been studied in detail in the previous chapter. Here the focus is made on the extraction of the essential parameters such as maximum sampling frequency and number of bits needed for the required energy resolution from the analog part. SPICE simulations of the front-end reveals that the maximum sampling frequency is defined by the bandwidth of the shapers. From the simulated signal shown in Fig. 4.2 and the frequency response of the shaper shown in Fig. 4.3, the analog bandwidth of the system is determined to be around 7 MHz. This leads to a sampling rate of 15 million samples per second. In order to be able to use the same hardware for other measurements where faster shaping is required, the sampling rate was extended at least four times and was set to 66 Mhz.

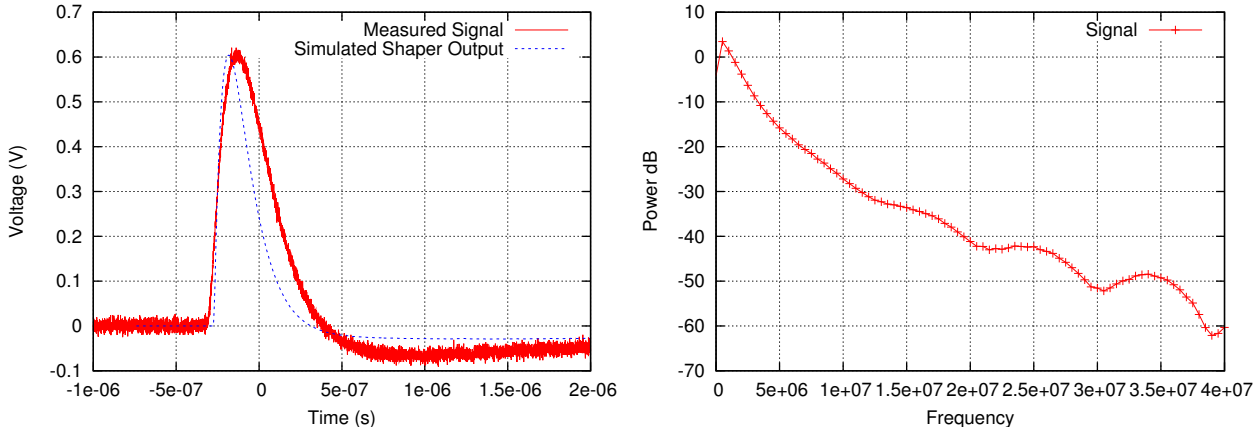

(a) (b)

Fig. 4.2: Simulated transient response of the shaper

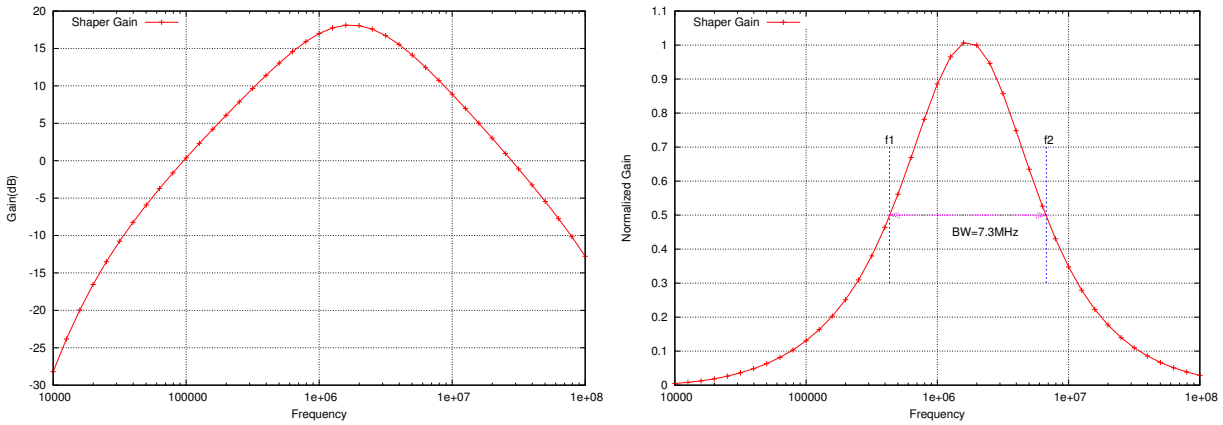

Fig. 4.3: PSPICE simulation of the shaper frequency response

Spectroscopic measurements from the analog front-end showed that the energy resolution of the silicon drift detector (SDD) is at best around 200 eV, and the energy range we would like to measure is in the range of 1 to 400 keV. As the measured energy is proportional to the amplitude of the signal pulse, the Signal to Noise Ratio (SNR) for the SDD system can be defined as $20\log(\frac{400k}{200}) = 66.02$ db. Substituting this value in the equation B.14 gives:

$$k = \frac{66.02 - 1.76}{6.02} = 10.67\ bits \tag{4.1}$$

Commercially available analog to digital converters are either 10 bits or 12 bits. So 12 bit converters have been chosen for the design.

4.2.2 Signals of the Absorption Detector

The Anger camera used as an absorption detector is a refurbished commercial product which has its analog readout electronics embedded on the camera head. Therefore, it was not possible to perform circuit simulations for this detector. Instead, some measurements have been performed

for the characterization of the analog signals. It has been found that the energy resolution for the Anger camera was approximately 10% at 662 keV. Its position resolution is at best 3 mm for a detector diameter of 400 mm. These figures require a resolution of 6 to 7 bits. The estimated shaping times from the signals are around 250 ns which is a little bit slower than silicon detector signals. This study finalizes the requirement specifications for the design of the data acquisition

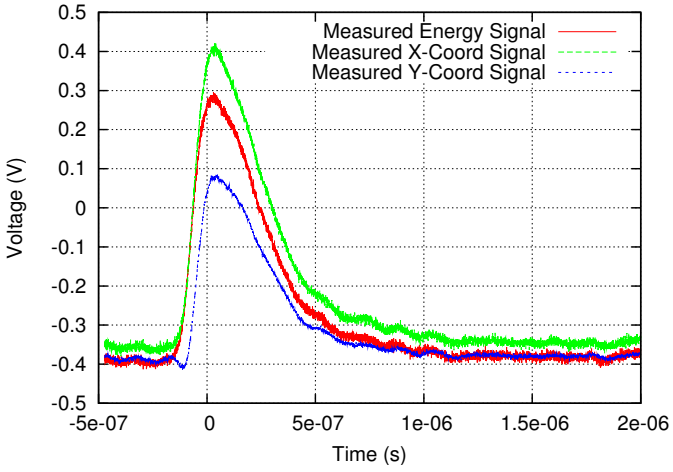

Fig. 4.4: Measured response of the Anger camera

system.

4.3 Implementation of the Data Acquisition System

The implementation of the Compton camera DAQ follows the high level design. It consists of a data/power backplane and a module interface for nine modules where different types of modules can be inserted using standard connectors. The provided modules are as follows.

- Silicon Detector Channel Processor Modules (5 CPM)
- Anger Camera Channel Processor Module (1 CPM)
- Event Builder Module

Channel Processor Modules (CPM) provide high-speed parallel analog-to-digital conversion and on-line data pre-processing. Using the backplane, the event builder module processes event fragments stored in CPM buffers and builds the data structure for the events. It also provides the necessary data connection to the data acquisition computer. This modularity and the use of Field Programmable Gate Arrays (FPGAs) instead of hardwired logic make the whole DAQ system highly flexible and adaptable to modified experimental setups. The infra-structure designed for the Compton camera system has also been used for an x-ray imager by changing the programmed logic of the FPGAs [Ort04]. Before going into the details of the implementation, it is useful to review some basic concepts of the FPGA technology.

4.3.1 Field Programmable Gate Arrays

Field Programmable Gate Array (FPGAs) is an integrated circuit that contains many logic blocks, input/output pins and an interconnection fabric that can be programmed by the end user. User design specifies the functionality of the logic blocks and the way they should be connected. User design may be programmed permanently, semi-permanently or may be downloaded by means of other non-volatile memories on each power-up sequence depending on the implementation technology. There are four major programmable elements on the FPGAs which are demonstrated in Fig 4.5:

1. Common Logic Blocks (CLB): These blocks contain programmable lookup tables, a few flip-flops and multiplexers. They are not very complex. Some companies provide support for binary addition and multiplication of up to 2 bits in their common blocks.

2. Programmable Interconnection fabric: These resources provide connection between one or more CLBs. Clock distribution is also a part of the interconnection fabric.

3. Input/Output Blocks: They provide connection to the world outside of the FPGA. They are capable of converting many I/O standards including differential I/O like LVDS or PECL to the internal fabric.

4. Memory Blocks: On modern FPGAs there are up to few megabits of programmable random access memory blocks that can be used for storing user data. They can be combined to act like a single global memory or can be accessed independently.

The latest FPGAs have even processors embedded to their interconnection fabric that opens new frontiers for applications in signal processing. The main benefits of using FPGAs can be summarized as follows:

- Performances nearly reach to custom CMOS VLSI chips while avoiding the initial cost of fabricating the chip, testing and validating the designs.

- Invaluable during the prototyping stage as they can be re-programmed easily.

- Flexibility and re-programmability make revisions of the products easier, and future requirements may be implemented without changing the hardware which leads to production cost cuts.

- Programming tools and languages are standardized such that it is possible to create a full custom VLSI chip with the same source code that has been tested with the FPGA. Custom VLSI chip may provide cost benefits for production over several thousand units.

- Theoretically, FPGAs combine the speed of dedicated, application-optimized hardware with the ability to flexibly change the chip resource allocation, so the same system can run for many applications, optimized for each one.

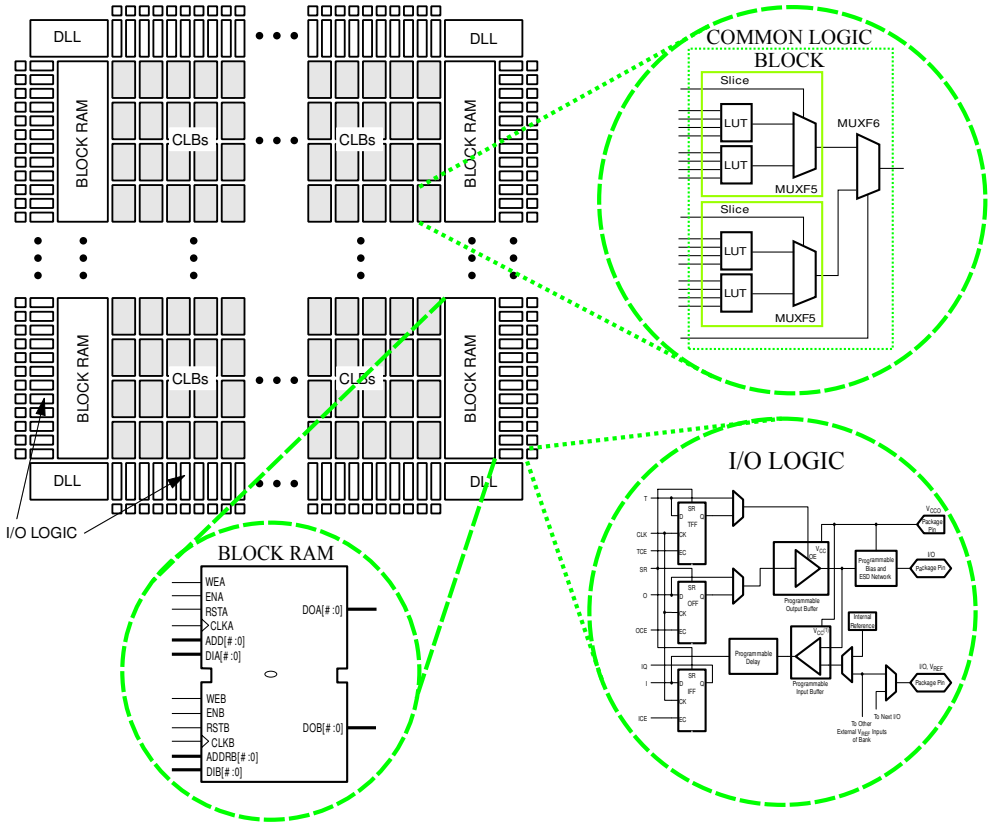

Fig. 4.5: Structure of a Field Programmable Gate Array

Depending on the technology, programming of the CLBs, I/Os and interconnection fabric changes drastically. There are several technologies used to produce FPGAs:

- SRAM Technology: In the Static RAM, FPGA programmable connections are made using pass-transistors, transmission gates, or multiplexers that are controlled by SRAM cells. This technology allows fast in-circuit reconfiguration. The major disadvantage is the size of the chip required by the RAM technology and that the chip configuration needs to be loaded to the chip from some external source (usually external non-volatile memory chip). The FPGA can either actively read its configuration data out of an external serial or byte-parallel PROM (master mode), or the configuration data can be written into the FPGA (slave and peripheral mode). The FPGA can be programmed an unlimited number of times.

- Anti-Fuse Technology: An anti-fuse resides in a high-impedance state and can be programmed into a low impedance or "fused" state. This technology can be used to make program-once devices that are less expensive than those that are produced by the RAM technology.

- EPROM Technology: This is the same technology used in the EPROM memories. The programming is stored without an external storage of configuration. EPROM based programmable chips can not be re-programmed in-circuit and need to be cleared with a UV

erasing.

- EEPROM Technology: This is the same technology used in the EEPROM memories. The programming is stored without an external storage of configuration. EEPROM based programmable chips can be electrically erased and re-programmed in-circuit.

Programming the logic and interconnection of FPGAs are done with Hardware Description Languages (HDL). The HDL code is processed in several stages. First the code is synthesized into simple logic and interconnections via an HDL synthesizer, then it is converted into an appropriate bit stream for the target device. There are several HDLs used in the industry like ABEL, Verilog, VHDL, AHDL but current trend moves toward two standard ones: Verilog and VHDL.

VHDL (Very high speed integrated circuit Hardware Description Language) became IEEE standard 1076 in 1987. It was updated in 1993 and today is known as "IEEE standard 1076 1993". The Verilog hardware description language has been used far longer than VHDL and has been extensively used since it was launched by Gateway in 1983. Cadence bought Gateway in 1989 and opened Verilog to the public domain in 1990. It became IEEE standard 1364 in December 1995.

As it is possible to implement most of the hardware structure both in Verilog and VHDL, the choice of the HDL depends on various factors like; the availability of the software tools and personal choices. VHDL provides a better abstraction at the system level and Verilog has a better support for low level constructs.

There are many different FPGAs with different architectures/processes. The standard digital design flow for FPGA programming is as follows:

- Design Entry: In the digital design stage, the digital design is created with a schematic digital design editor or with an HDL.

- Design Implementation: In the design implementation stage, the netlist produced by the design entry program is converted into the bit stream file which configures the FPGA. The first step maps the design onto the FPGA resources. The second step places or assigns logic blocks created in the mapping process in specific locations in the FPGA. The third step routes the interconnect paths between the logic blocks. The output is a Logic Cell Array (LCA) file for the particular FPGA. This LCA file is then converted into a bit stream file for configuring the FPGA.

- Design Verification: The design verification step tests the designed logic and timing using input stimuli. Various CAE software packages provide verification/simulation tools. In-circuit verification is another way to test the design.

- FPGA Configuration: Configuration is a process in which the circuit design (bit stream file) is downloaded into the FPGA. The FPGA is configured from an application program through this method.

For the Compton DAQ the following decisions have been made:

- VHDL has been chosen as an HDL for the logic designs of this work due to the better abstraction it provides at the system level. The software package that has been used is FPGA Advantage 6.2 from Mentor Graphics. This package provides both VHDL and Verilog. It also includes Modelsim Simulator for design verification which is an invaluable tool greatly simplifying the initial design stage.

- Spartan-IIE FPGAs from XILINX [Xil] have been chosen for the Compton Camera DAQ due to the personal experience and availability of the devices.

- C++ programming and Qt graphics library are used on a Linux computer for creating the DAQ software on the PC site.

4.3.2 Data Interconnection

The data interconnection is implemented as a backplane which distributes both data signals and power to the modules. All the modules share a single physical interface which simplifies design efforts for different module types. The power distribution is made such that analog and digital power supplies are fully separated. The backplane carries 44 digital shared lines, 3 dedicated lines to the module on the left, 3 dedicated lines to the module on the right, 2 dedicated clock distribution lines that allow differential clocking and a global serial JTAG interface that enables to debug and configure individual FPGAs during the development stage. A global clock source, with a frequency of 66 MHz (15.15 ns period) and a rise time of 1 ns, has

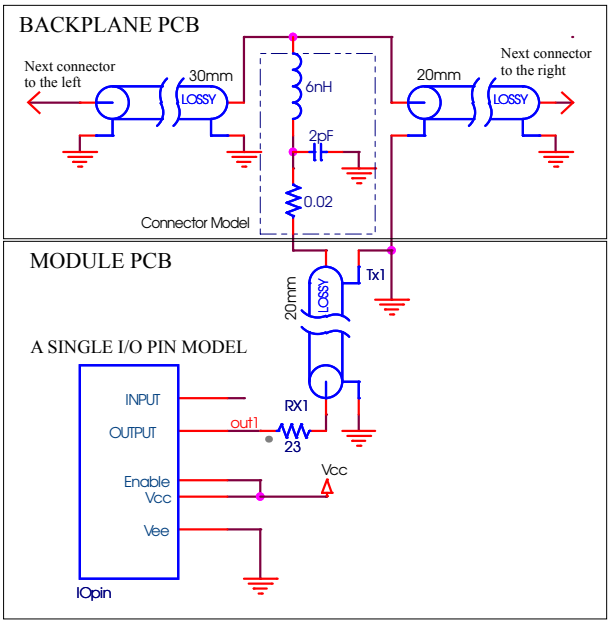

Fig. 4.6: A simulation detail of a single digital I/O pin of the Xilinx Spartan-IIE FPGA. An average signal trace length from the FPGA to the backplane connector is about 20 mm. The distance between the backplane connectors is around 20 mm and termination resistors lie 30 mm away from the leftmost and rightmost connectors. Xilinx provides the IBIS model for the I/O pin. The model is translated into a PSPICE model in order to perform circuit simulations

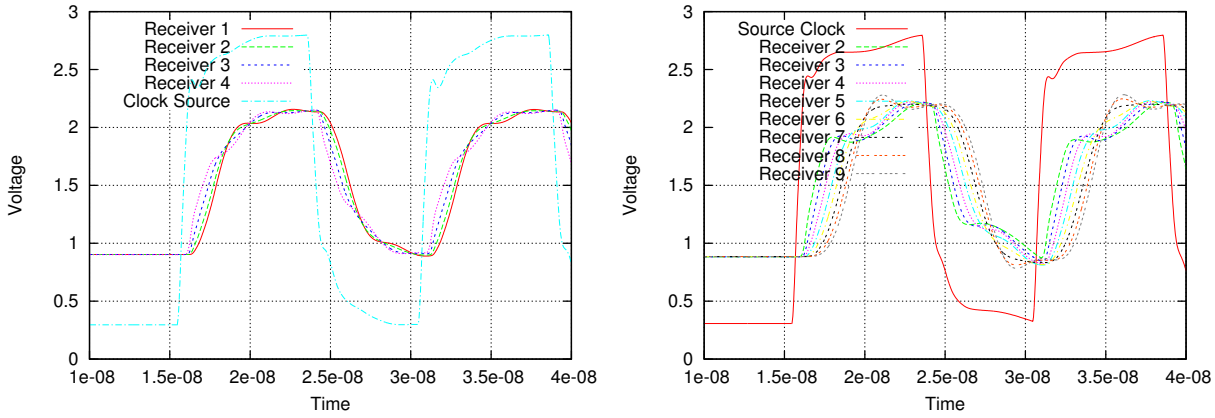

Fig. 4.7: Simulated clock distribution over backplane

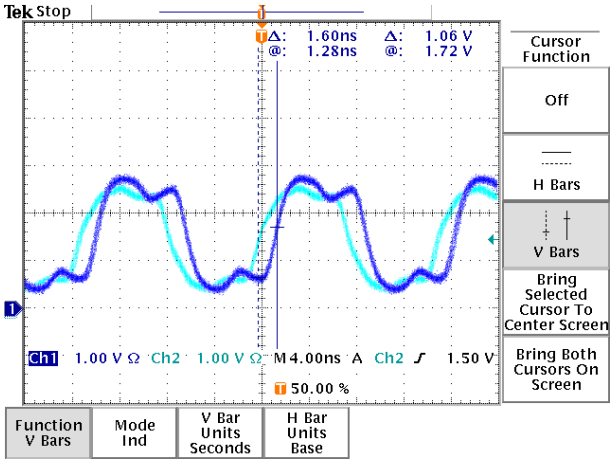

Fig. 4.8: Measured clock signal over the backplane

been used for the simulations. The physical dimensions of the backplane show that the signal and clock traces are around 20 cm long. Any circuit with signal traces longer than $\frac{1}{6}$ of the $\frac{\text{Rise Time}}{\text{Propagation Delay}}$ (length of the rising edge) becomes a *distributed* circuit and these traces act like transmission lines. Initial calculations and design requirements for the backplane showed that the system is actually a distributed system. Any digital signal sent over transmission lines may create ringing, and a time delay which leads to synchronization problems between sender and receiver systems. In order to overcome this problem, the transmission lines has been terminated with their characteristic impedance. This also means that standard TTL signal levels cannot be used for fast data transfers between distant modules. Fortunately, the Xilinx SpantanIIe FPGA provides a set of I/O standards for terminated digital signaling. SSTL3 standard has been selected since it is also used for high speed data transfers between memory modules and processors.

PSPICE simulation of the I/O ports, PCB traces, connector capacitances and the position of the termination resistances has been performed before the final layout design of the PCBs (Fig. 4.6). The results of the simulation for various clock distribution schemas can be seen in

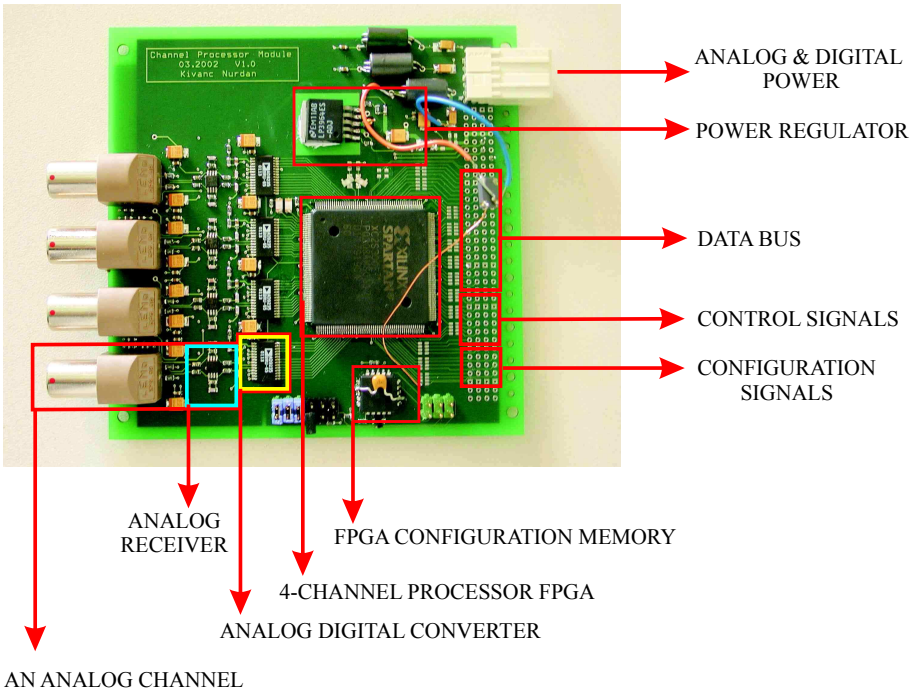

Fig. 4.9: Channel processor card

Fig. 4.7. They are in agreement with the real measurements shown in Fig. 4.8. It has been concluded that the master card should be positioned at the center of the backplane for optimum clock and data distribution.

Other details like the name of the signals carried on the backplane, circuit schematics are presented in Appendix D.

4.3.3 Channel Processor Module

The first module designed is the Channel Processor Module(CPM) which is shown in Fig. 4.9. The CPM is responsible for the digitization of analog input signals and pre-processing. The desired features for CCDAQ are the peak finding and the integration. The extracted features are time-stamped and buffered for further processing. The control logic of the FPGA is implemented slightly differently for the two types of detectors. Flexible and reprogrammable FPGAs enable the application of different control tasks without changing the hardware.

4.3.3.1 Hardware

The CPM hardware consists of 4 12-bit analog/digital converters (AD9235) from Analog Devices [AD] running with a system clock of 66 MHz coupled with differential anti-alias filtered line receivers, a XILINX Spartan-IIE FPGA which is responsible for collecting the data and communicating with the backplane, the FGPA configuration ROM and the voltage regulator. Special care is taken to avoid crosstalk between analog channels and coupling from the digital bus logic. The system runs on three separate power supplies +3.3 V and -3.3 V analog, and

+3.3 V digital. FPGA's internal logic requires an additional +1.8 V which is generated from the digital +3.3 V supply.

The layout of the CPM Printed Circuit Board (PCB) is presented in Fig. 4.9. As there are both analog and digital signals on the board, considerable care has been taken in routing analog and digital signal paths. The analog and digital grounds are totally separated which further reduces the possibility of digital noise appearing on the analog inputs.

On power-up the FPGA reads the FPGA-configuration from 2 Mbit Atmel [ATM] EEPROM. Once the configuration is loaded, the clock signal provided through the backplane is forwarded to ADCs and using the feedback line, the ADC clock and the FPGA are synchronized with the help of the Digital Delay Loop (DDL) feature of the FPGA. This enables reliable data transfer between ADCs and the FPGA.

4.3.3.2 Programmed Logic for the Scatter Detector

The processing model for each channel is combined into a generic channel processor which is then cloned for each channel of the silicon detector. This approach has minimized the design burden of the whole DAQ system. The architecture of the data flow implemented for the scatter detector channel is presented in Fig. 4.10. The data flow starts with a programmable digital delay where data can be delayed up to 256 clock cycles (approximately 4 μsec duration). Electronic delays of different channels can be compensated and even reordering of the events in time, relative to their appearance, can be arranged with the help of this digital delay. Delayed data are then fed into a trigger unit and a second small delay unit, enabling the capture of up to 32 samples ($\frac{1}{2}$ μsec) before the trigger occurs. The trigger unit is programmable with a threshold word and has selectable modes of rising edge, falling edge, and level triggering modes. The triggering decision is transferred to a Local Channel Controller (LCC). The LCC then starts the event window controller unit and according to its configuration, enables operators to be applied to

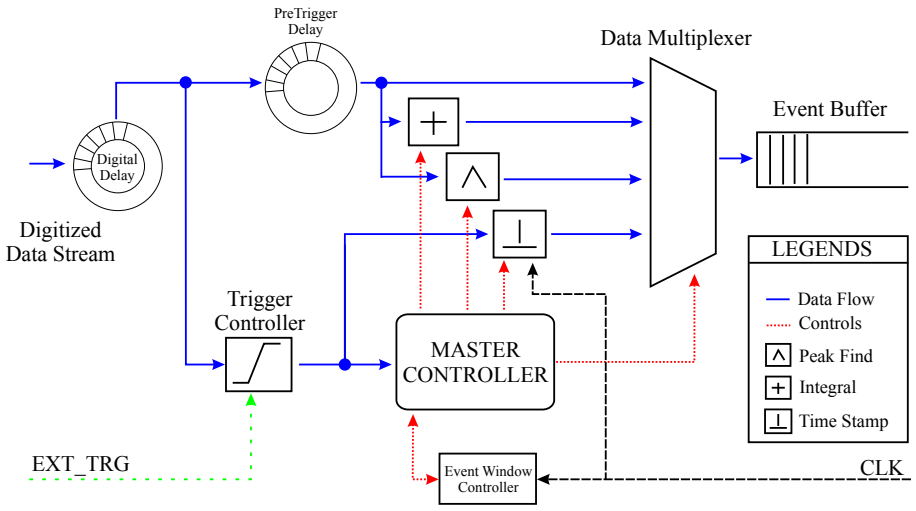

Fig. 4.10: The architecture of a single CPM channel

the incoming data within the programmed event window. The following four operators are implemented:

1. Peak Finding : According to the configuration, the maximum or minimum of the samples within the event window are searched. At the end of the event window, the base-line extracted from the pre-trigger data is subtracted from this extremum and stored until the next event starts.

2. Integral : All the samples in the event window are summed. The result is preserved until the next event is triggered.

3. Raw Data : The sampled data is transferred directly to the output FIFO. This is quite useful for visualizing and debugging the digitized signals.

4. Time Stamp : The time stamp generator is a 36 bit up-counter which is initialized when the DAQ system is started. It has a clock accuracy of 15.15 ns. When a trigger occurs, the value of the time stamp generator is copied to the time stamp register and stored until the next event comes.

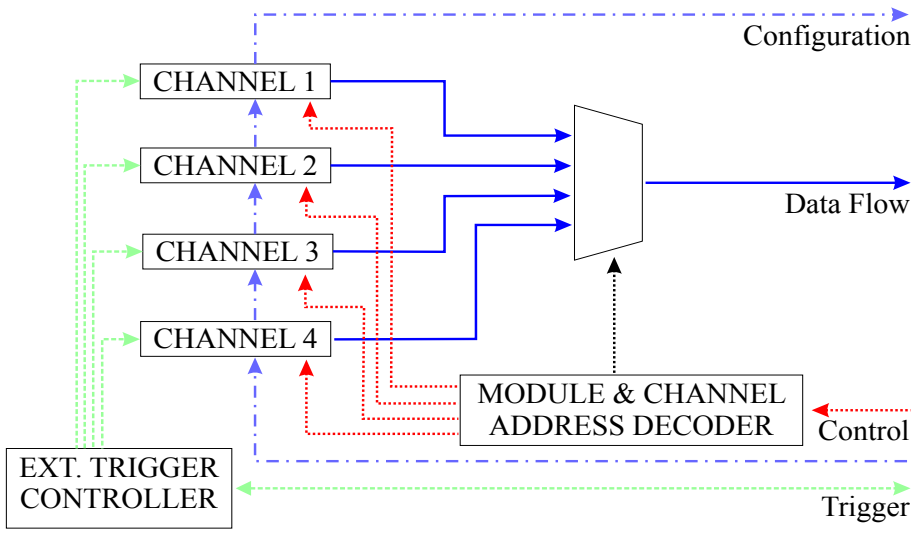

Fig. 4.11: The slave bus controller and the external trigger logic

These operators may be enabled inclusively. The event window controller signals the LCC when the end of the event window is reached. The LCC then stops all ongoing operations, collects results and transfers them to the de-randomization First-In-First-Out (FIFO) buffer. Each channel has a dedicated FIFO of 256 words in the current implementation. It is also possible to extend this to 1024 by changing the VHDL code, if needed.

The transfer of data from the de-randomization buffers to the EBM is achieved by the slave bus controller (SBC) logic shown in Fig. 4.11, which doesn't depend on the LCC. The SBC implements a simple control mechanism on how full the FIFOs are and signals the bus master if

a pre-programmed level is reached depending on the event size. There may be only one master but many slaves on the bus. As there are four physical channels on a CPM card, a single SBC is implemented per CPM and it serializes the data to be sent over a bus to the EBM which is coordinated by a Bus Master (BM) implemented in the EBM.

4.3.3.3 Programmed Logic for the Absorption Detector

The absorption detector front-end electronics produces already shaped signals together with a trigger. The signals are X coordinate, Y coordinate, energy and corrected energy which is also used for triggering. The same channel structure used for the silicon detector channels has also been used for the Anger camera readout with the following changes:

- The first three channels on the CPM are assigned to X,Y and E signals. Triggering mode for these channels is set to external triggering.
- The fourth channel is assigned to the corrected energy signal and the internal trigger decision of this channel is fed to other channels through the external trigger controller.
- Accessing FIFOs of this module should be in X coordinate, Y coordinate, energy (E_{eng}) and corrected energy (E_{cor}) sequence. Reading out of sequence leads data synchronization loss in the FIFOs.

The input stage of this module is also modified for the single ended reception of the Anger camera signals.

4.3.4 Event Builder Module

The event builder module is the heart and brain of the whole system. It not only provides clock and configuration signals to the rest of the modules but also collects the event fragments and performs the event building. The data flow diagram and the high level design of the EBM with the integrated BM logic is presented in Fig. 4.12. The implementation consists of following sub-units:

- Bus master controller: It is responsible for sending the control and configuration signals to CPMs and monitor their status continuously.
- Data transfer Controller : This unit is responsible for making burst transfers over the data bus and stores event fragment data to pointed buffers.
- Coincidence Unit: This unit is a dedicated hardware coincidence unit that compares two given time stamps and produces a boolean result on the condition that they are in a given time window relative to each other.
- Memory Access Controller (MAC): On-board 2 MB SRAM can only be accessed exclusively from various units. MAC should provide a way for sharing the access to the SRAM.

- Communications Controller: It should provide a protocol for data transfers to the data acquisition computer.

- Programmable System Controller (PSC): It organizes all interactions between the units, event building and data organization.

The event building process using these units can be implemented as follows: After event fragments are collected in CPMs, SBCs create proper request signals for the BM. All CPMs have dedicated request lines to the BM. The BM controls two queues where the received data are pushed in. The data received from the absorption detector are pushed into one queue (ABS-REG) and all the others to the other queue (SCAT-REG). Due to the nature of the Compton events, the ABS-REG queue length is set to 1. If new data arrive to the ABS-REG, the SCAT-REG queue is cleared and made ready for the next possible Compton event. The coincidence logic checks time stamps from both queues, and if the time stamps fall within a defined relative time window they are accepted as coincidence candidates and the Programmable System Controller (PSC) is informed about this decision. The PSC is implemented as a small stack-processor that is fully programmable. It continuously transfers time stamps to the coincidence unit and checks the coincidence decision. If a true coincidence decision occurs, it accepts this candidate as a Compton event and transfers all data from the queues to the SRAM with a known data structure. The PSC is also responsible for establishing a PC connection and a proper protocol to transfer data from the SRAM to the PC.

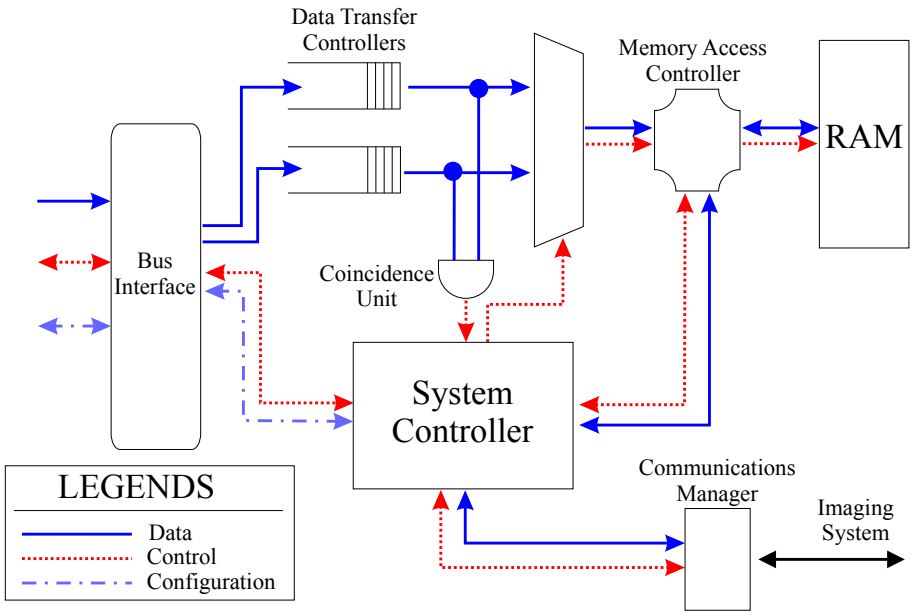

Fig. 4.12: The bus master and the high level design of the event builder module

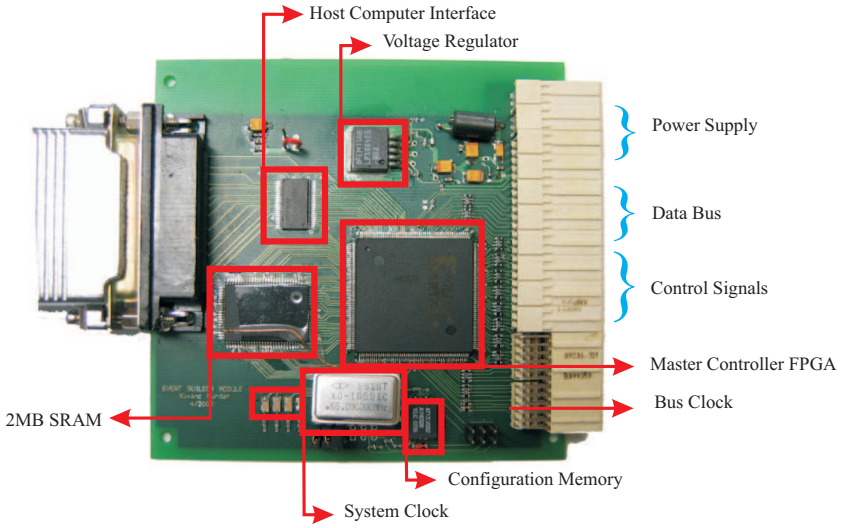

Fig. 4.13: Event builder module

4.3.4.1 Hardware

The EBM hardware shown in Fig. 4.13 is implemented with a 1 M × 18 bit NtRAM from Samsung [Sam] which is actually a synchronous SRAM, a XILINX Spartan-IIE and LVX161284 physical level parallel port interface from National Semiconductors [Nat]. As this module is built completely using a digital technique, design constraints are easily fulfilled. The system clock is generated with a crystal oscillator and is fed directly to the FPGA. The FPGA then regenerates the clock signal for the backplane in SSTL3 (Stub-Series Terminated Logic) and for the SRAM in LVTTL (Low-Voltage Transistor-to-Transistor Logic).

4.3.4.2 Implemented FPGA logic

Initially a fully static, state machine oriented system controller has been designed for the EBM. But controlling and debugging such a system turned out to be more difficult than initially thought. Then a full-fledged 16-bit stack processor core with a separate program, data and i/o memory spaces is implemented which provides enormous flexibly with some compromise in possible maximum throughput. The detailed description of the processor core is presented in Appendix C.

The designed processor core has the following properties:

- It is fast enough to perform all of the required tasks like per event coincidence processing, buffer allocation and transfer, within one or two microseconds.
- It was simple enough to be implemented and tested in VHDL within 2-3 months time. The designed core covers only 15 percent of the target FPGA platform.
- The implemented core has a high code denstiy (minimum code length) for most of the

tasks to be performed. All the system code fits with in 512 words and the total dedicated code memory is 2 kwords.

- The implemented peripheral access protocol is simple and additional peripheral cores can be easily integrated to the processor core.

The processor has a single instruction cycle for all operations including branch and subroutine calls. The separation of the program memory and the data memory leads to a simple and straight forward instruction fetching and execution unit. All the programs that are written for the processor core fit into 512 words including the bootstrap kernel code.

The implemented core has the following peripherals that are mapped to the I/O memory space of the processor core:

- Communications Controller: An 8 bit Extended Capability Port (ECP) interface has been implemented for a simple data communication between the data acquisition computer and the event builder. The unit performs all necessary signaling with the DAQ-computer and when the transmission is finished, it signals the processor-core if there is new data or the data has been sent successfully.

- Coincidence Unit: A 48 bit coincidence unit with high and low thresholds is implemented. Given two 48 bit time stamps and two 16 bit signed high-low thresholds, the coincidence is performed first by the extension of the 48 bit values to 49 bit signed values and the subtraction of them is followed by two comparisons, all of which are performed in a single cycle. The result is presented as inside the range, above the range or below the range.

- Bus controller: This performs the duties of the bus master. It is directly coupled to the configuration and signal monitoring on the bus.

- Data Transfer Controller: It performs synchronous data burst transfers over the bus to the data memory without the intervention of the processor core. It has a programmable base address, length of the burst and start/stop controls.

- Memory Access Controller: This is a priority arbiter between the processor and the data transfer controller which regulates access to the data memory space. When there is a burst transfer to the data memory, it prevents access to the processor core.

- Data Memory: This is a 20 bit data address space. The processor core has only a 16 bit address register. Upper 4 bits are provided by a memory page register.

Implementation details of the event builder are shown in Fig. 4.14. The global design is divided into 3 address spaces, all of which can be addressed by the processor core. The data address space is shared between the processor core and the data transfer controller.

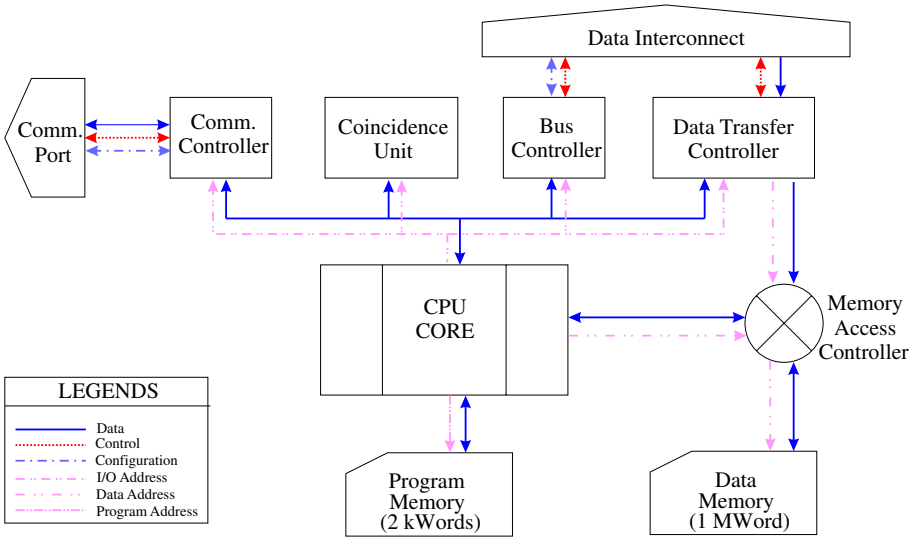

Fig. 4.14: Implementation details for the event builder module

4.4 Readout Software

The software written for the DAQ system can be divided into two parts: Programs written for the DAQ-processor and the programs written for the DAQ-supervisor-computer.

The software written for the DAQ-processor is purely in machine language and provides an initial boot-strap and a micro-kernel for the DAQ-processor. The micro-kernel code is directly embedded into the VHDL code of the processor. The kernel provides a very primitive boot-shell over parallel port interface to the user. The commmands available for the user are as follows:

- read cpu memory: sends all the processor memory (∼4 kB) over parallel port, except kernel area.
- write cpu memory: all processor memory is written with the data sent over the parallel port.
- read ram: any part of the data memory (∼2 MB) can be read.
- write ram: any part of the data memory can be written.
- execute program: execution starts with a call instruction to the first address of the processor memory. The program that is executed should return success or failure message when it is finished. There is no way to stop execution once it is started unless the program terminates by itself. But it is still possible to send a reset signal to the processor with a hardwired instruction embedded into the parallel port interface.

A typical DAQ session is as follows: DAQ supervisor-computer first establishes communication with the processor core. The boot-shell becomes active and ready to receive commands. DAQ supervisor loads the DAQ-executive program to the processor and sends the execution

command. The DAQ-executive program takes control and provides the required DAQ functionalities like the configuration management, starting and stopping the data flow and the data transfer between the DAQ system and the DAQ supervisor-computer.

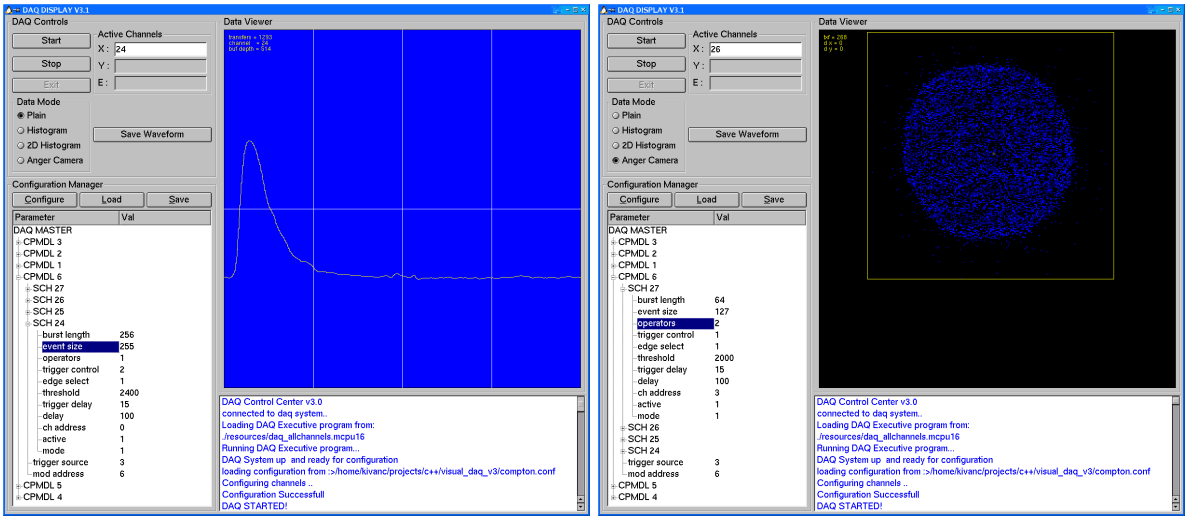

Fig. 4.15: Visual DAQ program in shaper output and 2D histogram visualization modes, respectively

On the DAQ-supervisor-computer, two DAQ readout programs have been created for the data acquisition; namely the DAQ-Visual program and the DAQ-Compton program. The DAQ-Visual program is an interactive program which provides a visual interface for the whole DAQ-system as shown in Fig. 4.15. It is written in C++ and Qt and runs on a linux operating system. The main purpose of this program is to check the configuration parameters, to monitor the detector signals, to inspect the energy histograms visually and to display the Anger camera interactions in 2D. It provides the following functionality interactively:

- load configuration: loads DAQ-configuration from a given file
- modify configuration: acts for the modification of all parameters for each channel
- configure: sends configuration data to the DAQ-processor
- start: starts acquisition
- stop: stops acquisition
- reset: resets the DAQ-processor and reloads the DAQ-executive program
- select visualization mode: provides the selection of different visualization modes such as the shaper output, the energy histogram and the 2D histogram

The DAQ-Compton program, on the other hand, is non-interactive and used for automated measurements. It is called via the command line and uses the provided configuration file. It simply collects the data for a given number of Compton interactions from the DAQ-system,

stores them to a file, and stops the system without any other interaction. It is mainly used for high statistics measurements.

4.5 Measurements

After performing the calibration measurements for scatter and absorption detector subsystems, the remaining measurements are divided into two categories. The measurements which exploit the timing properties of the prototype system, and coincidence measurements for the image reconstruction.

4.6 Timing Measurements

The initial rate measurements with the Compton camera prototype revealed that it is not possible to see the theoretical expectations in the detected rate change due to the fact that the measured rates were very low. In order to show that the system performs ideally in this low rate condition, timing measurements with a ^{57}Co source has been done. The measured results of the event time stamp distribution are presented as follows . Fig. 4.16 shows the interval distribution which has the same characteristics as Fig. 2.19. Fitting the exponential function given below;

$$y = A \cdot e^{-\frac{x}{t_1}}$$

with two parameters to this figure gives $A = 0.001705$ and $t_1 = 588.56$ where $1/A = 586.5$ shows that this is nearly a perfect interval distribution. The calculated rate is 1700 counts per second (cps).

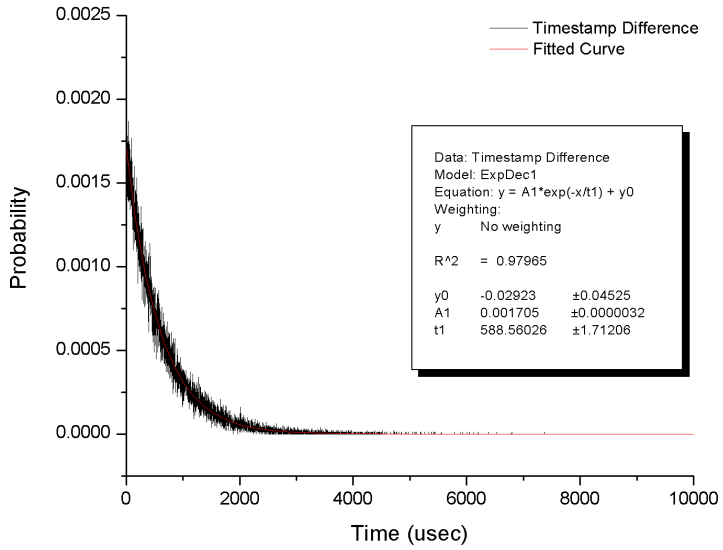

Fig. 4.16: The measured time stamp interval distribution for the Anger camera

The histogram of the number of events for a given interval is also calculated and is presented in Fig. 4.17. The observation window is set to 10 milliseconds (ms). From the previous calculation, the rate was found to be 1700 cps and for a time window of 10 ms 17 events are expected on the average with a Poisson distribution. Fig. 4.17 perfectly shows these expected results.

Coincidence measurements require that both interactions occur in two detector systems nearly at the same time. In addition to these *true coincidences*, each detector system produces events which may not belong to Compton events. Due to the random nature of these events, they may appear at the same time quanta and falsely accepted as coincidences as well. Ideally for coincident events, the event times recorded in both detectors should be almost the same. In reality there are different signal delays due to the electronics and the recorded event times for coincident events may differ. In order to find this relative time delay, *time coincidence curves* can be plotted.

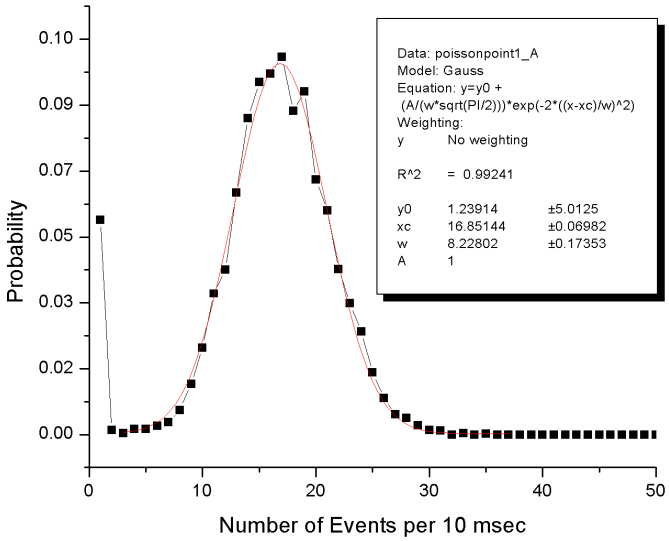

Fig. 4.17: The histogram of the observed number of events for every 10 ms

The rate of false coincidences can be calculated with a simple formula assuming that there is no correlation between coincident events for both detector systems:

$$r_{\text{false}} = 2 \cdot \tau \cdot r_s \cdot r_a$$

where τ is the coincidence window, r_s and r_a are the measured rates from scatter and absorption detectors, respectively. This creates a continuous flat background in the time coincidence curve.

The time coincidence curve presented in Fig. 4.18 is produced from the data acquired with the first version of the data acquisition software, where all the events were collected from scatter and absorption detectors and coincidence events are filtered by the offline analysis software. $4.50{\cdot}10^8$ Anger camera events and 4.35 10^5 SDD events are collected within 128 hours of data

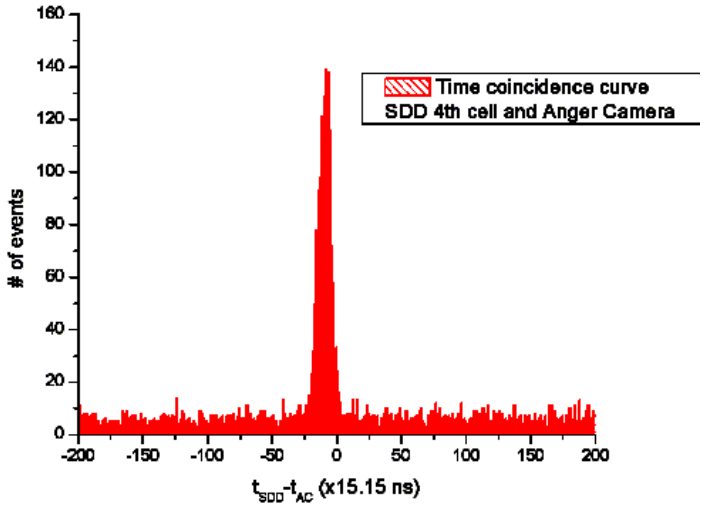

Fig. 4.18: Time coincidence curve for the events occuring in the 4th channel of the SDD and the Anger camera

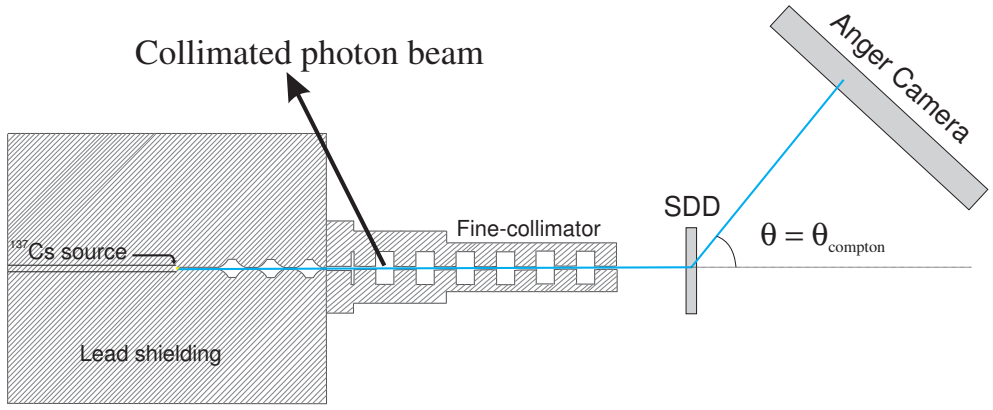

Fig. 4.19: Coincidence setup for high statistics measurements

collection. The time stamp difference is restricted to ± 3 μsec in the analysis. There are 3840 event pairs in the coincidence window of ± 3 μsec and 1653 of them are populated in the region where $t_{SDD} - t_{AC}$ ranges between -300 ns and +75 ns. The FWHM of the coincidence peak is around 300 ns which is mainly due to the drift time of the electrons in the SDD.

4.7 Imaging Measurements

High statistics coincidence measurements have been performed [ÇN04c] for the system configured as shown in Fig. 4.19.

With this orientation of the absorption detector, an angular range of 10°-50° is covered for the scattered photons which favours the collection of high statistics due to a high cross section of the Compton scattering in this forward angular region at the energy of 662 keV. The FPGA on the

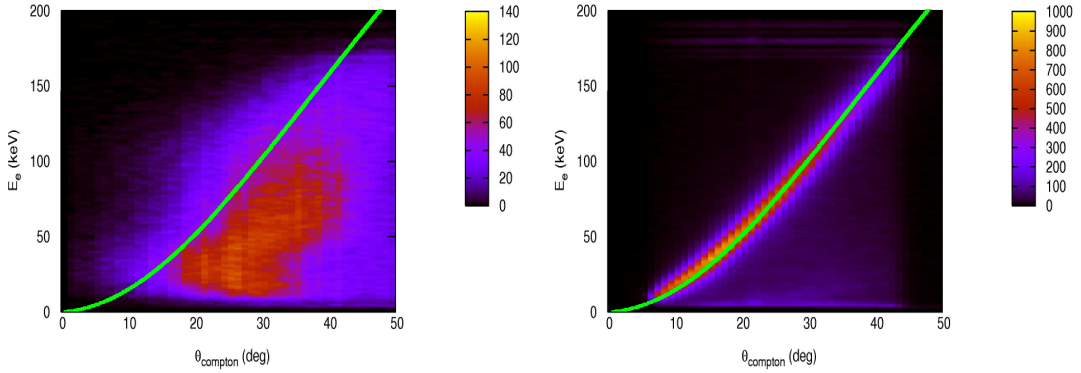

(a) E_e vs θ with θ calculated from $E_{\gamma'}$

(b) E_e vs θ with θ calculated from interaction locations

Fig. 4.20: Measured recoil electron energy as a function of the scattering angle where (a) θ is calculated from the energy of the scattered photon measured in the Anger camera (b) θ is calculated from the measured interaction locations. The smooth curve shows the theoretical calculation

master card is programmed such that the acquisition of the data in a selected time window would be possible. The time window is chosen to be in the range of $-300\ ns < t_{SDD} - t_{AC} < 75\ ns$ where most of the coincidence events are peaked as shown in Fig. 4.18. The coincidence rate was around 0.9 events per second with these settings.

2D histogram plot of the recoil electron energy measured in the SDD as a function of the scattering angle is shown in Fig. 4.20. In Fig. 4.20(a) the scattering angle is measured from the energy of the scattered photon using the equation:

$$\theta = acos\left[\frac{E_{\gamma'}E_{\gamma} - m_e c^2(E_{\gamma} - E_{\gamma'})}{E_{\gamma'}E_{\gamma}}\right] \tag{4.2}$$

On the other hand, in Fig. 4.20(b), the scattering angle is determined from the measured location of interactions in the Anger camera. For this calculation, it is assumed that the incoming photons are directed perpendicular to the SDD plane due to the small angular spread ($\approx 0.3^{\circ}$) provided by the collimator. In this case, the scattering angle can be assumed to be equal to θ as shown in Fig. 4.19. The theoretical expectation curve is also shown in both figures and while the data plotted in Fig. 4.20(b) agrees well with this curve, there is a large deviation from expectation in Fig. 4.20(a). This is mainly due to the fact that the energy resolution of the Anger camera is not good enough for the measurement of the scattered photon energy accurately and there are many partial events where the energy of the scattered photon is not totally absorbed. The cross section of the Compton scattering is quite high for this energy range of the scattered photons and these events result in the partial absorption of the scattered photon energy.

The energy of the scattered photon as a function of the recoil electron energy has also been analyzed with two different methods in Fig. 4.21. In Fig. 4.21(a) the measured energies of the scattered photon and the recoil electron are plotted. The distribution of the scattered photon energy measured in the Anger camera consists of two parts; one of which is around

the theoretical expectation curve and other forming a broad distribution below this curve. The upper part corresponds to the scattered photons undergoing a photoelectric absorption process in the Anger camera where they deposit all their energy. The large broadening with respect to the fine theoretical curve is mainly due to the uncertainty in the energy measurement of the scattered photon in the Anger camera. The lower part of the distribution corresponds to those events which undergo a Compton scattering in the absorption detector. Due to the partial absorption of the scattered photon energy, the energy range of the scattered photon is below the expected value for this part. In Fig. 4.21(b) the recoil electron energy is the measured energy in the SDD, whereas the scattered photon energy is calculated from the scattering angle which is determined using the coordinate information of the interactions. This results in a much narrower distribution which agrees with the theoretical expectation.

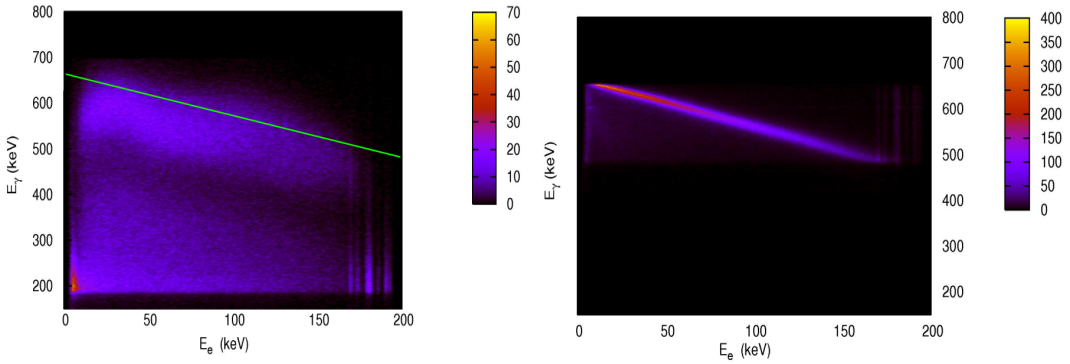

(a) Measured $E_{\gamma'}$ vs E_e

(b) $E_{\gamma'}$ vs E_e where $E_{\gamma'}$ is calculated from θ

Fig. 4.21: Scattered photon energy as a function of the recoil electron energy for two cases: (a) $E_{\gamma'}$ and E_e are the measured energies in the Anger camera and SDD, respectively (b) $E_{\gamma'}$ is calculated from the scattering angle which is determined from the interaction locations. The smooth curve shows the theoretical calculation

Finally, using the coincidence data, the image of the point-like ^{137}Cs source is reconstructed as shown in Fig. 4.22(b). The angular spread is around 1.4° which agrees well with the theoretical expected value of the angular uncertainty (1.3 °) for an inter-detector distance of 120 cm as shown in Fig. 4.22(a).

The image is reconstructed using a new iterative algorithm, Imaginary Time Expectation Maximization (ITEM) that has been proposed by Pauli [Pau02]. It has been further optimized by I. Chiosa [Chi04]. The main difference of this reconstruction algorithm opposed to others, is that not all the dataset is required to perform the reconstruction. With ITEM, it is possible to start the reconstruction with one data set and as more data is available it can simply be added in order to improve the quality of the reconstructed image. In this respect, it is well suited for a realtime acquisition and reconstruction which is a desired property.

ITEM is motivated by the quantum mechanical considerations. It works with a Hamiltonian-like operator acting on the actual image which is identified with a wave function. Due to the

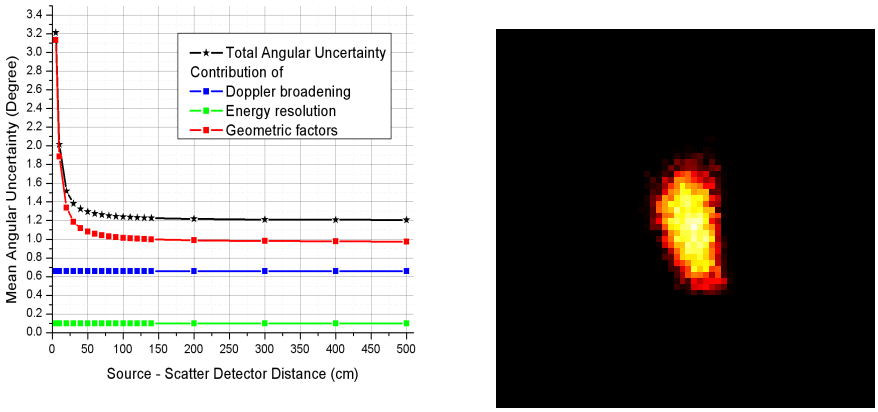

(a) $\Delta\theta$ vs D_2 (b) Recostructed image

Fig. 4.22: (a) The theoretical angular uncertainty as a function of inter-detector distance including individual contributions (b) Reconstructed image where the angular uncertainty is around 1.4° for D_2=120 cm

poor spatial pixel resolution of the silicon detector (that only has 19 cells which are 2mm apart), it was not possible to create a 3D reconstruction and the measurements are restricted to 2D reconstructions.

4.8 Overview of the DAQ System

The burst performance of the system can reach up to $6 \cdot 10^6$ events per second with a 3 cycle protocol delay and 5 cycles of data transfer with a system clock of 66 MHz, depending on the definition of the event data. Each channel has an additional independent deadtime of 2-7 clock cycles, depending on the selected operators. Maximum achievable sustained data rate is $2 \cdot 10^5$ events per channel per second when 32 channels are fully utilized. The Compton coincidence logic manages $5 \cdot 10^5$ Compton events per second and the expected Compton event rate is $1 \cdot 10^4$ Compton events per second for the prototype system. The parallel port PC interface with a raw data transfer rate of 800 kB/sec is capable of carrying two times more information than required for the whole system.

Chapter 5

Monte Carlo Simulations & Discussion

In the theoretical overview (Chapter 2) some analytical calculations for the performance of the radiation recording systems expressed through the DQE, have been presented. As it has been pointed out, the Compton cameras (and other modern imaging systems like PET) are more complex and can not be described in the same way using analytical calculations. Therefore, in this chapter the Monte Carlo method is introduced and the simulation results obtained for the implemented DAQ system is presented. The simulations are extended later in the chapter for the discussion of the related systems.

5.1 Monte Carlo Model of the DAQ System

The Monte Carlo simulation model that has been designed in order to study the complex dead-time relations in the implemented DAQ system, is illustrated in Fig. 5.1. This model consists of parameters which can be divided into two groups as follows;

1. Detector parameters:

   ρ_c The initial activity of the source.

   C_{es} Probability of a Compton interaction in the first detector and an interaction in the second detector.

   E_a Additional interaction efficiency of the second detector. This includes Compton interactions in the second detector which doesn't reach to the first detector and photoelectric interactions

   ρ_1 Random event rate in the scatter detector from other sources.

   ρ_2 Random event rate in the absorption detector from other sources.

   B_s Event buffer depth of the scatter detector.

   B_a Event buffer depth of the absorption detector.

2. Coincidence processor parameters:

r	The width of the coincidence time window.
C_{acc}	The time penalty for the coincidence processor during its access to the detector buffer.
C_{trn}	The time penalty for the coincidence processor during its transfer of data.
C_{coin}	The time penalty for the coincidence processor per coincidence.
C_{rec}	The time penalty for the coincidence processor during the reconstruction of an event

The paralyzable model has been choosen for the detectors due to digital processing and signal analysis. The arrival rates at the two detectors are chosen as follows:

$$\begin{aligned} A_s(t) &= C_{es} * \rho_c + \rho_1 \\ A_a(t) &= (E_a + C_{es}) * \rho_c + \rho_2 \end{aligned}$$

where the subscripts of the arrival rate (A) denote the scatter and the absorption detectors, respectively and $(E_a + C_{es}) \leq 1$. They are used as the real event rates in the Monte Carlo simulations.

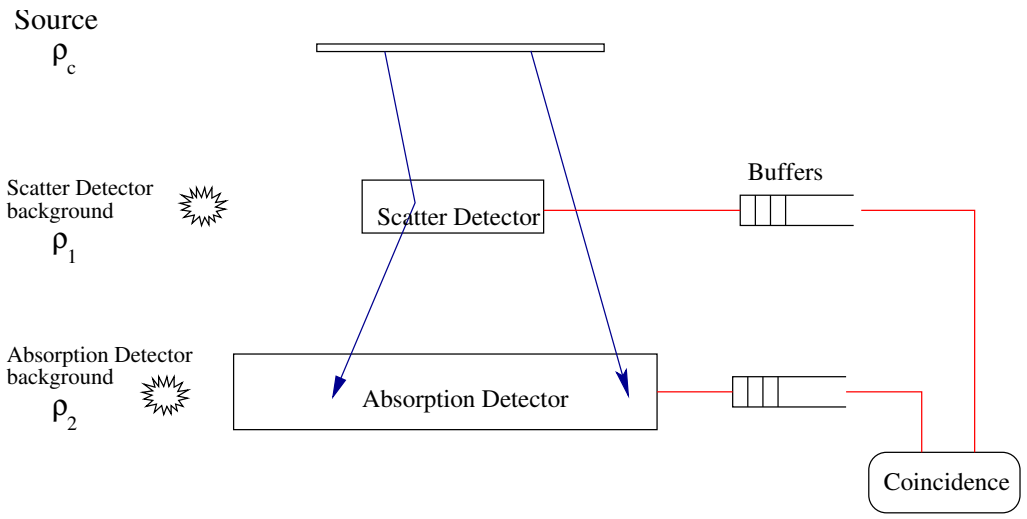

Fig. 5.1: Illustration of the DAQ Monte-Carlo Model

5.2 Monte Carlo Algorithm

The Monte Carlo (MC) algorithm is designed to generate and process event objects. Each event object consists of a unique event ID, an event type, a detector type where it is interacting, a time stamp and an amplitude. The algorithm treats the time like a pointer which is updated from an event to an event. All events are created in a dynamic double link list where the iterations in the forward and backward directions in time are possible.

The whole simulation is divided into three major modules which make modifications for different detector systems and coincidence strategies easier.

The first module is the *generator* that generates coincidence and random events for both scatter and absorption detectors with time stamps and relevant amplitude information. Generated events are inserted to an event list that is ordered according to the time stamps of the events.

The second module is the *detector* where different detector systems are modelled. For each modelled detector subsystem, the globally generated event list is processed and detector specific processes (like drift, detection uncertainity, etc) are implemented by modifying the event's time stamp and/or amplitude information. The survived events are inserted to another linked list and marked as processed by the related detector subsystem. Intelligent detectors with their integrated electronics are also simulated at this stage.

The third module is the *coincidence unit* where the event lists processed by the related detectors are searched for the coincident events. Buffer effects, timing penalties for coincidence processor and coincidence window are implemented in this module. Specifically, buffers are simulated as pointers moving on the event array. Detector deadtimes and processing times spent in the coincidence processor simply increase the current time marker. If the time stamp of the next event is smaller then the current time, it is marked as lost.

Finally the statistical properties of the coincidences are calculated using the resulting coincidence event list.

5.3 Simulation Results

As it has been shown, there are many simulation parameters which may have an influence on event losses. The important aspects that are aimed to study are the influence of buffer depth, and the performance of the soft coincidence system compared to a hardwired system. The actual parameters extracted from the real Compton prototype system are used in the simulator in order to characterize the performance of the overall system and to study the factors mentioned above.

The simulation parameters are set as follows for the following figures: Random event rate is set to zero for the first detector and 1700 counts/s for the second detector, C_{es} is chosen to be 1 (100% efficiency) and $E_a = 0$ such that all the Compton events are captured in both detectors. Although this assumption with the existing detectors is almost impossible to achieve and applies only in case of ideal detectors, it does not affect the generality and simulation of deadtime and DQE. Observation time has been set to 1 second and up to 1 million events are simulated for each point in the graphs. The paralyzable model has been chosen for both detector systems with a deadtime of 1 μs. Buffer access times C_{acc} are set to be 3 μs for each detector with per event transfer rate C_{trn} of 0.2 μs for each consecutive event in the buffer. The coincidence window is chosen to be 0.3 μs which is the maximum drift time of the silicon detector.

The first aspect to be studied is the influence of the buffer depth on the event losses. The comparison of the observed rate versus the real rate is presented in Fig. 5.2. It is evident from the simulations that increasing the buffer depth has a positive influence on the observed rate for a given real rate. This can be explained by the derandomization effect of the buffers. The coincidence processor's deadtime is not constant and decreases per coincidence operation when

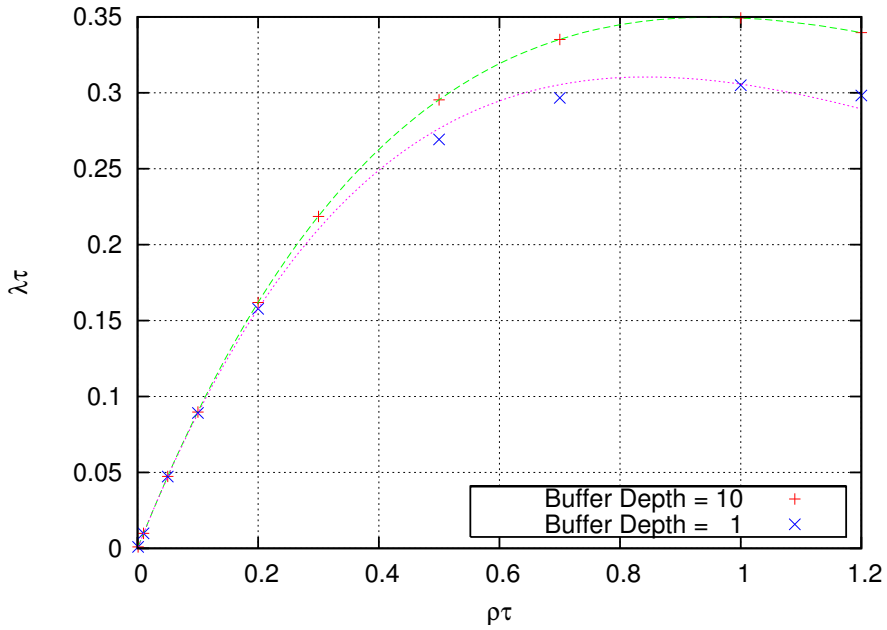

Fig. 5.2: The observed rate versus the real rate for different buffer depths for the implemented coincidence system

the buffers are longer. This is due to different fixed penalties for accessing and transfering data from detector data buffers. The buffers regulate the random nature of the incoming event flux, hence the block transfers of multiple event data speed up processing. Obviously , if the average interval time between events is less then the dynamic system dead time, the buffers saturate and the losses increase immediately.

The second aspect concerns the question how well the soft coincidence system performs compared to a hardwired system. The hardwired system is defined as the system where no deadtime is applied for coincidences.

In Fig. 5.3 the observed rates for hardwired coincidence unit versus the coincidence processor that is implemented in the Compton camera prototype, with an event buffer depth of 10, is presented. It is evident from the figure that both systems perform nearly the same.

In the second chapter a way to compare through the use of DQE principle was presented. The theoretical formula for DQE for the hardware coincidence system has been derived using the Eq. 2.62 and the upper limit of Eq. 2.63 as the variance of the detected rate with the following simplifications.

The simulation parameters were $\rho_1 = 0$, $\rho_2 = 1700$ events/s, $\tau_1 = \tau_2 = 1\mu$s, r= 0.3 μs, t=1 s and ρ is in the range of $10^3 - 10^6$ events/s. The Eq. 2.62 can be simplified to:

$$\lambda = \rho e^{-\rho\tau} \tag{5.1}$$

as ρ_2 has not a significant contribution to the final result even on the extremums. Then the mean becomes $E = \lambda \cdot t$ and the variance is simplified to $V = \lambda t[1 - 2\lambda\tau]$. Let $\kappa = \frac{\tau}{t}$ and

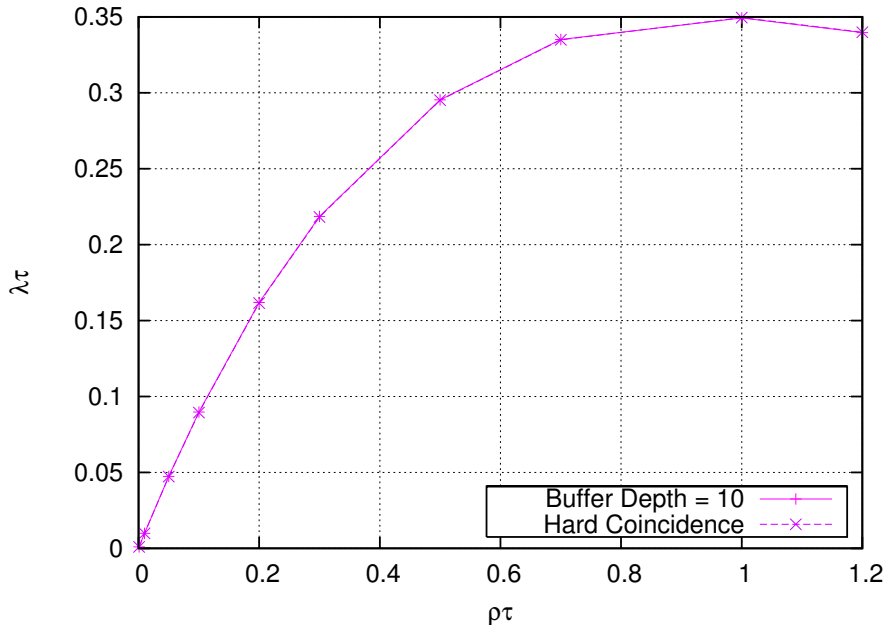

Fig. 5.3: The observed rate versus the real rate for the implemented system with a buffer depth of 10 events and for a hardwired coincidence system

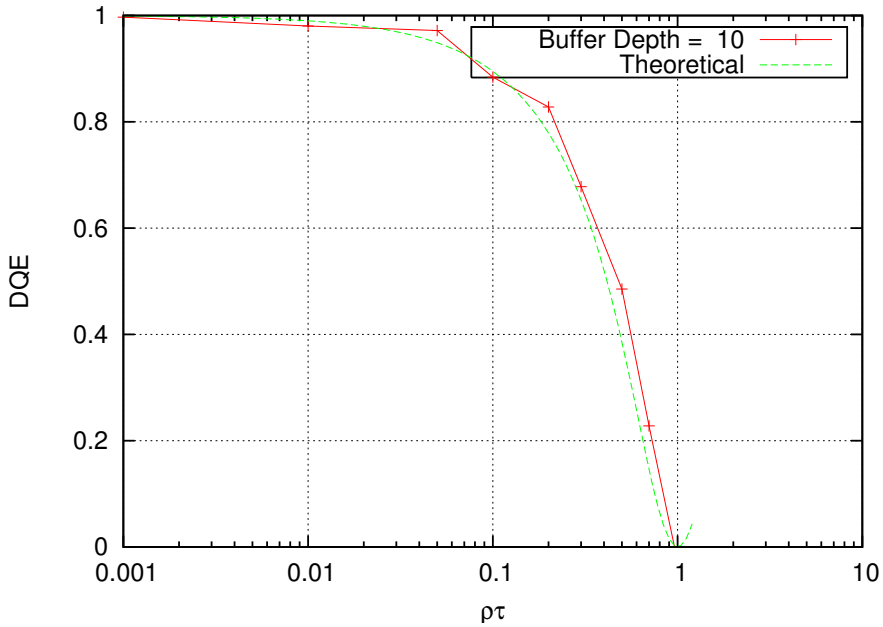

Fig. 5.4: The simulated DQE versus the theoretical DQE

$\chi = \rho \cdot \tau$. Mean can also be defined as $\frac{\chi}{\kappa} e^{-\chi}$. Using the following conversion;

$$\frac{\mathrm{N}'}{\Delta \mathrm{N}'} = \frac{E}{\sqrt{V}} = \frac{\frac{\chi}{\kappa} e^{-\chi}}{\sqrt{\frac{\chi}{\kappa} e^{-\chi}[1 - 2\chi e^{-\chi}]}} \tag{5.2}$$

the theoretical DQE can be calculated by following the steps starting from Eq. 2.38 in section 2.3.4.2.

The DQE of the simulated system has been calculated by generating up to billion events per point in the figure in order to get secondary statistics precise to the 3rd digit. Special care has been taken in random number generation. The Mersenne twister (MT19937) random number generator algorithm [Mat98] has been used for the excellent statistical properties and the nearly unreachable period ($2^{199937} - 1$). It is also useful to reproduce the generated random number sequences which was helpful for debugging the developed algorithms.

In Fig. 5.4 the simulated DQE and the theoretical DQE can be seen. The resulting DQE generated by the Monte Carlo simulation nicely fits to the theoretical curve. It is evident that the Monte Carlo simulation allows a good description of the performance and in addition allows almost an unlimited extension to the existing thoretical work.

Discussion

The study above showed that the soft coincidence concept performs at least as good as hardware coincidence systems. Now we would like to demonstrate its usefulness where the hardware coincidence systems are inferior.

In following sections, two new detector systems will be modelled and their operational and performace properties will be presented. Finally, they will be merged to form a Compton camera system with an extended soft coincidence concept and the performance of such a system will be compared in terms of DQE to a hardwired system with similar parameters.

5.4 Silicon Drift Detector with a Fast Trigger

The first detector system to be presented is a new type of 2D silicon drift detector [Cas04] developed in MPI which can easily be adapted for the Compton camera applications. The innovation in this detector, in addition to standard drift property, is a special configuration made on the back electrode that allows the extraction of trigger signals. 2D silicon drift detectors have very good position and energy resolutions. The energy resolution is better than 400 eV at 5.9 keV and the position resolution is of the order of 100 μm. In Fig. 5.5 the operation principle of such a detector is illustrated. 2D coordinate information can be extracted as follows: The Y-coordinate is simply given by the physical position of an anode that is attached to an energy channel as indicated for one channel in Fig.5.5. Typically anodes can be positioned with 100 μm pitch and a few hundreds of them lie along one side. The X-coordinate should be calculated. It is proportional to the time difference between the trigger and the energy signals as electrons drift along the X axis with a nearly constant drift speed. The maximal drift time can be of the order of microseconds. The back electrode which provides trigger signals, is divided into several trigger regions perpendicular to the drift direction. In this way the long drift time is subdivided into smaller drift times that are shifted in time. At the same time these trigger regions have less capacitance hence better signal quality and more precise trigger information.

The trigger signal is used both for a position resolution in one dimension and as a time stamp of a detected event that is essential for capturing Compton events. Despite the subdivision of

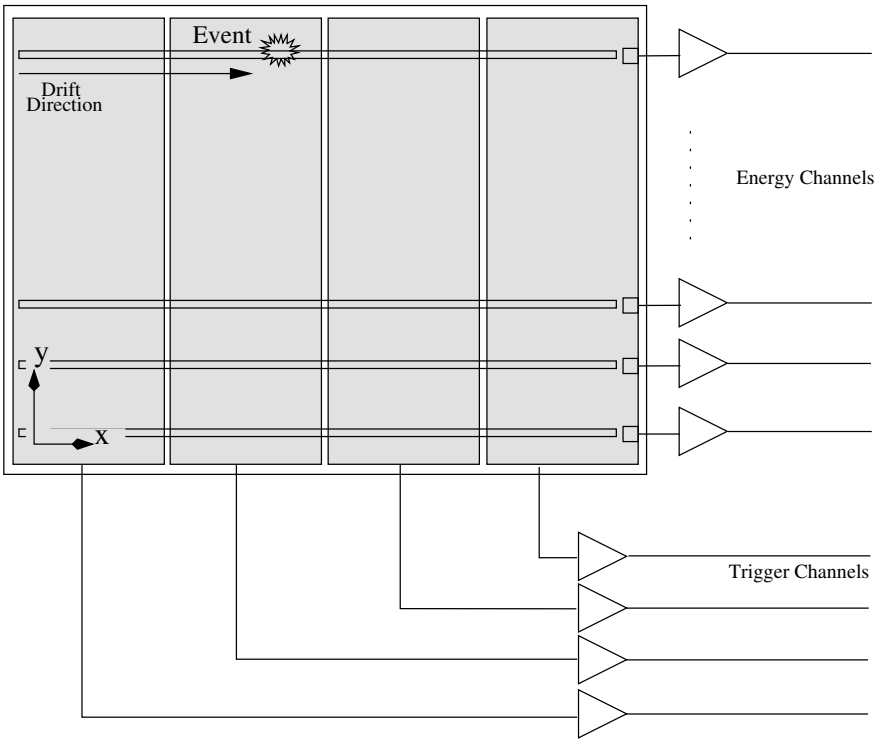

Fig. 5.5: 2D silicon drift detector with a fast trigger

the trigger, there are two types of ambiguities inherent in the event reconstruction in this type of detectors. This is due to the fact that, if multiple events occur during the drift process, it may not be possible to resolve events in time, which is required for position resolution in the drift direction.

We will define trigger region time window (TRTW) for the discussion below. TRTW equals to the drift velocity times the region width. The first type of ambiguity occurs if two events occur within the TRTW in the same trigger region. Then it is not possible to determine which energy signal belongs to a certain trigger signal. The second type of ambiguity occurs if two energy signals arrive within the TRTW of each other. Then it is not possible to resolve which trigger belongs to which energy signal.

Here an intelligent trigger resolving schema is proposed to minimize this sort of event losses. This schema ensures that if a trigger signal is detected, the next signal should be an energy signal in time. Otherwise it is not possible to resolve them within the drift time and they are vetoed. The veto mechanism blocks the detector until all respective energy signals are drifted and it waits for the maximum drift time to ensure that the detector is free of ambiguous signals.

Fig. 5.6 shows four events where one couple is accepted while other is rejected. In this figure each real event generates a trigger and an energy signal. For instance, (1t,1e) is a trigger and energy signal pair for the first event. As there is no additional trigger signal between the (1t) and (1e) signals, it is accepted and there is no need to wait for the maximum drift time. The second event also fulfills the same condition. The third event starts with the trigger signal (3t). As it can be observed, another trigger signal (4t) arrives before an energy is detected. So

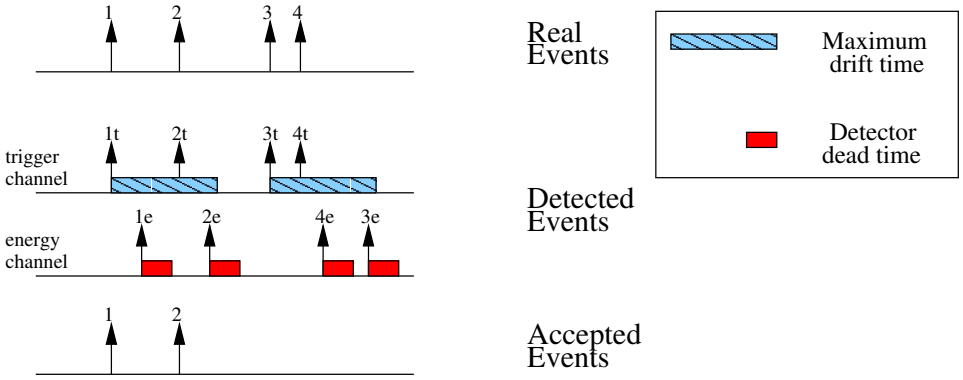

Fig. 5.6: The deadtime analysis for the fast SDD

the system vetoes both of these events and waits until the maximum drift time or two energy signals (3e,4e) appear, unless there is an additional trigger signal observed. Then the detector is signalled to be free and the event acceptance starts as above.

The coincidence simulations are made using the model described above for a single trigger region of the silicon detector and an ideal absorption detector. Multiple trigger regions can be added by shifting event reconstruction in time as well, without disturbing this single case. Typical parameters are chosen for the detector which are 1 μs drift time, 10 ns deadtime for the front-end electronics of the trigger signal and 100 ns deadtime for the front-end electronics of the energy signal.

The important parameters are chosen to be the real rate and the maximum drift time for this type of detectors.

In Fig. 5.7 the ratio of the observed and real events are presented as a function of the drift time for several real event rates considered. As the drift time increases, the ratio of the observed event rate drops exponentially. As we go to higher rates this drop in the observed rate is more pronounced. This can be understood as follows: The average drift time increases as we increase the maximum drift time. For a given constant incoming event rate which is coming from a Poisson process, most of the events having intervals less then the average drift time are rejected as illustrated in Fig. 5.6 and explained previously. So the form of the curves should be similar to the interval distributions curve shown in Fig. 2.46.

It is also interesting to see the processing power requirements for increasing rates, as the detector system itself performs an event identification/rejection algorithm. The operational complexity of the detector system is defined as the number of comparisons required to find an unambiguous event. In Fig. 5.8 the operation complexity is plotted with respect to the drift time. It can be seen from this plot that complexity increases nearly exponentially with an increasing maximum drift time. This is due to the fact that all the energy-trigger pairs are checked within the maximum drift time to identify unambiguous events where the number of comparisons may reach up to the factorial of the pairs.

As expected, at higher rates the increase is more significant. The interesting region for the implemented prototype in MPI is up to 2 μs maximum drift which corresponds to 20 comparisons

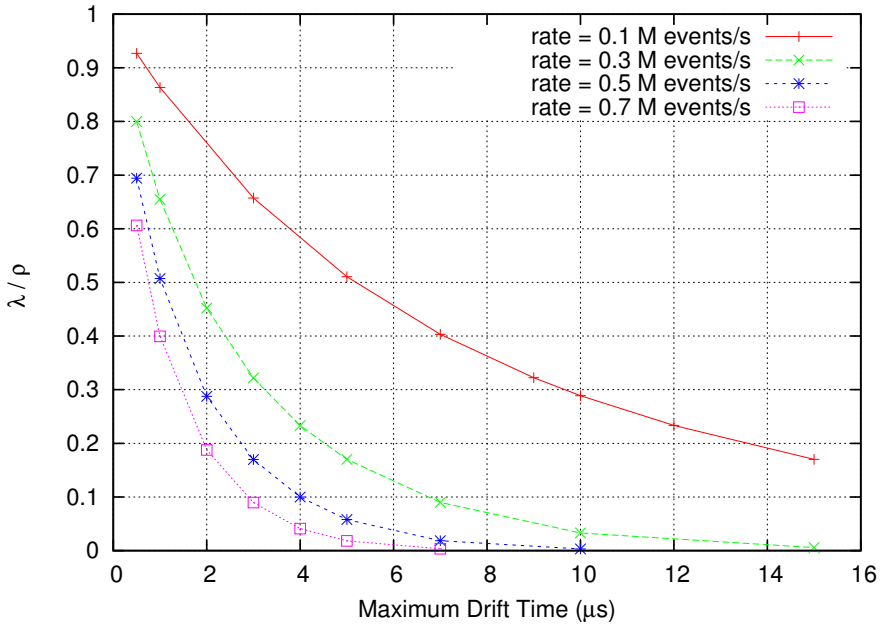

Fig. 5.7: The ratio of the observed and real events as a function of the maximum drift time for the fast SDD with different real rates

on the average. The processing element that will be designed for this detector should be capable of sustaining at least 10M comparisons per seconds plus data handling and transfer from detector system.

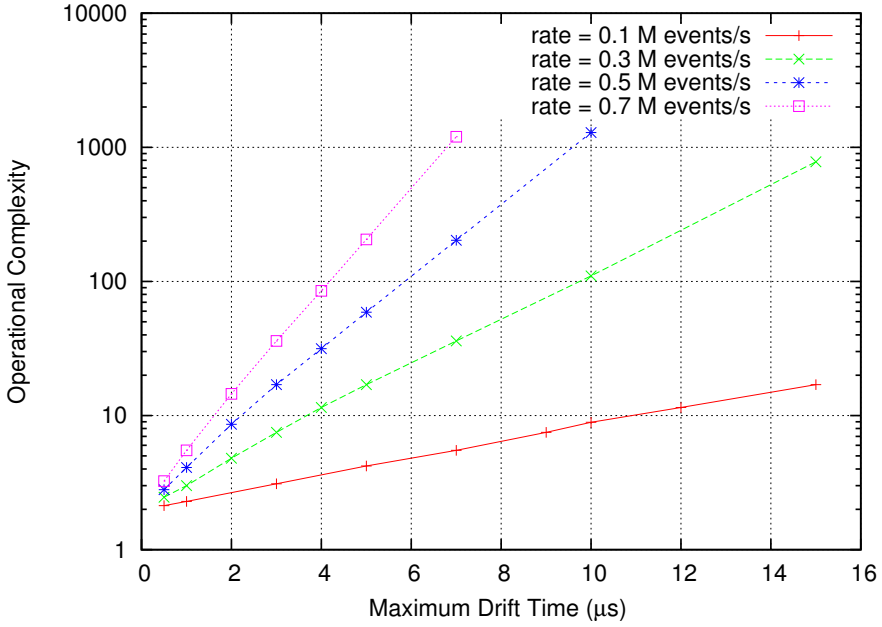

Fig. 5.8: The operational complexity as a function of the maximum drift time for different real rates

It can be stated that increasing the drift time both hinders the observed rate and adds a computational burden on the intelligent triggering schema.

5.5 Lithium Drifted Silicon Detector

Lithium drifted silicon (Si(Li)) detectors [Pro04] are 2D detectors and can be produced up to a few centimeters of thickness. A typical detector block is $70 \times 70 \times 10$ mm and consists of 32 parallel upper electrodes perpendicular to 32 lower electrodes in a mesh configuration. Since the γ-ray interaction rate increases with thickness, they are favourable as absorption detectors in Compton camera systems. The operation principle of the detector is shown in Fig. 5.9. When

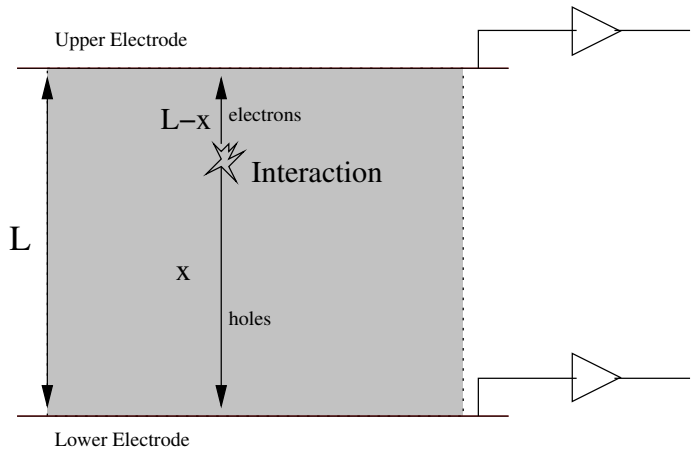

Fig. 5.9: The operation principle of the Lithium drifted silicon detector block

an interaction occurs within detector's sensitive volume, the produced electrons and holes drift to opposite electrodes due to potential difference. In order to find the depth of interaction which will give us more precision in defining the exact coordinates of the interaction, the timing model is defined with the equations below:

$$(t_e - t_o)v_e = L - x \tag{5.3}$$

$$(t_h - t_o)v_h = x \tag{5.4}$$

where the original event time is t_o. The detection time of the anode electrode signal is denoted by t_e which is due to the drift of electrons. The detection time of the cathode electrode signal is denoted by t_h which is due to the drift of holes. L is the thickness of the detector and x is the depth of interaction. v_e and v_h are the drift velocities for electrons and holes in the detector, respectively.

Solving equations 5.3 and 5.4 with the measurable values t_e, t_h, v_e, v_h and L being known, the unknown values t_o and x can be calculated as:

$$t_o = \frac{t_e v_e + t_h v_h - L}{v_e + v_h} \tag{5.5}$$

and x can be calculated using t_o and Eq. 5.4.

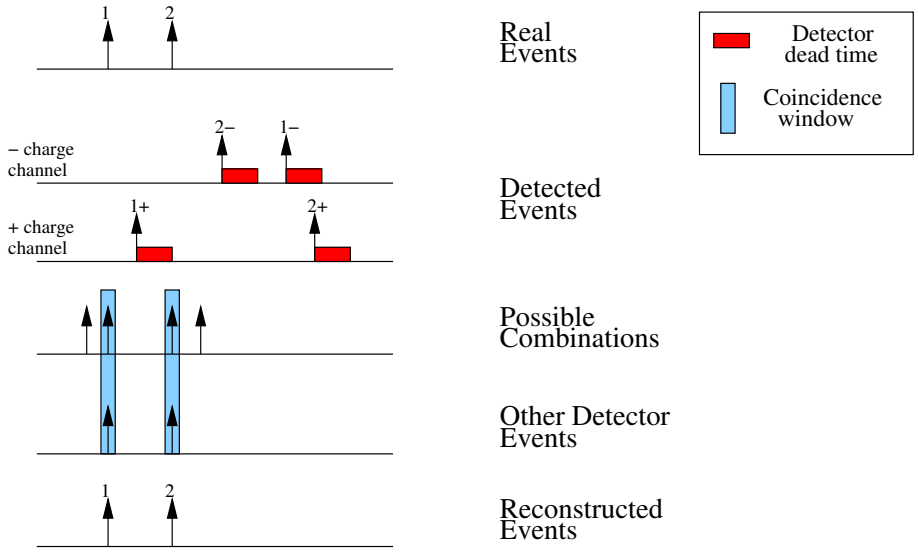

Fig. 5.10: The deadtime analysis for the Si(Li) detector

Obviously this calculations can only be done after recording the signals from upper and lower electrodes. An event reconstruction algorithm is developed that identifies and selects the correct coincident signal pairs with the help of the trigger signal information from the scatter detector system under high rate conditions.

The event reconstruction algorithm analyzing the effect of the deadtime is presented in Fig. 5.10. The reconstruction algorithm first records events for a certain time window which is chosen to be two times the maximum possible drift time for the simulations. Then the possible t_o time stamps are calculated with the recorded event pairs from the anode and the cathode which fulfill the timing constraints. The real events are reconstructed by comparing these t_o time stamps with the event time stamps obtained from the scatter detector system. The following simulations were performed by considering a combination of an ideal scatter detector and this type of a detector as an absorption detector. Fig. 5.11 shows coincidence simulations of such an absorption detector in combination with an ideal scatter detector. The event reconstruction concept proposed above works successfully and it can be seen that, the event reconstruction efficiency is very high for low rates. Even for rates as high as 1M events/s and drift length of 3 μs which means there are at least 3 or more events drifting in the detector for any moment, it is still possible to reconstruct events and to find correct signal pairs with the help of the precise trigger provided by the other detector. It should be stated that the quality of the event reconstruction depends on the precision of the trigger signals.

Fig. 5.12 shows how this operational complexity scales with the drift time and the real event rate. Operational complexity increases with the real rate.

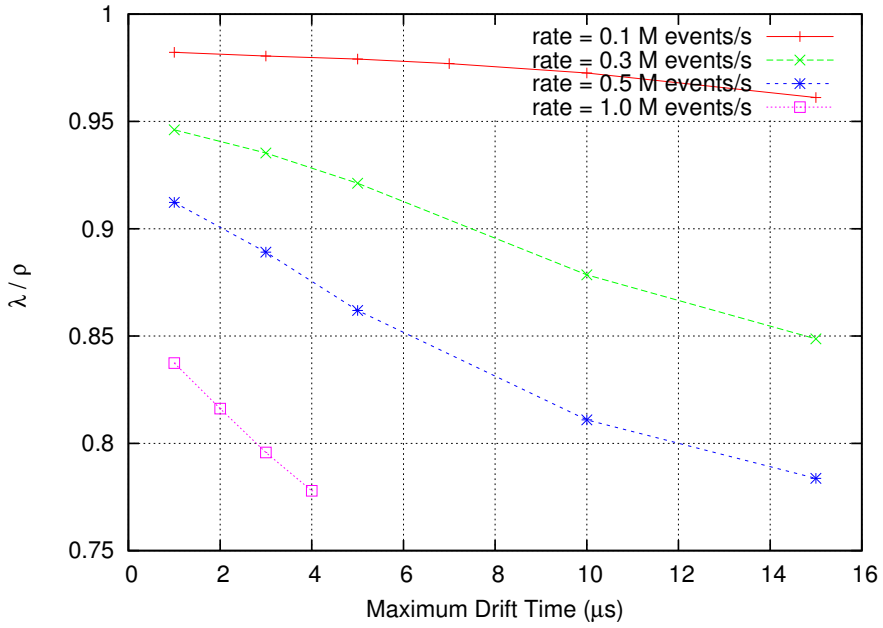

Fig. 5.11: The behaviour of the ideal scatter detector in combination with a Si(Li) absorption detector

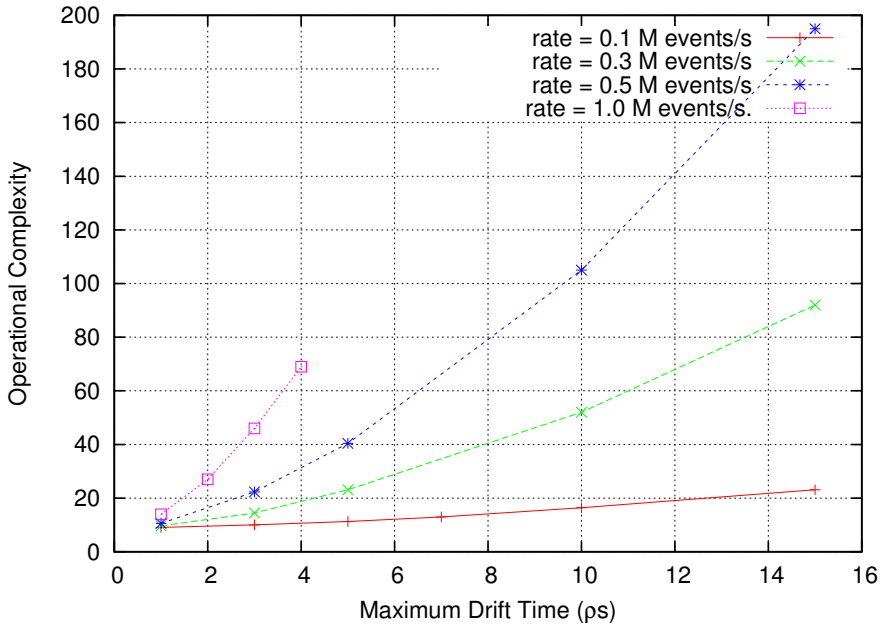

Fig. 5.12: Operation complexity of the ideal scatter detector and Si(Li) absorption detector

5.6 Combined Coincidences

The impact of the processing capability on deadtime and hence DQE, of a Compton coincidence system is studied with the two detector systems introduced in the previous sections. The scatter detector is a 2D fast silicon drift detector and the absorption detector is a Lithium drifted silicon detector.

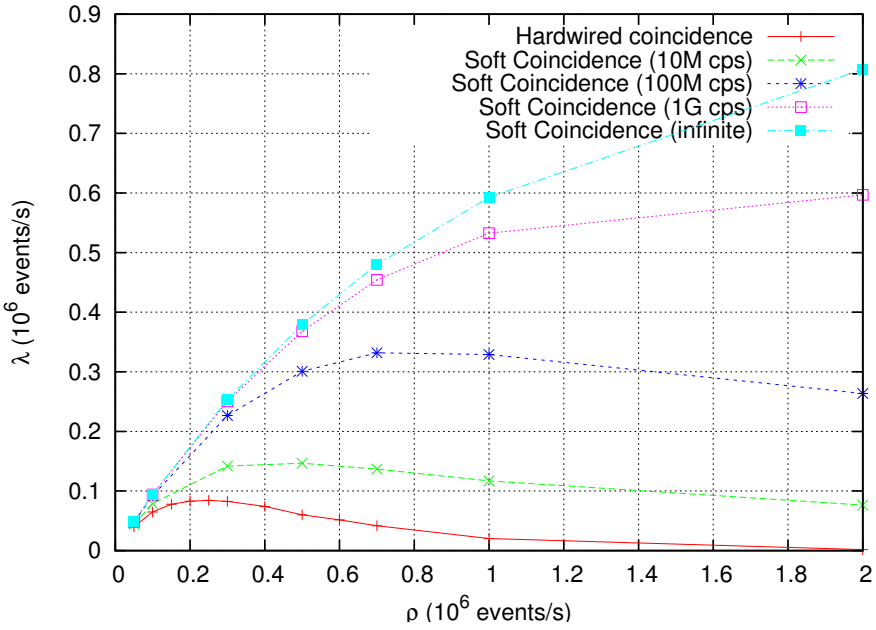

Fig. 5.13: The observed rate versus the real rate for different coincidence processors

Processing capability is simulated by a simple measure which is the number of comparisons performed per processed event. This number is then multiplied by the time spent per comparison and used as the deadtime of the coincidence processing system. The hardwired system for this simulation is defined as follows: There is no deadtime penalty for performing coincidences. The coincidence window should be at least as long as the drift time of the scatter detector as hardwired system is not capable of identifying complex timing relations. The multiple events that occur within a coincidence window are also rejected due to the fact that it is not possible to reconstruct scattered and absorbed events properly, which is required later by the image reconstruction.

The observed rate vesus the real rate with different operational costs are presented in Fig. 5.13. It is remarkable to see that with a reasonable processing power, a hardwired coincidence unit where no multiple events are allowed within the drift time, can be outperformed. The increased processing power has a positive impact on the observed rate.

In Fig. 5.14 DQE curves are plotted for different processing powers. Using processing units instead of a hardwired logic increases the DQE. In other words, for a DQE of 80% the coincidence processor can handle five times more input rate then a hardwired coincidence logic. It is observed that with the increasing processing power, physical characteristics of the detector systems become the major contributor to the event losses rather than the coincidence processing.

It is concluded that the complex system shows a similar behaviour like a single photon counting device demostrated in Chapter 2, with an *effective deadtime* (τ_{eff}) that can be determined with Monte Carlo simulations. This τ_{eff} scales with not only the processor speed alone, but also the primary and secondary detector's properties. The recent advances in computing enables such systems to reach their physical limits and processing these complex relations in realtime is

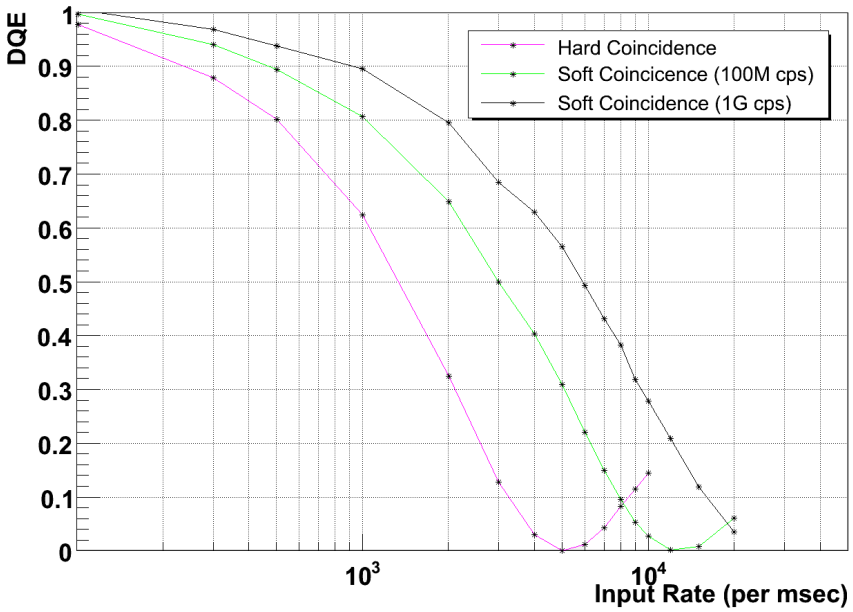

Fig. 5.14: The DQE as a function of the input rate for hard and soft processors

no more a problem.

Chapter 6

Conclusion

In this chapter, conclusions based on the previous chapters will be presented and based on the experience that has been acquired during the construction of the Compton camera prototype, an improved readout structure of a probable Compton camera imaging device for medical applications, will be proposed.

6.1 Conclusion on the Prototype Detector

A Compton prototype system for studying the various system parameters has been designed and constructed. It has been shown that, due to the complex nature of the Compton events, a readout system with similar complexity to a high energy physics experiment readout system is necessary.

The developed prototype Compton camera system is flexible enough for studying the performance of the Compton camera at different orientations and Compton kinematics. With the developed DAQ system the events from scatter and absorption detectors are fused and it has been shown that it is possible to reconstruct Compton events using time stamps of the corresponding events.

It has been shown for the first time with silicon drift detectors that it is possible to reconstruct Compton events by measuring scattered electron energy and position information from both detectors for mostly monochromatic radio-pharmaceuticals.

Deadtime simulations have been performed in order to find out how a Compton camera system scales with soft coincidences that uses time stamps. Simulations show that this type of system shows a paralyzible behavior as the rate increases. Furthermore this behaviour is similar to the single photon counting device with an *effective deadtime* that can be determined with the simulation. The *effective deadtime* scales with not only the processor speed alone, but also the primary and secondary detector's properties. The recent advances in computing enables such systems to reach their physical limits and processing these complex relations in realtime is no more a problem. It has also been shown that FIFO buffers with enough depth improves the overall performance.

A custom modular DAQ system has been designed that can support up to 32 independent

channels with independent delay, thresholds and buffers. DAQ system consists of 8 channel processor cards, an event builder card and a custom designed backplane which is used for high speed communications between the event builder and channel processor cards. Each channel processor card consists of 4 channel with independent ADCs running continuously at 66 MHz sampling clock. Each channel has a dedicated controller with peak finding and integral operators. A complex trigger logic is implemented within every channel processor card.

A dedicated stack processor has been implemented in VHDL which is integrated on the event builder card. This is an important achievement for this type of DAQ system. A soft processor that is implemented in an FPGA processor may work slower than a dedicated external DSP processor but there are several advantages of the soft processor. It is possible to extend the soft processor easily and add a few new op-codes that performs dedicated functions a lot faster than a hardwired external processor with a fixed instruction set. The proof of concept soft stack processor requires a very small program space due to the optimized registers and instructions. All bootstrap code with micro kernel allocates 96 bytes and all the DAQ executive program is around 250 bytes long that scans all signal channels, performs buffer and memory management and communication between DAQ system and the DAQ computer.

One bottleneck of the DAQ system is the communication speed between the DAQ system and the DAQ computer. It has a throughput of 500 kilobytes per second. This was more than enough for the prototype as all the events are processed and filtered by the DAQ system, but it is possible to improve the communication speed by 40-80 times using USB 2.0 or IEEE1394 serial protocols and adding appropriate physical layer converter chips.

6.2 Outlook

In this section a planned Compton Camera Imager (CCI) for Medical Diagnostics will be presented. The artists vision of the system is shown in Fig. 6.1. Such a system is proposed for detecting tumors that are not very deep in the body. It consists of multiple scatter and absorption detectors. The planned system is composed of CDDs (controlled drift detectors) [Cas04] which are principally silicon drift detectors with performance enhancements and additional CCD like integrating mode, as scatter detectors. Silicon detectors have no concurrence amongst other types of detectors as they have optimal Compton scatter profiles.

Absorption detectors may be of several types like crystals, lithium drifted silicon blocks, cadmium zinc telluride or germanium. Two types of these detectors have been chosen to investigate their performance for the planned CCI system.

- LSO crystal coupled with APDs (avalange photodiodes) have high efficiency and fast signals which are in the range of 20 - 40 ns. There are several disadvantages of these detectors. They are expensive to produce but this may reduce significantly with mass production techniques. They are pixelized and require ten thousands of channels to be read simultaneously which puts a great burden to the readout system.

- Si(Li) detectors [Pro04] have relatively less number of channels to be read and they op-

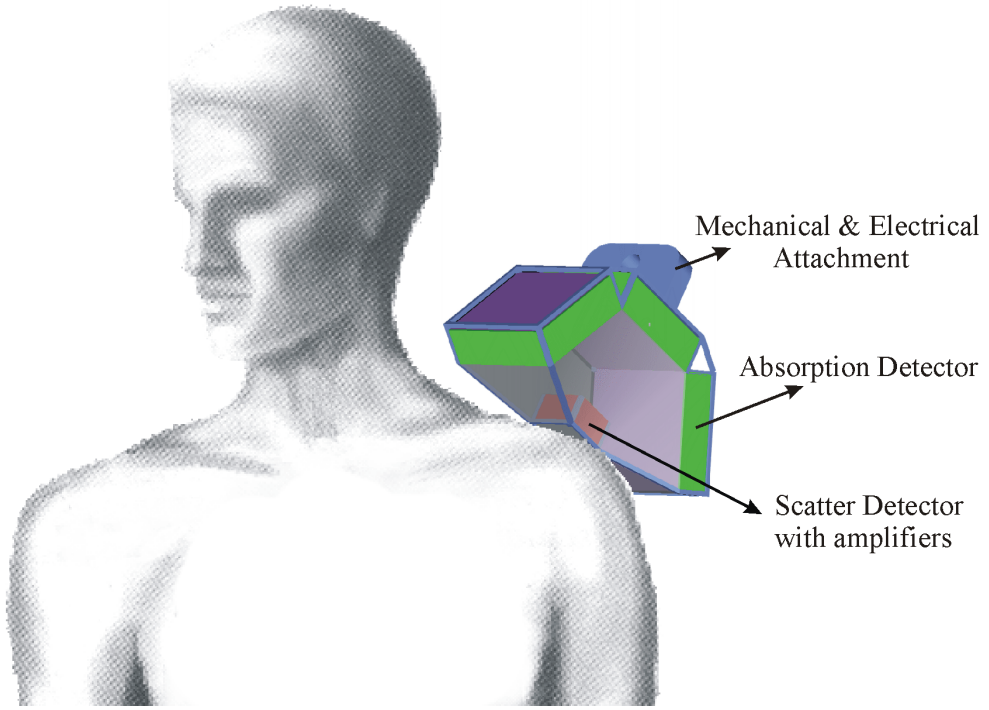

Fig. 6.1: Compton Camera Imager

erate at room temperature. The disadvantages of these detectors can be summarized as follows; the consecutive events may overlap at very high rates and have to be resolved with digital signal processing techniques [Bec02]. The exact time of interaction should be reconstructed after the signal has been recorded. However, these problems can be solved to a certain extend by cooling the detector and by emplying the event reconstruction method demostrated in the previous chapter.

The details of the detectors shown in Fig. 6.1 are as follows. The scatter detector is made of CDD chips. Each CDD chip is 4 x 2 cm^2 by .5 mm thick, and implemented on detector grade high purity silicon with 128 readout channels. 10-20 layers of CDD chips are stacked in order to increase the interaction probability. Total size of the scatter detector is 4 x 4 x 2 cm^3 where 20 layers of 2 CDD chips side by side with integrated readout chips. The Compton interaction efficiency of such a block is around 20%. If 1 mCi source is positioned 4 cm away from the detector each detector chip will receive $\sim$ 150k events/s which is a reasonable value.

Absorption detectors have an interaction efficiency of $\sim$ 60% and will be 10 x 10 cm^2 by 1 cm thick. The expected data rate per absorption detector block is around 2M events/s.

Overall efficiency of such a CCI system would be around 5-6%. This excellent efficiency as compared to Anger camera with collimator ($\epsilon \approx 10^{-4}$) is 500..600 times better where the reconstruction efficiency in the data processor besides the availibility of these new detectors plays a crucial role.

APPENDICES

Appendix A

Derivation of the Compton Formula

Let's consider the interaction given in Fig A. We would like to find a relation between initial and final energy and momentum of the photon which are denoted as $(E_\gamma, \overrightarrow{p}_\gamma)$ and $(E'_\gamma, \overrightarrow{p}'_\gamma)$. Initially the energy and momentum of the photon $(E_\gamma, \overrightarrow{p}_\gamma)$ is known and the electron is at rest $(\overrightarrow{p}_e = 0)$.

In order to solve this problem a few points should be remembered. The relativistic energy and momentum of a particle is related by an invariant equation given as;

$$E^2 = c^2|\overrightarrow{p}|^2 + m^2c^4 \tag{A.1}$$

where c is the speed of light and m is the rest mass of the particle. For photons this relation simplifies to $E_\gamma^2 = c^2|\overrightarrow{p}_\gamma|^2$ as the rest mass of the photon is zero , or the relativistic momentum of the photon can be defined as $\overrightarrow{p}_\gamma = \frac{E}{c}\overrightarrow{n}$ where $\overrightarrow{n} = \frac{\overrightarrow{p}_\gamma}{|\overrightarrow{p}_\gamma|}$ is the normal vector. Momentum

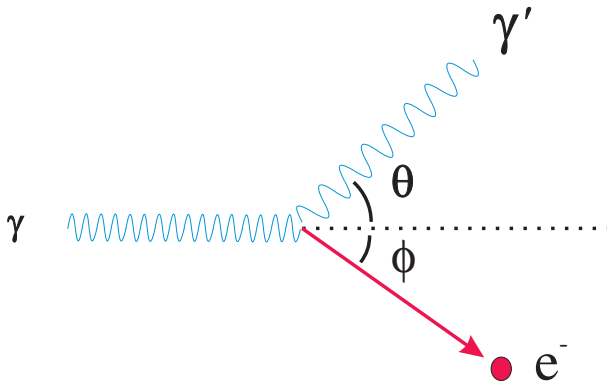

Fig. A.1: Compton Scattering Principle

and energy is conserved in any relativistic interaction.

$$\begin{aligned} \overrightarrow{p}_\gamma &= \overrightarrow{p}'_\gamma + \overrightarrow{p}'_e \quad \text{(Conservation of Momentum)} \\ E_\gamma + E_{e_{\text{rest}}} &= E'_\gamma + E'_e \quad \text{(Conservation of Energy)} \end{aligned}$$

where $E_{e_{\text{rest}}} = m_e c^2$. With simple manipulations,

$$\begin{aligned} \overrightarrow{p}_\gamma - \overrightarrow{p}'_\gamma &= \overrightarrow{p}'_e \\ (E_\gamma - E'_\gamma) + E_{e_{\text{rest}}} &= E'_e \end{aligned}$$

taking the squares of both equations,

$$\begin{aligned} |\overrightarrow{p}_\gamma|^2 + |\overrightarrow{p}'_\gamma|^2 - 2\overrightarrow{p}_\gamma \cdot \overrightarrow{p}'_\gamma &= |\overrightarrow{p}'_e|^2 \\ (E_\gamma - E'_\gamma)^2 + E^2_{e_{\text{rest}}} + 2E_{e_{\text{rest}}}(E_\gamma - E'_\gamma) &= (E'_e)^2. \end{aligned} \tag{A.2}$$

If we rewrite the momentum equation using the Eq. A.1 and multiplying both sides with

$$\frac{\cancel{c^2}E_\gamma^2}{\cancel{c^2}} + \frac{\cancel{c^2}(E'_\gamma)^2}{\cancel{c^2}} - 2c^2\overrightarrow{p}_\gamma \cdot \overrightarrow{p}'_\gamma = c^2|\overrightarrow{p}'_e|^2$$

$$E_\gamma^2 + (E'_\gamma)^2 - 2c^2\overrightarrow{p}_\gamma \cdot \overrightarrow{p}'_\gamma = (E'_e)^2 - m_e^2c^4. \tag{A.3}$$

subtracting Eq. A.3 from Eq. A.2 gives us,

$$2E_\gamma E'_\gamma + \cancel{E^2_{e_{\text{rest}}}} + 2E_{e_{\text{rest}}}(E_\gamma - E'_\gamma) + 2c^2\overrightarrow{p}_\gamma \cdot \overrightarrow{p}'_\gamma = \cancel{m_e^2c^4}$$

and,

$$\cancel{2}E_\gamma E'_\gamma + \cancel{2}E_{e_{\text{rest}}}(E_\gamma - E'_\gamma) = -\cancel{2}\cancel{c^2}\frac{E_\gamma}{\cancel{c}}\frac{E'_\gamma}{\cancel{c}}\overrightarrow{n}_\gamma \cdot \overrightarrow{n}'_\gamma$$

$$E_{e_{\text{rest}}}\frac{(E_\gamma - E'_\gamma)}{E_\gamma E'_\gamma} = 1 - \underbrace{\overrightarrow{n}_\gamma \cdot \overrightarrow{n}'_\gamma}_{\cos\theta}$$

where θ is the angle between two normal vectors and finally,

$$\frac{1}{E'_\gamma} - \frac{1}{E_\gamma} = \frac{1}{m_e c^2}(1 - \cos\theta) \tag{A.4}$$

Some useful derivations from this result as follows,

$$\boxed{E'_\gamma = \frac{E_\gamma}{1 + \frac{E_\gamma}{m_e c^2}(1 - \cos\theta)}}$$

$$\boxed{\cos\theta = 1 - m_e c^2\left[\frac{E_\gamma - E'_\gamma}{E_\gamma E'_\gamma}\right]}$$

Appendix B

Digitization Theory

B.1 Sampling Theory

In order to digitally process signals, they have to be quantized both in time and amplitude. Quantization in time is called sampling, and quantization of amplitude is called digitization.

Processing analog signals with digital systems requires sampling of the analog signal periodically. Generally sampling operation is not invertible; ie. for a given set of samples $x[n]$, there are infinite number of analog signals that can generate this output Fig. B.1 [AD].

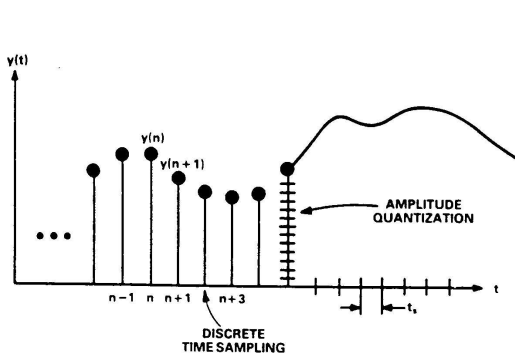

(a) Sampling and Quantization Schematic

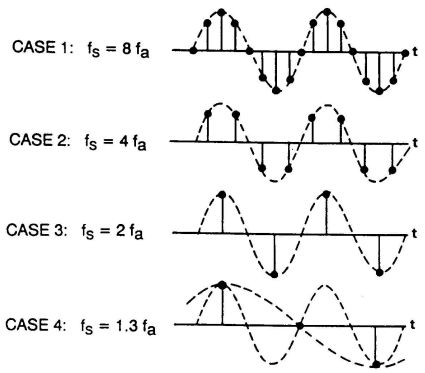

(b) Aliasing and different sampling

It is still possible to reconstruct an analog signal $x(t)$ using $x[n]$ if we pose certain restrictions on $x(t)$. These restrictions are provided by Shannon-Nyquist Sampling therorem that is stated as follows

Sampling Theorem: If $X(t)$ is a band-limited signal in frequency domain,

$$x(t) \xrightarrow{\mathcal{F}} X(f) \Longrightarrow \{X(f) = 0 \quad \textbf{for} \quad f > |f_m|\} \tag{B.1}$$

then $x(t)$ can be uniquely determined from its sampled values $x[n] = x(nT)$ where $T < \frac{1}{2f_m}$.

$f_s = \frac{1}{T}$ is called sampling frequency. Reconstructed signal is then given by;

$$x(t) = \sum_{n=-\infty}^{\infty} x[n] \frac{\sin(\pi f_s(t - nT))}{\pi f_s(t - nT)} \tag{B.2}$$

This has been first formulated by Harry Nyquist in 1928 but proved formally in 1949 by Claude E. Shannon.

Proof of the theorem is as follows:

We will first define a sampled version of the original signal in time domain

$$x_s(t) = x(t) \cdot T \sum_{n=-\infty}^{\infty} \delta(t - nT) \tag{B.3}$$

$$X_s(f) = \mathcal{F}\{x_s(t)\} = X(f) * \sum_{k=-\infty}^{\infty} \delta(f - \tfrac{k}{T}) \tag{B.4}$$

since $X_s(f)$ is periodic, it is possible to expand it in Fourier series in frequency domain.

$$X_s(f) = \sum_{n=-\infty}^{\infty} C_n e^{-\frac{j2\pi nf}{2f_m}} \tag{B.5}$$

and,

$$\begin{aligned} C_n &= \frac{1}{2f_m} \int_{-f_m}^{f_m} X_s(f) e^{\frac{j\pi nf}{f_m}} df \\ &= \frac{1}{2f_m} \int_{-\infty}^{\infty} X_s(f) \Pi(\tfrac{f}{2f_m}) e^{\frac{j\pi nf}{f_m}} df \end{aligned}$$

where $\Pi(\frac{x}{a}) = \begin{cases} 1 & \text{if} \quad x < |\frac{a}{2}|, \\ 0 & \text{elsewhere.} \end{cases}$ if $T = \frac{1}{2f_m}$then,

$$X(f) = X_s(f)\Pi(\tfrac{f}{2f_m}) \tag{B.6}$$

hence,

$$\begin{aligned} C_n &= \frac{1}{2f_m} \int_{-\infty}^{\infty} X(f) e^{\frac{j\pi nf}{f_m}} df \\ &= \frac{1}{2f_m} \mathcal{F}^{-1}\{X(f)\}_{t=\frac{n}{2f_m}} \\ &= \frac{1}{2f_m} x(\tfrac{n}{2f_m}) \end{aligned}$$

Now we can write Eq. B.5 as follows.

$$X(f) = \frac{1}{2f_m} \sum_{n=-\infty}^{\infty} x(\tfrac{n}{2f_m}) e^{-\frac{j2\pi nf}{2f_m}} \tag{B.7}$$

using conversion $T = \frac{1}{2f_m}$,

$$x(t) = \mathcal{F}^{-1}\{X(f)\} = \int_{-f_m}^{f_m} [T \sum_{n=-\infty}^{\infty} x(nT) e^{-j2\pi nTf}] e^{-j2\pi ft} df \tag{B.8}$$

as $X(f)$ is bandlimited with f_m, we change the integration limit respectively. Changing the order of summation and integration and rearranging the above formula yields,

$$x(t) = T \sum_{n=-\infty}^{\infty} x(nT) \int_{-f_m}^{f_m} e^{j2\pi f(t-nT)} df \tag{B.9}$$

the integral,

$$\int_{-f_m}^{f_m} e^{j2\pi f(t-nT)} = \frac{\sin(\pi 2 f_m (t-nT))}{\pi(t-nT)} \tag{B.10}$$

finally,

$$x(t) = \sum_{n=-\infty}^{\infty} x(nT) \frac{T}{\pi(t-nT)} \sin(\tfrac{\pi(t-nT)}{T}) \tag{B.11}$$

$$\boxed{x(t) = \textstyle\sum_{n=-\infty}^{\infty} x(nT) \mathrm{sinc}(\tfrac{(t-nT)}{T})}$$

where $\mathrm{sinc}(x) = \frac{\sin(\pi x)}{\pi x}$.

B.2 Quantization Error

Division of a continuous analog signal range into non-overlapping regions is called quantization. As maximum number of regions is a finite number, it is not possible to detect changes within a single region. Thus quantization error is defined as the difference between the actual analog value and its quantized representation. In Practice maximum number of regions $N = 2^{k-1}$ is chosen to be a power of 2 for a k bit quantizer.

Quantization error can be interpreted as noise. Assuming that the quantization error is uniformly distributed in the range $[-\frac{\Delta}{2}, \frac{\Delta}{2}]$, the power of the Quantization noise can be calculated as;

$$\sigma_q^2 = \int_{-\frac{\Delta}{2}}^{\frac{\Delta}{2}} x^2 \left(\frac{1}{\Delta}\right) dx = \frac{\Delta^2}{12} \tag{B.12}$$

B.3 Dynamic Range

Signal-to-Noise ratios are closely related to the concept of dynamic range. Where dynamic range measures the ratio between noise and the greatest un-distorted signal on a channel, SNR measures the ratio between noise and an arbitrary signal on the channel, not necessarily the most powerful signal possible. Because of this, measuring signal-to-noise ratios requires the selection of a representative or reference signal.

From this we can calculate maximum Signal to Noise Ratio (SNR) of an k bit analog digital converter as follows,

$$P_s = \frac{A^2}{\pi} \int_0^{\pi} \sin^2(x) dx = \frac{A^2}{2} \tag{B.13}$$

if we take $A = 2^{k-1}\Delta$ then $P_s = 2^{2k-3}\Delta^2$ from here,

$$\text{SNR} = 10 \log \left(\frac{2^{2k-3}\Delta^2}{\frac{\Delta^2}{12}} \right) = 6.02k + 1.76 \quad \text{dB} \tag{B.14}$$

Appendix C

MSTCPU16 Architecture

During the development of the Compton Camera DAQ system, the need for a programmable controller arised. An 16 bit stack processor with 2 kilowords of program memory and 1 megaword of data memory, has been designed and implemented for this purpose. The following figures show the internal structure, instruction set and definition of the memory mapped control registers.

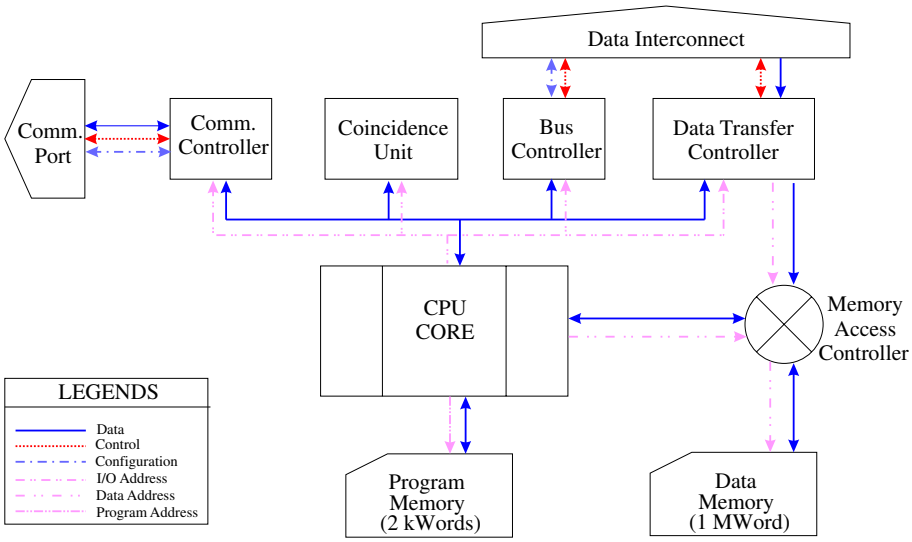

Fig. C.1: MSTCPU16 Peripherals

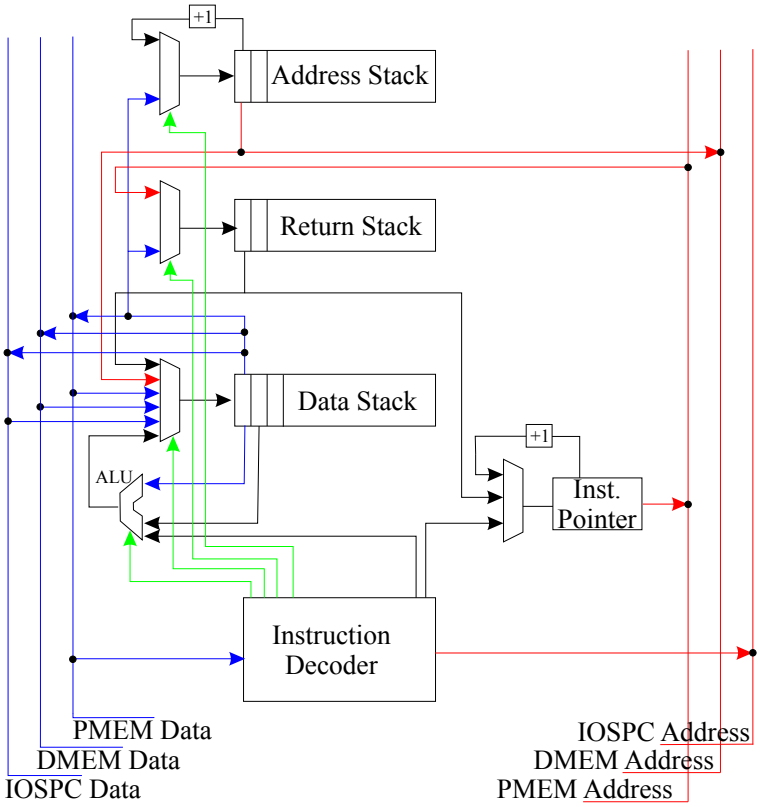

Fig. C.2: MSTCPU16 Internal Structure

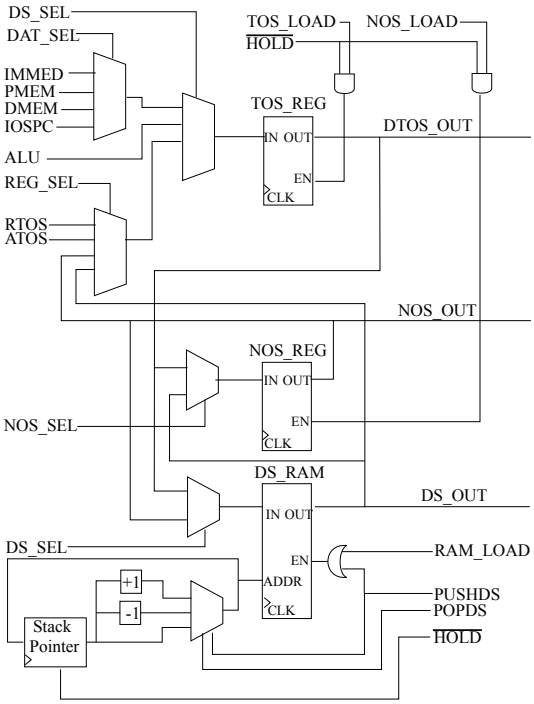

Fig. C.3: Data Stack Design

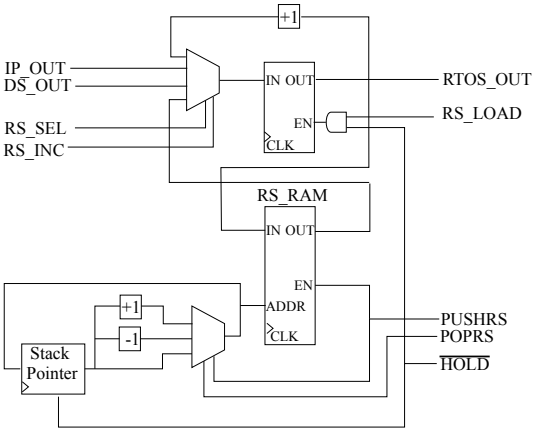

Fig. C.4: Return Stack Design

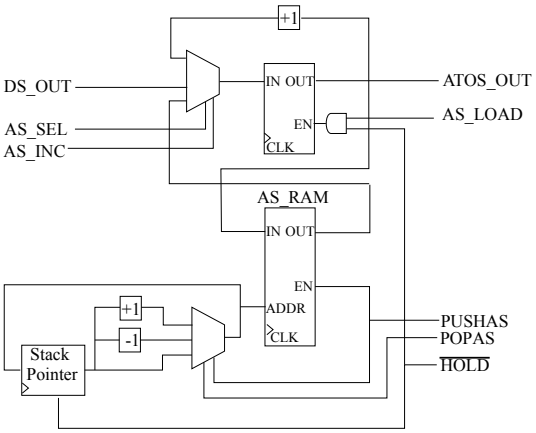

Fig. C.5: Address Stack Design

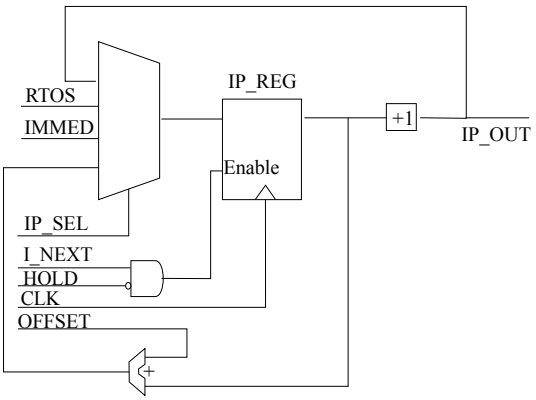

Fig. C.6: Instruction Pointer Design

Mnemonic	Size (bits)	Instruction Code	Argument (bits)	ST	C	Definition
CALL	16	F	12	RS:+1		subroutine call to absolute pmem address
RET	8	01		RS:-1		return from subroutine
JMP	16	E	12			unconditional branch to absolute pmem address
BRNZ	16	D	12	DS:-1		branch when dtos not zero (ip relative)
BRZ	16	C	12	DS:-1		branch when dtos zero (ip relative)
BRCC	16	B	12	DS:-1		branch when C = 0 (ip relative)
BRCS	16	A	12	DS:-1		branch when C = 1 (ip relative)
LIT	16	9	12	DS:+1		push immediate argument to ds
STP	16	8	12	DS:-1		pop ds ; store pmem (absolute addr)
LDP	16	7	12	DS:+1		load pmem (absolute address); push ds
OUT	16	40	8	DS:-1		pop ds ; store iospc (argument is iospc address)
IN	16	41	8	DS:+1		load iospc; push ds (argument is iospc address)
ST(A)	8	44		DS:-1		pop ds ; store dmem(atos) (atos indirect)
ST(A++)	8	45		DS:-1		pop ds; store dmem(atos); atos = atos+1
LD(A)	8	46		DS:+1		load dmem(atos); push ds (atos indirect)
LD(A++)	8	47		DS:+1		load dmem(atos); push ds ; atos = atos+1
ST(R)	8	48		DS:-1		pop ds ; store dmem(rtos) (rtos indirect)
ST(R++)	8	49		DS:-1		pop ds; store dmem(rtos); rtos = rtos+1
LD(R)	8	4A		DS:+1		load dmem(rtos); push ds (rtos indirect)
LD(R++)	8	4B		DS:+1		load dmem(rtos); push ds ; rtos = rtos+1
STP(A)	8	4C		DS:-1		pop ds ; store pmem(atos) (atos indirect)
STP(A++)	8	4D		DS:-1		pop ds; store pmem(atos); atos = atos+1
LDP(A)	8	4E		DS:+1		load pmem(atos); push ds (atos indirect)
LDP(A++)	8	4F		DS:+1		load pmem(atos); push ds ; atos = atos+1
ADD	16	30	8		√	dtos = dtos + argument
ADC	16	31	8		√	dtos = dtos + argument + C
SBC	16	32	8		√	dtos = dtos - argument - C
AND	16	33	8			dtos = dtos and 0xFF(argument)
OR	16	34	8			dtos = dtos or 0x00(argument)
XOR	16	35	8			dtos = dtos xor argument
LSLn	16	36	8			dtos shifted left by argument smaller than 0x0F
LSRn	16	37	8			dtos shifted right by argument smaller than 0x0F
ADD	8	20		DS:-1	√	dtos = dtos + dnos
ADC	8	21		DS:-1	√	dtos = dtos + dnos + C
SBC	8	22		DS:-1	√	dtos = dtos - dnos - C
AND	8	23		DS:-1		dtos = dtos and dnos
OR	8	24		DS:-1		dtos = dtos or dnos
XOR	8	25		DS:-1		dtos = dtos xor dnos
LSLn	8	26		DS:-1		dtos shifted left by dnos smaller than 0x0F
LSRn	8	27		DS:-1		dtos shifted right by dnos smaller than 0x0F
NOT	8	28				dtos = not(dtos)
BSWAP	8	29				bytes of dtos swapped
LSL	8	2A				dtos shifted left by 1
LSR	8	2B				dtos shifted right by 1
ROL	8	2C			√	dtos rotated left over C
ROR	8	2D			√	dtos rotated right over C
INC	8	2E				dtos = dtos + 1
DEC	8	2F				dtos = dtos - 1

Table C.1: MSTCPU16 Instruction Set I

Mnemonic	Size (bits)	Instruction Code	Argument (bits)	ST	C	Definition
DROP	8	10		DS:-1		top of data stack dropped
OVER	8	11		DS:+1		dnos copied and pushed back to ds
3RD	8	12		DS:+1		3rd element copied and pushed back to ds
SWAP	8	13				dnos and dtos swapped
ROT	8	14				top 3 element on ds rotated from bottom to top
NROT	8	15				top 3 element on ds rotated from top to bottom
>R	8	16		DS:-1,RS:+1		pop ds; push rs
<R	8	17		DS:+1,RS-1		pop rs; push ds
LDR	8	18		DS:+1		load rs; push ds
STR	8	19		RS:+1		load ds; push rs
DUP	8	1A		DS:+1		duplicate top of ds
>A	8	1B		AS:+1,DS:-1		pop ds; push as
<A	8	1C		AS:-1,DS:+1		pop as; push ds
LDA	8	1D		DS:+1		load rs; push ds
STA	8	1E		AS:+1		load ds; push as

Table C.2: MSTCPU16 Instruction Set II

ADDRESS	BITS																REGISTER NAME
	F	E	D	C	B	A	9	8	7	6	5	4	3	2	1	0	
CPU INTERNAL																	
0x00																C	STATUS
0x01													PAGE				RSPAGE
0x02													PAGE				ASPAGE
0x03													G3	G2	G1	R	LEDS
0x04	GENERAL PURPOSE REGISTER																GPR0
0x05	GENERAL PURPOSE REGISTER																GPR1
0x06	GENERAL PURPOSE REGISTER																GPR2
0x07	GENERAL PURPOSE REGISTER																GPR3
COMMUNICATIONS CONTROLLER UNIT																	
0x08	DATA																PPORT_DATA
0x09											CN				RCV	SND	PPORT_CTRL
BUS CONTROLLER UNIT																	
0x10					FL	CHANNELS					MODULES						DAQ_AVAIL
0x11							DATA_SRC					MODULE_ADDR				CH_ADDR	DAQ_ADDR
0x12											EN	PA	RS	..	PG	CLK	DO	DI	DAQ_CTRL
DATA TRANSFER CONTROLLER UNIT																	
0x18																	DMA_PAGE
0x19	DMA BASE ADDRESS																DMA_ADDR
0x1A	DMA BURST LENGTH																DMA_LENGTH
0x1B											PL					ST	DMA_CTRL
COINCIDENCE UNIT																	
0x20																	COIN_BASE_H
0x21																	COIN_BASE_M
0x22																	COIN_BASE_L
0x23																	COIN_COMP_H
0x24																	COIN_COMP_M
0x25																	COIN_COMP_L
0x26	COINCIDENCE UNIT REG7																COIN_HTHR
0x27	COINCIDENCE UNIT REG8																COIN_LTHR
0x28																	COIN_RESULT

Table C.3: MSTCPU16 IOSPC Address Map

Appendix D

Schematics

In the following pages circuit schematics for backplane, channel processor module and event builder module are presented.

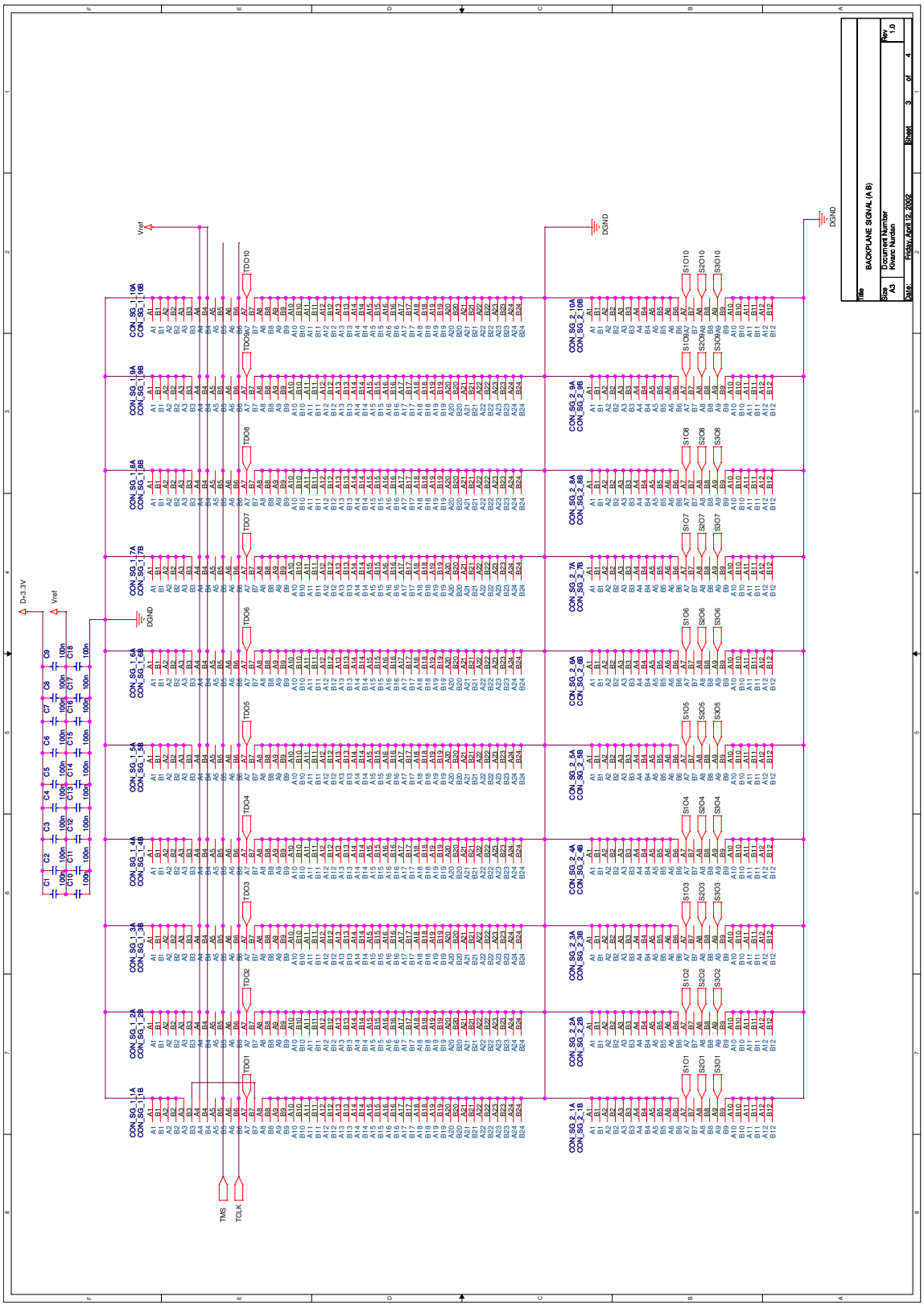

Fig. D.1: Backplane ground and serial connections

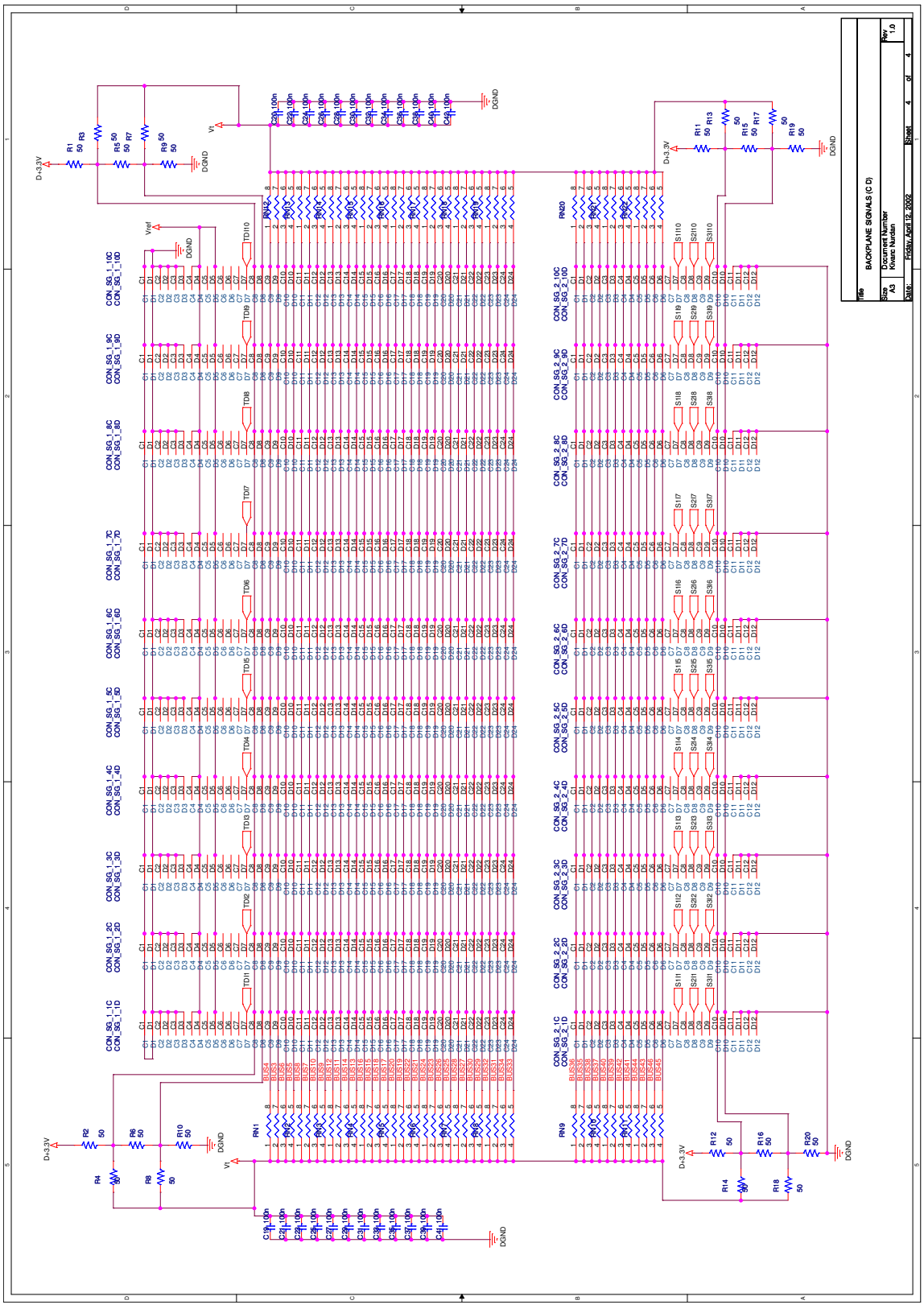

Fig. D.2: Backplane signal interface

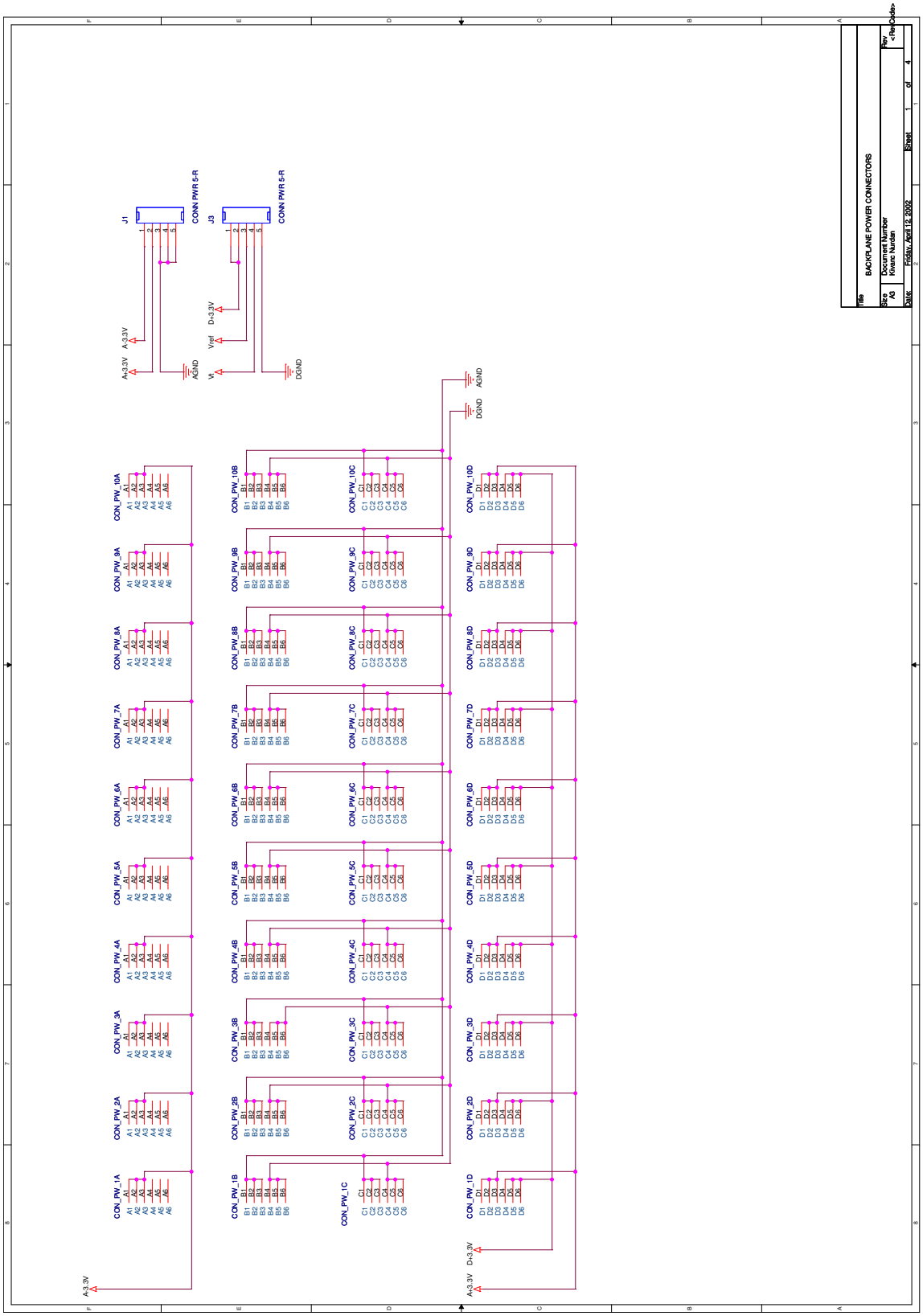

Fig. D.3: Backplane power distribution

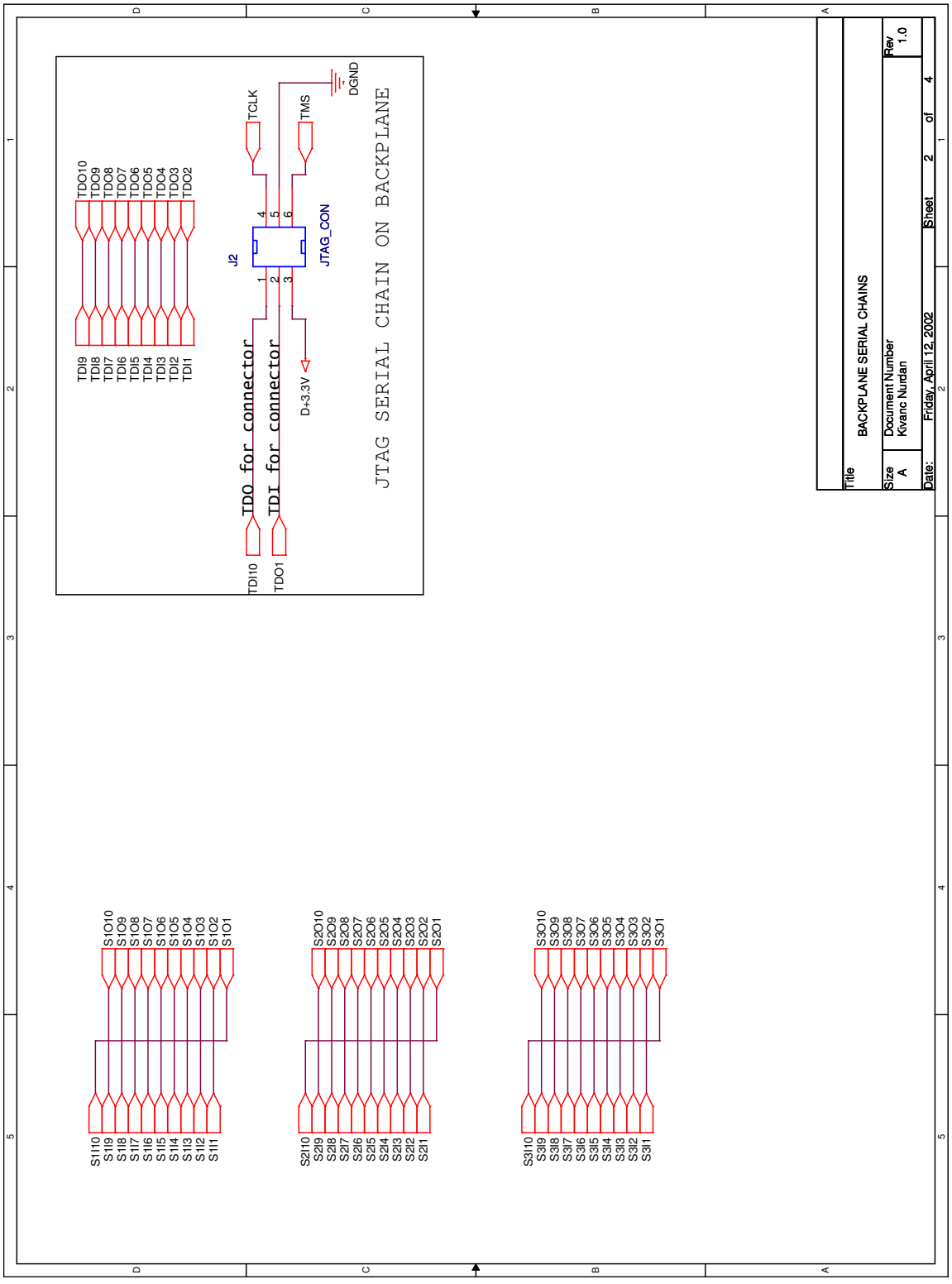

Fig. D.4: Backplane serial and JTAG chains

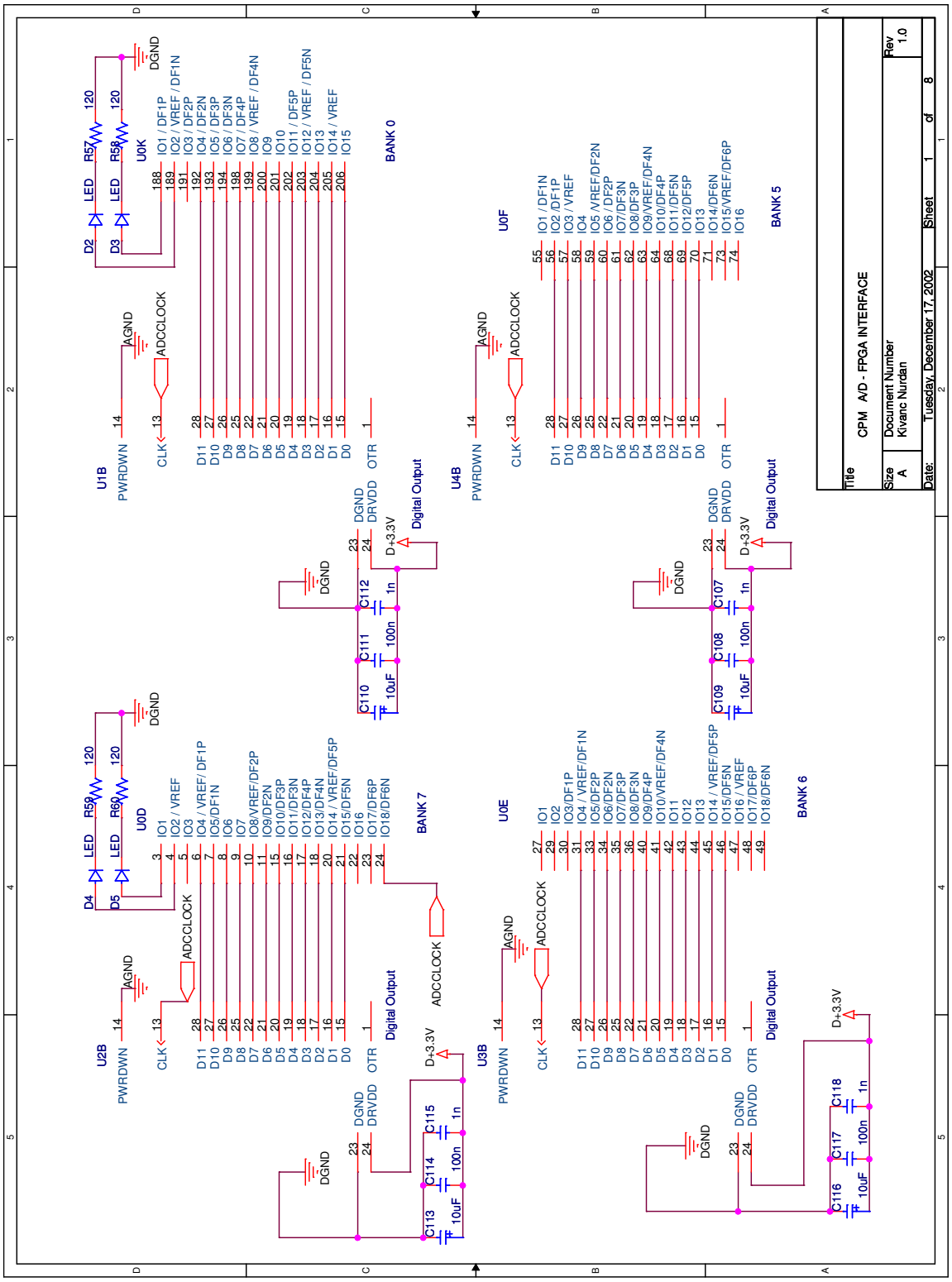

Fig. D.5: Channel processor module FGPA to A/D converter interface

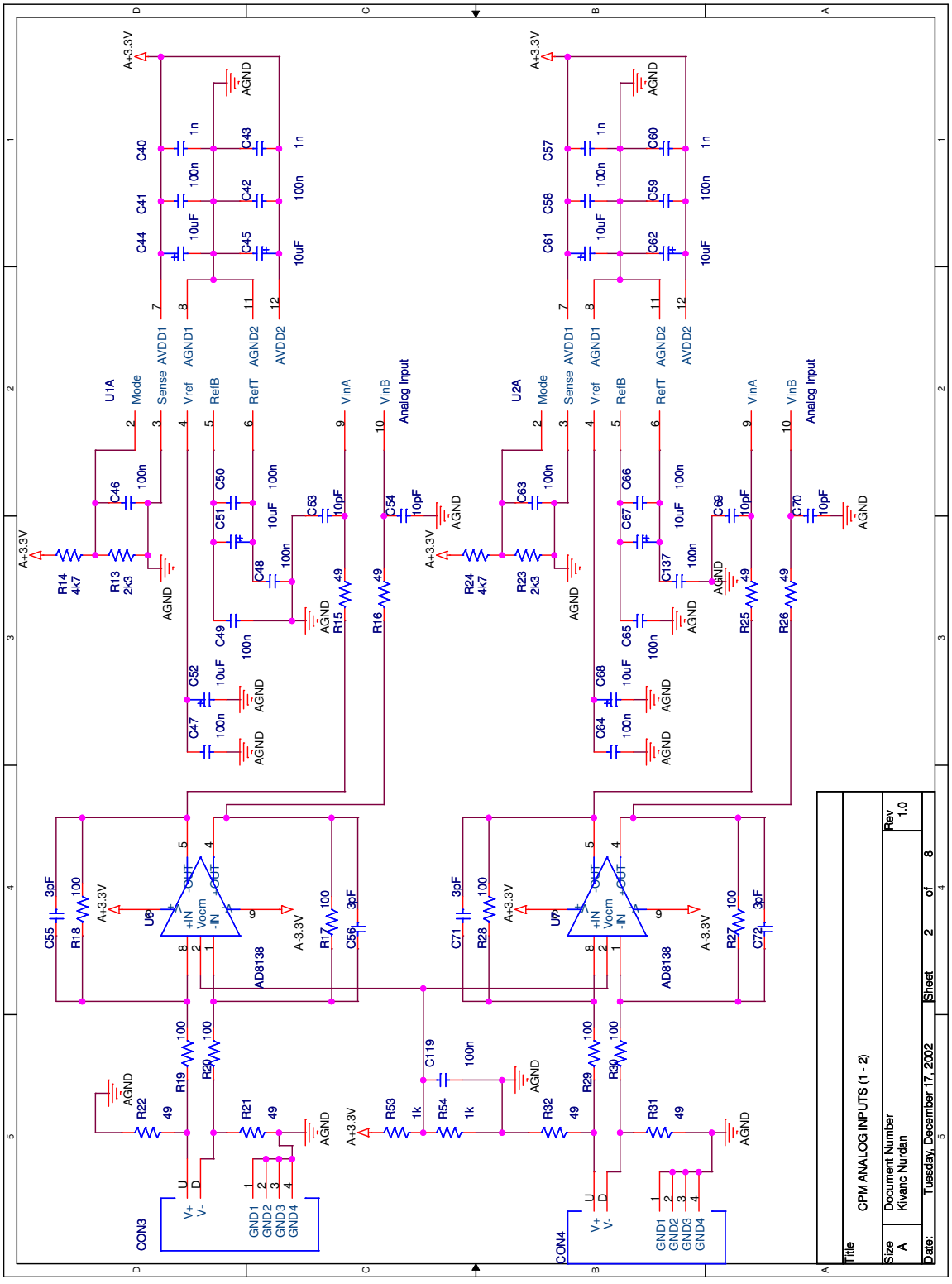

Fig. D.6: Channel processor module analog signal interface I

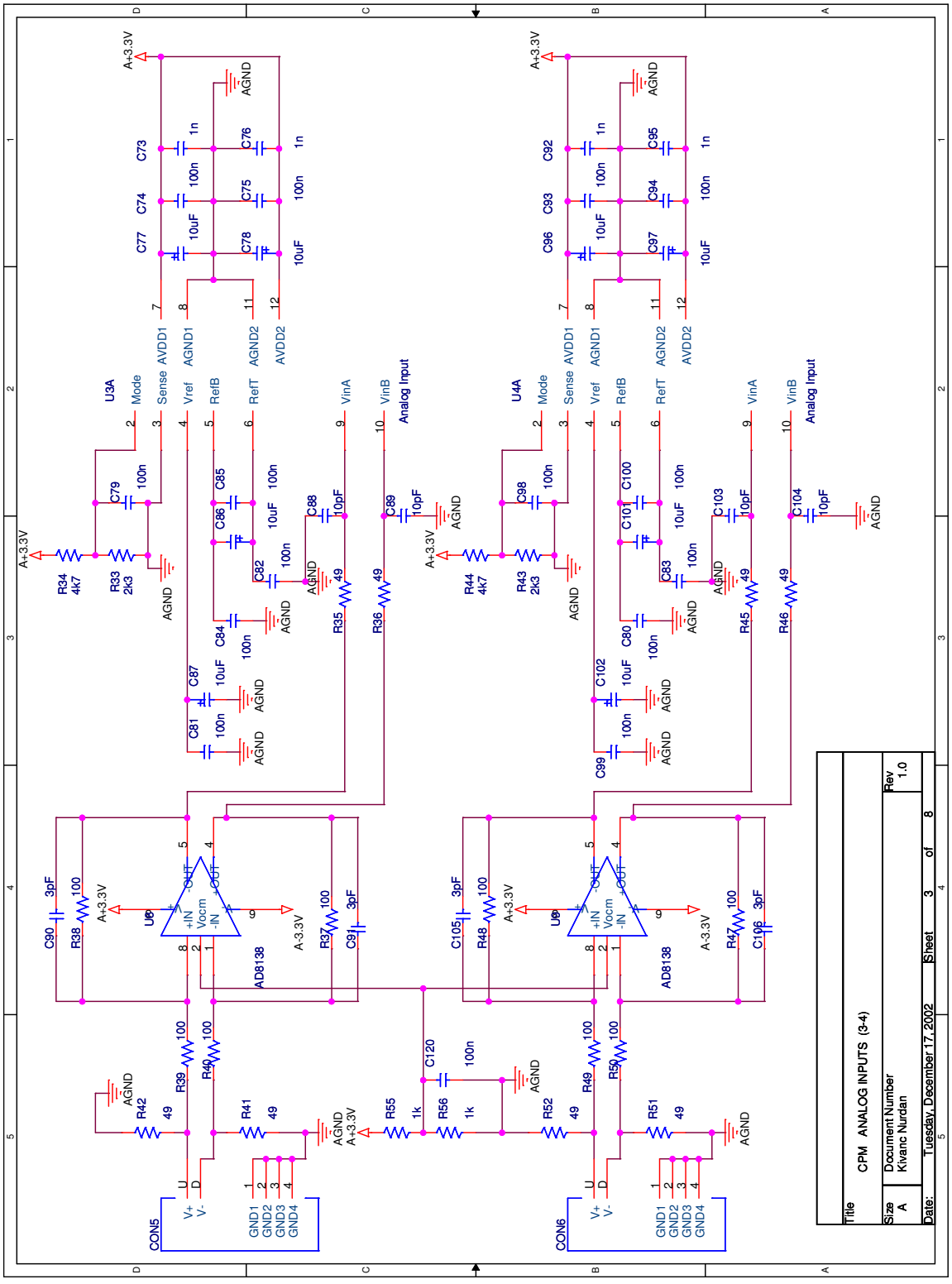

Fig. D.7: Channel processor module analog signal interface II

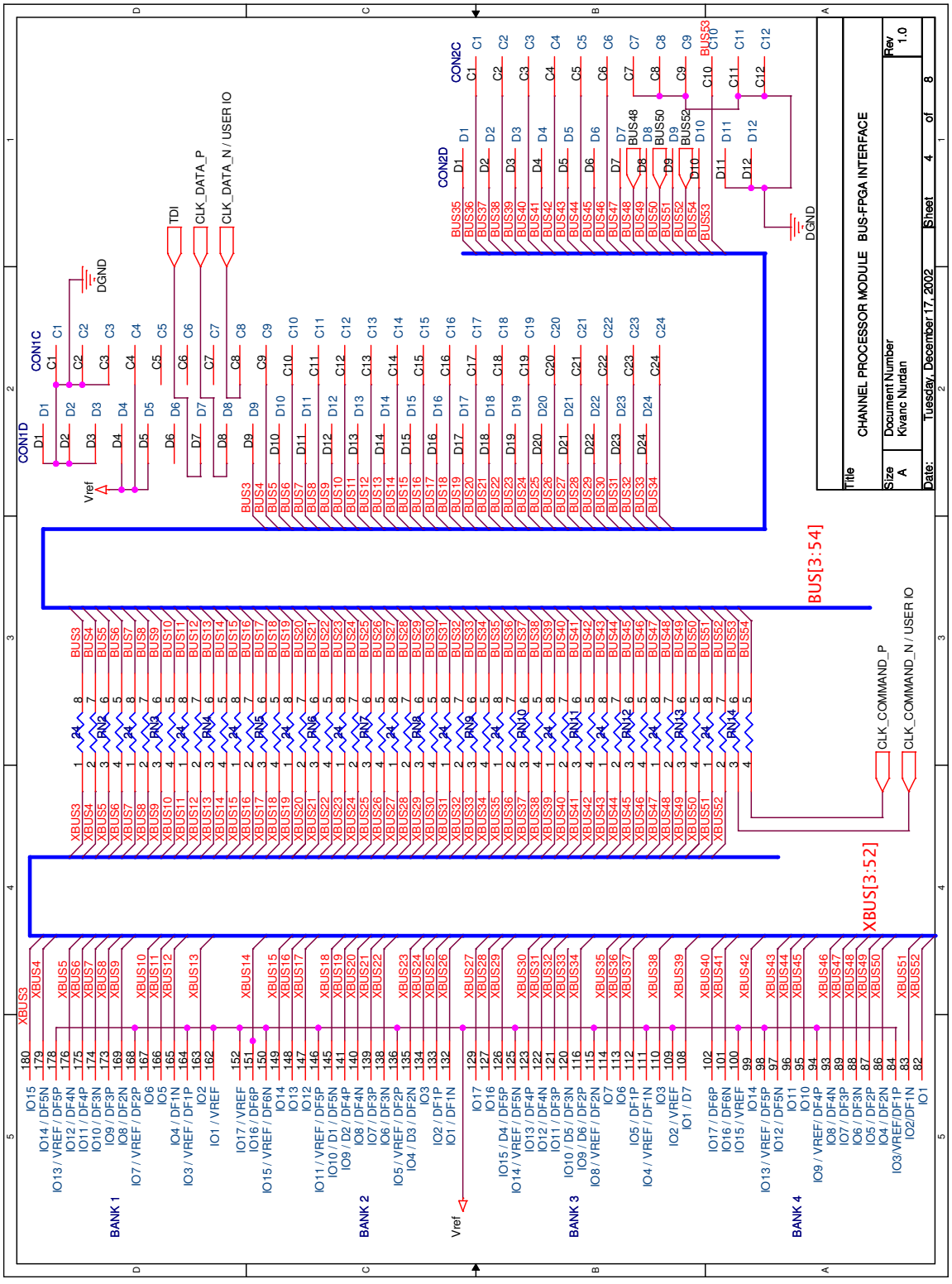

Fig. D.8: Channel processor module backplane interface

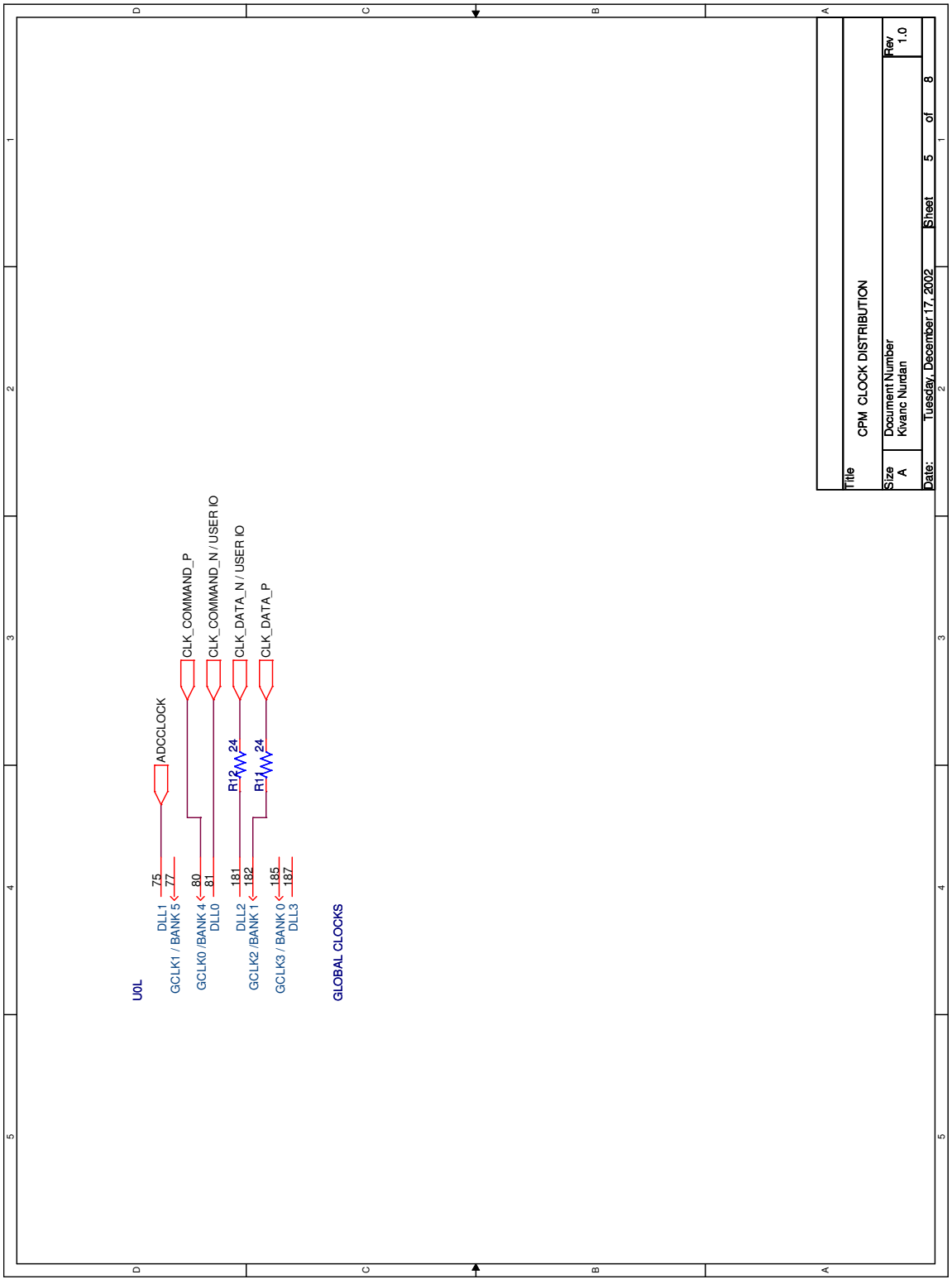

Fig. D.9: Channel processor module clock distribution

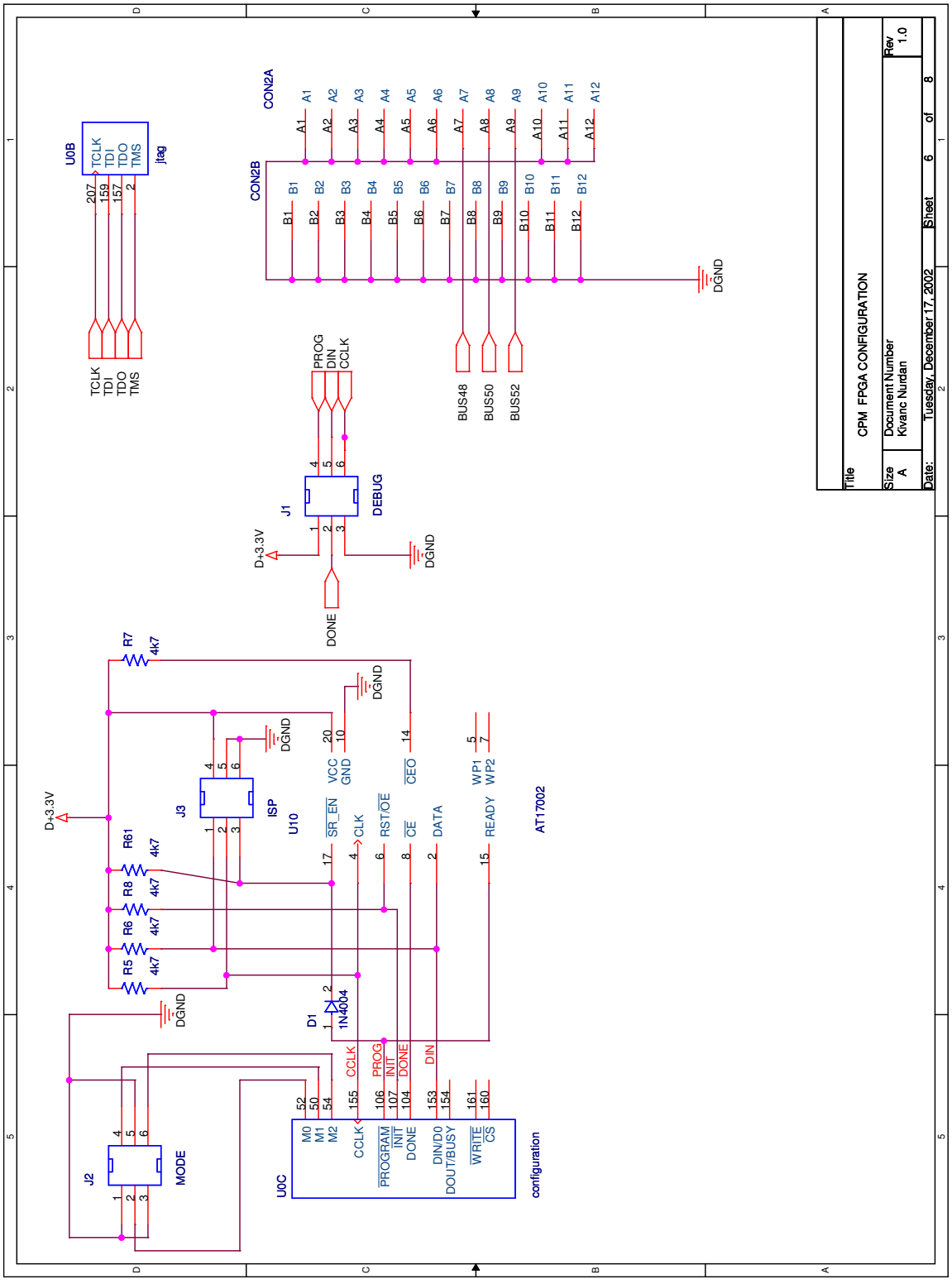

Fig. D.10: Channel processor module FPGA configuration EEPROM

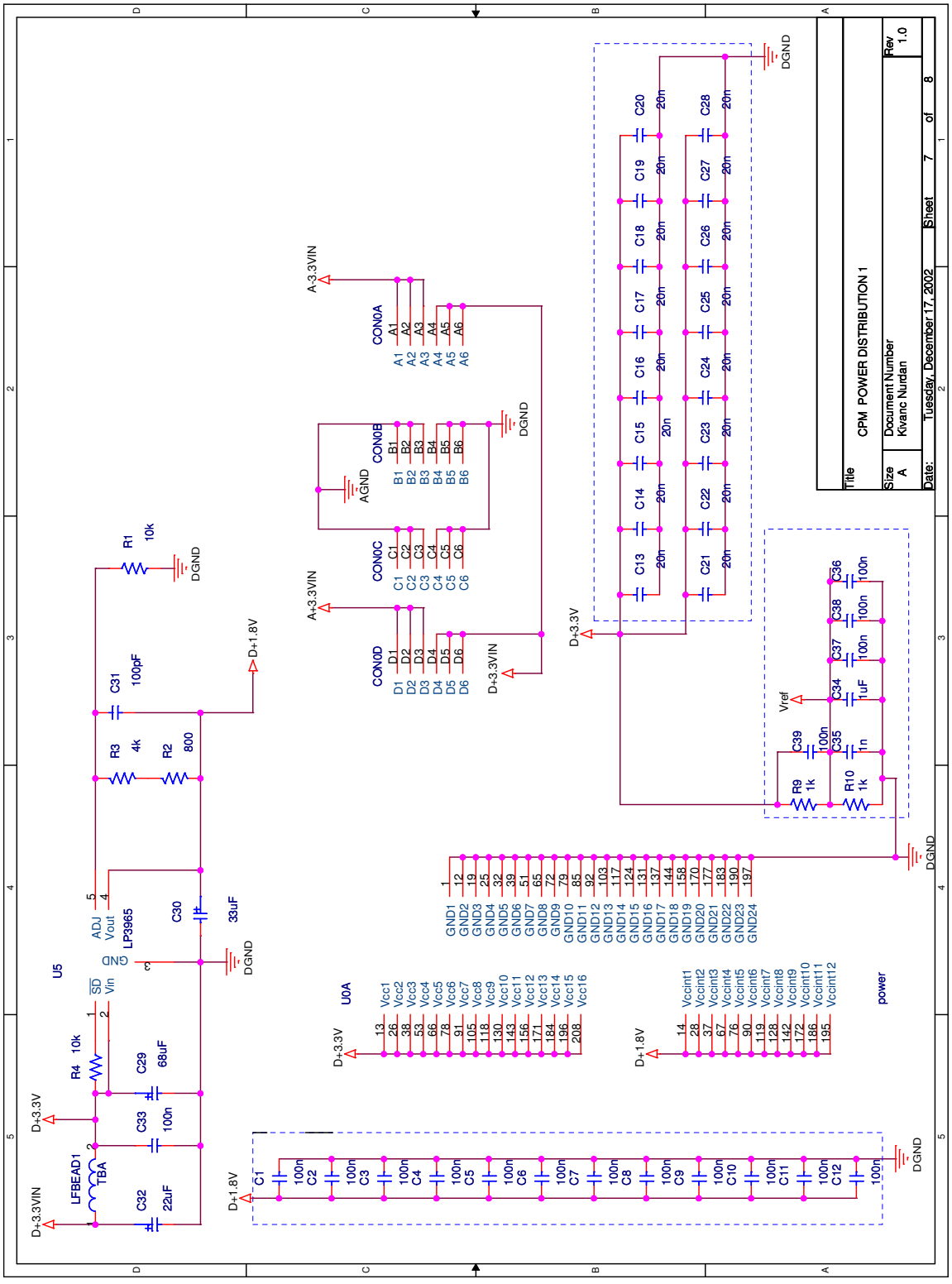

Fig. D.11: Channel processor module power distribution I

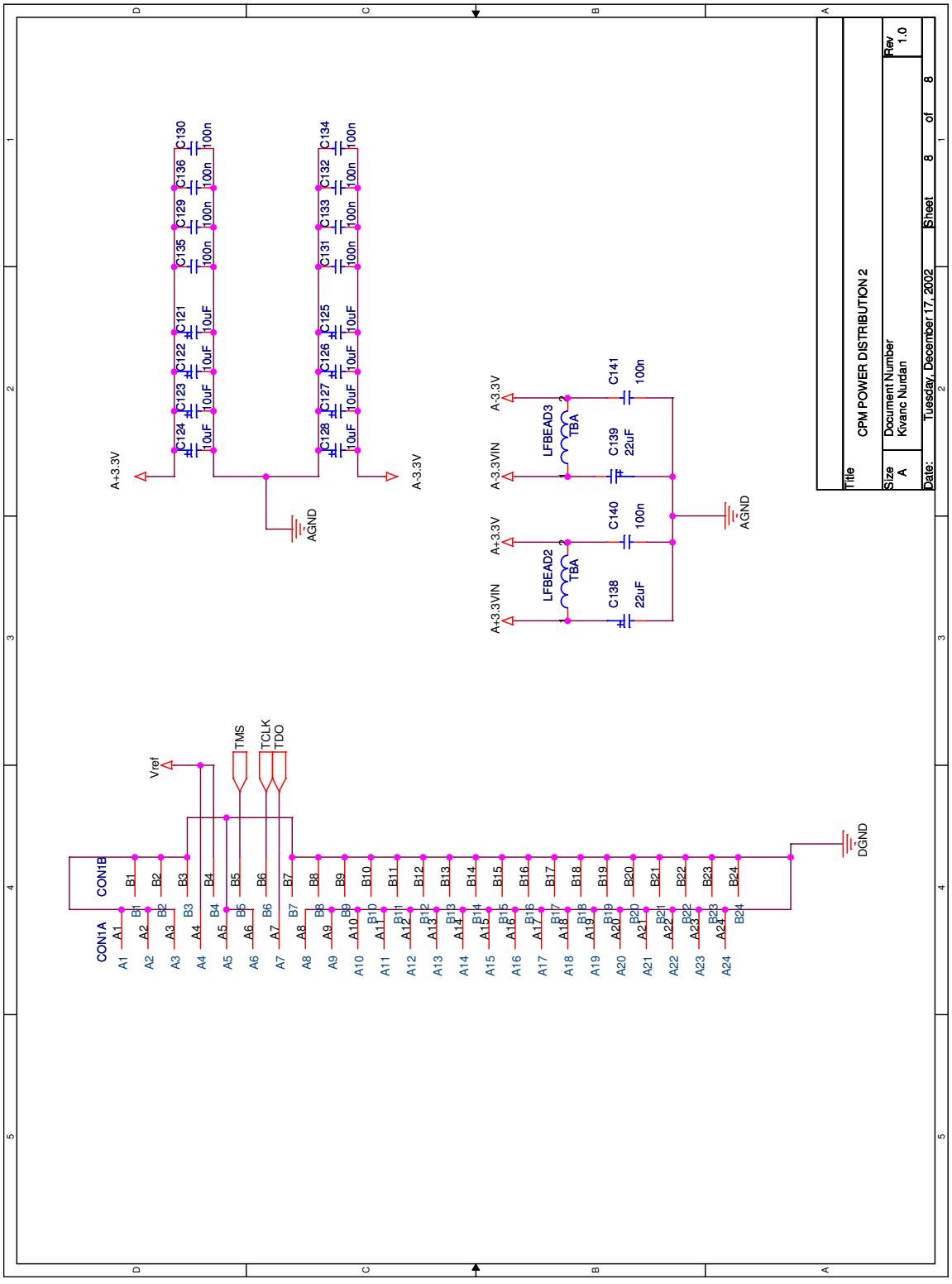

Fig. D.12: Channel processor module power distribution II

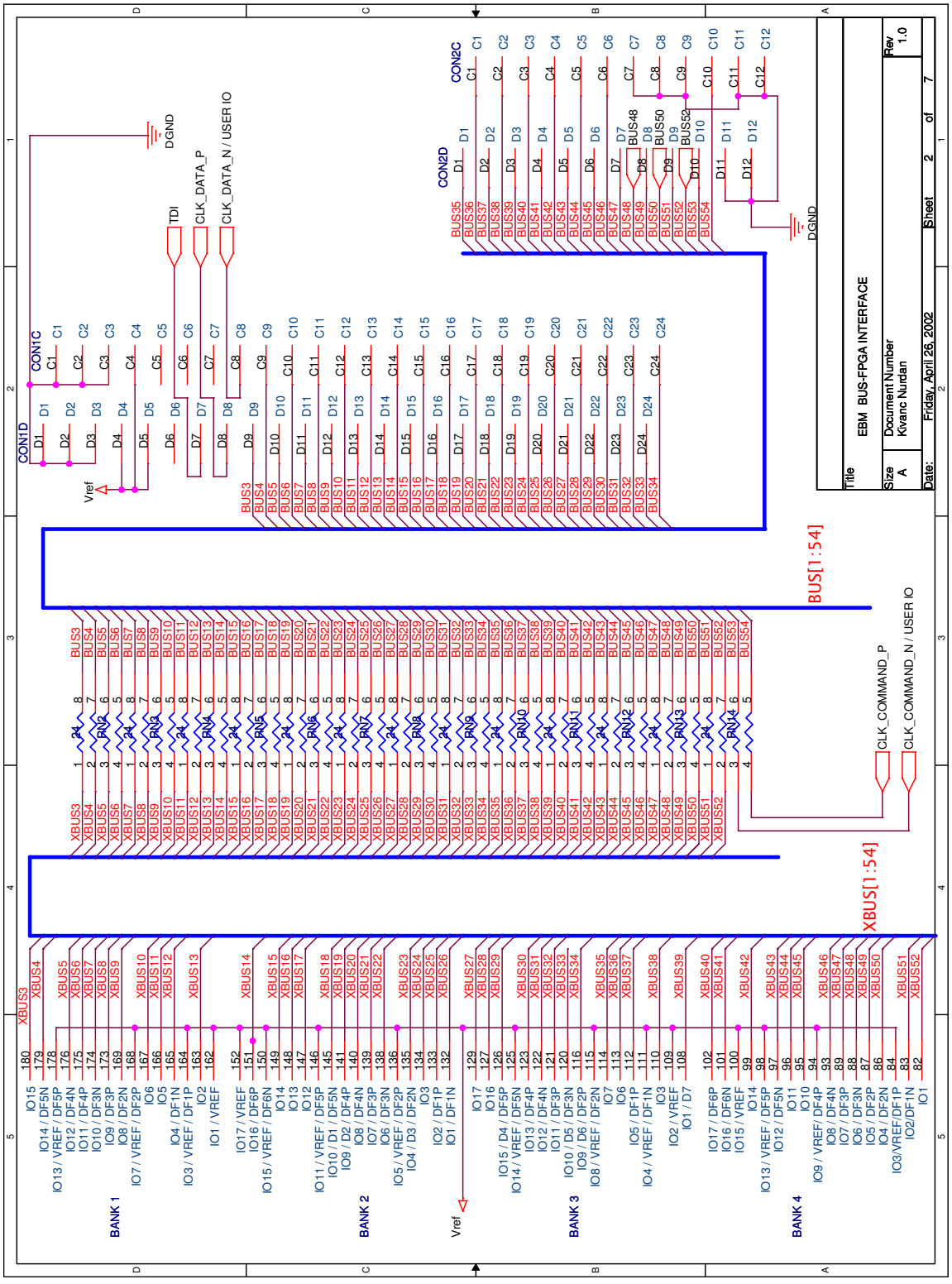

Fig. D.13: Event builder module backplane interface

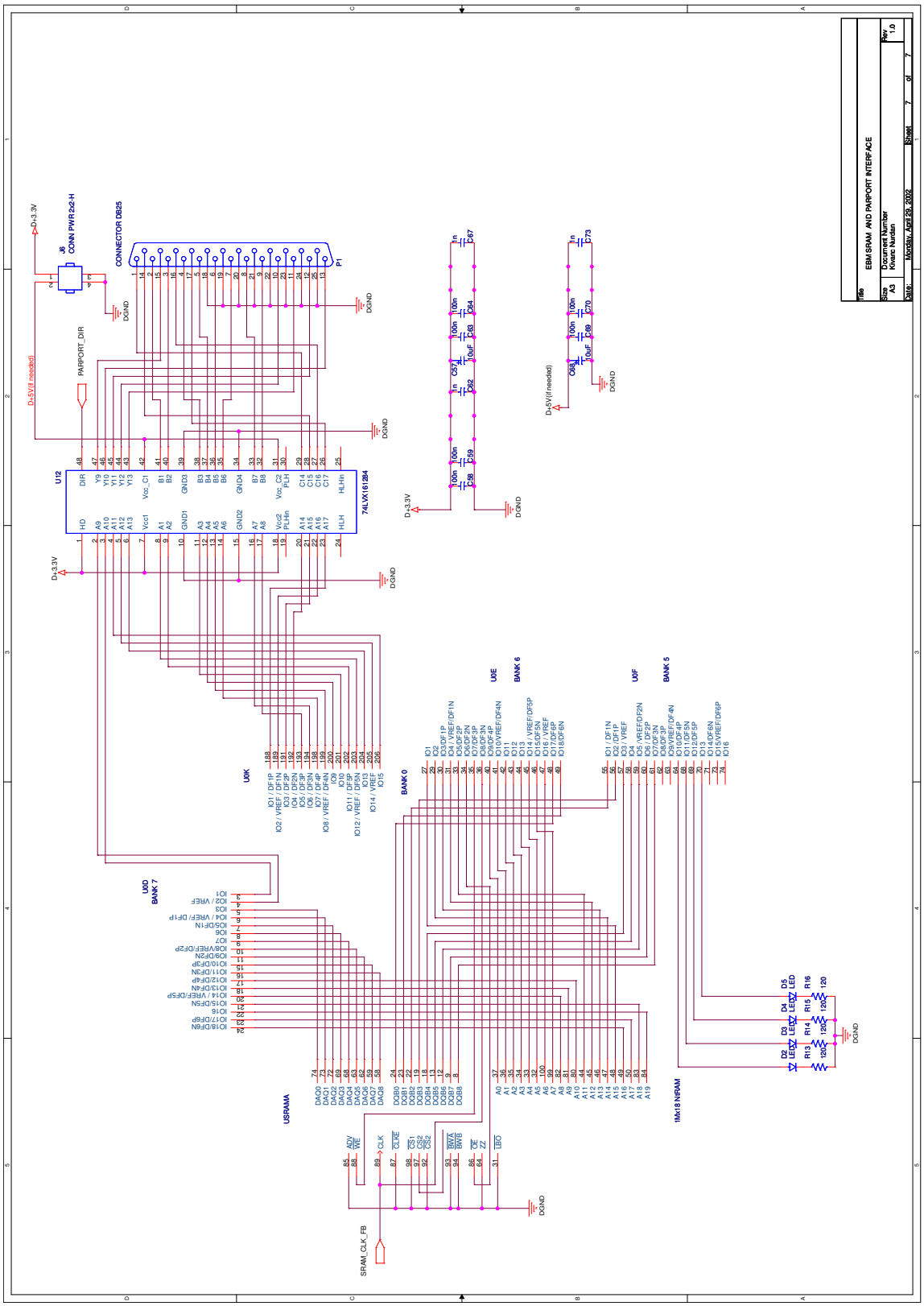

Fig. D.14: Event builder module 2MB SRAM and parallel port interface interface

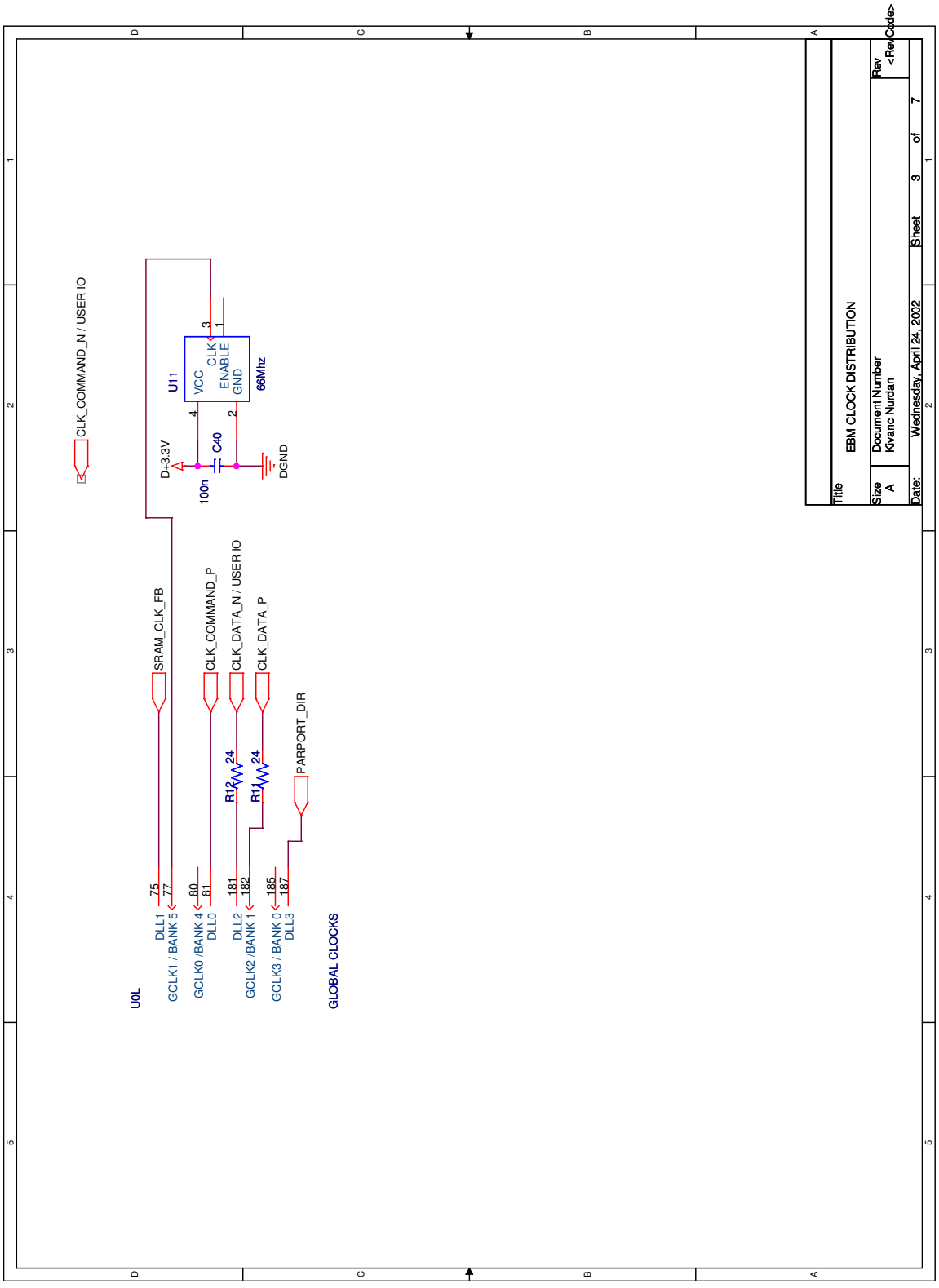

Fig. D.15: Event builder module clock distribution

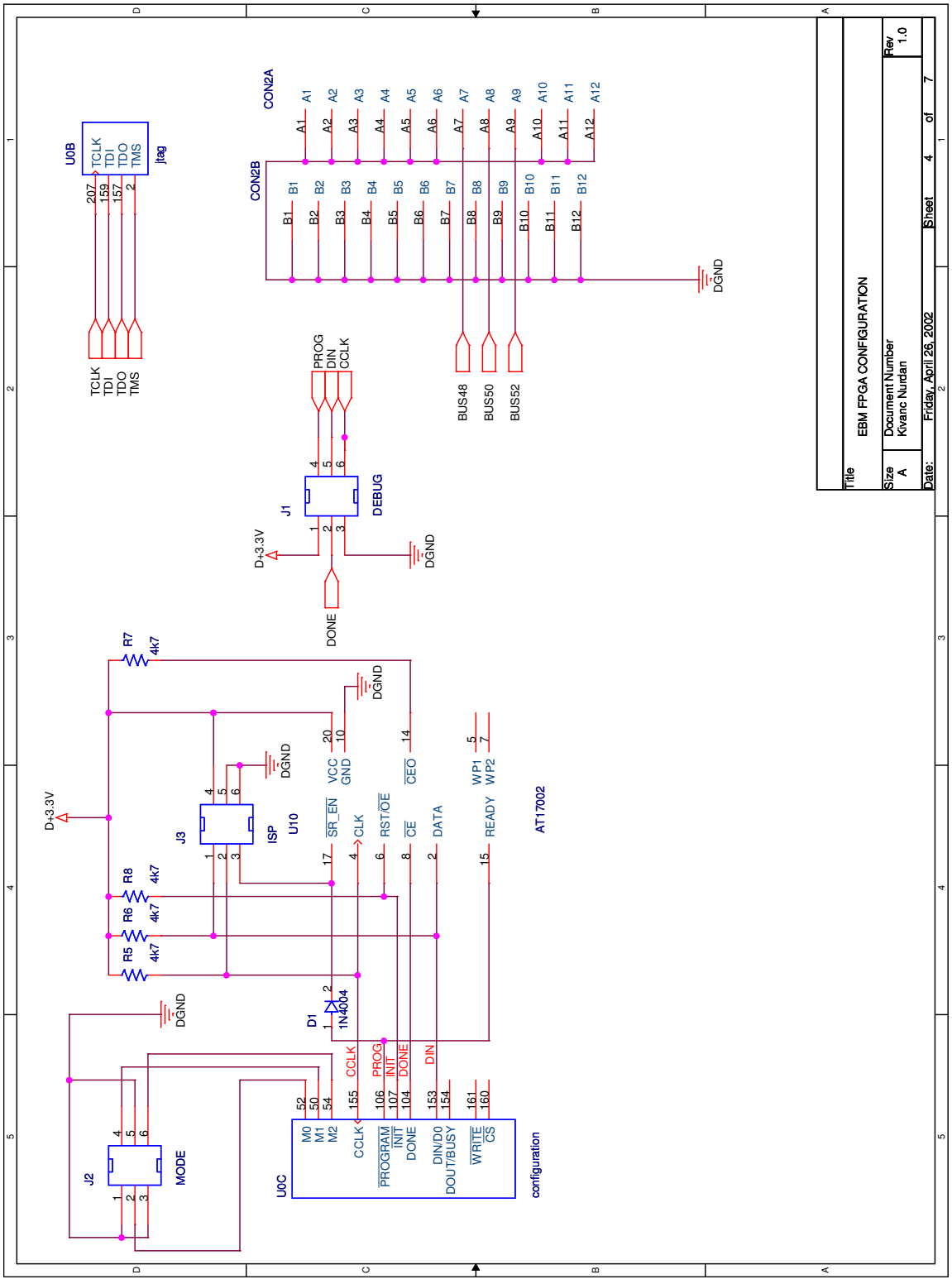

Fig. D.16: Event builder module FPGA configuration EEPROM

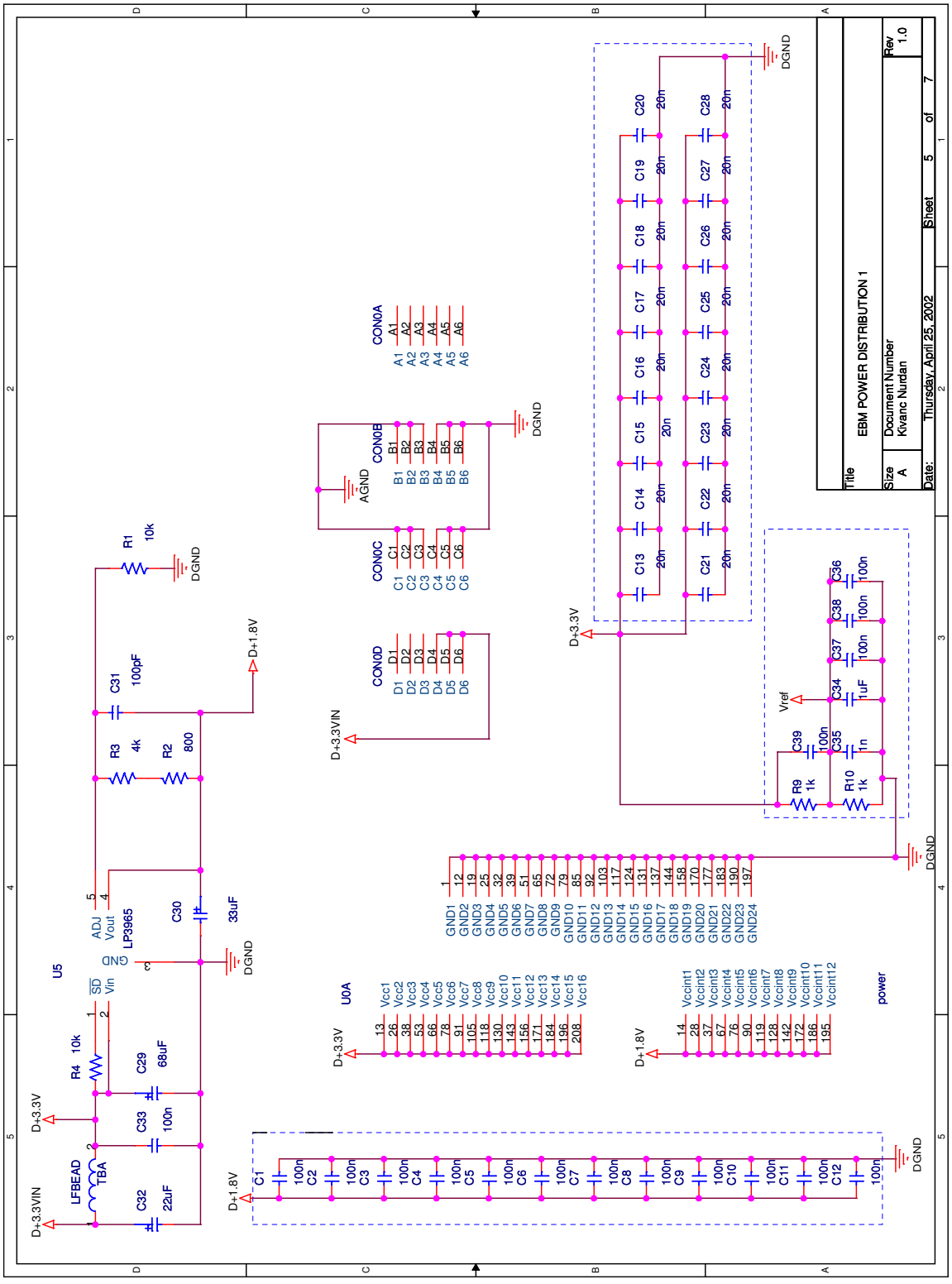

Fig. D.17: Event builder module power distribution I

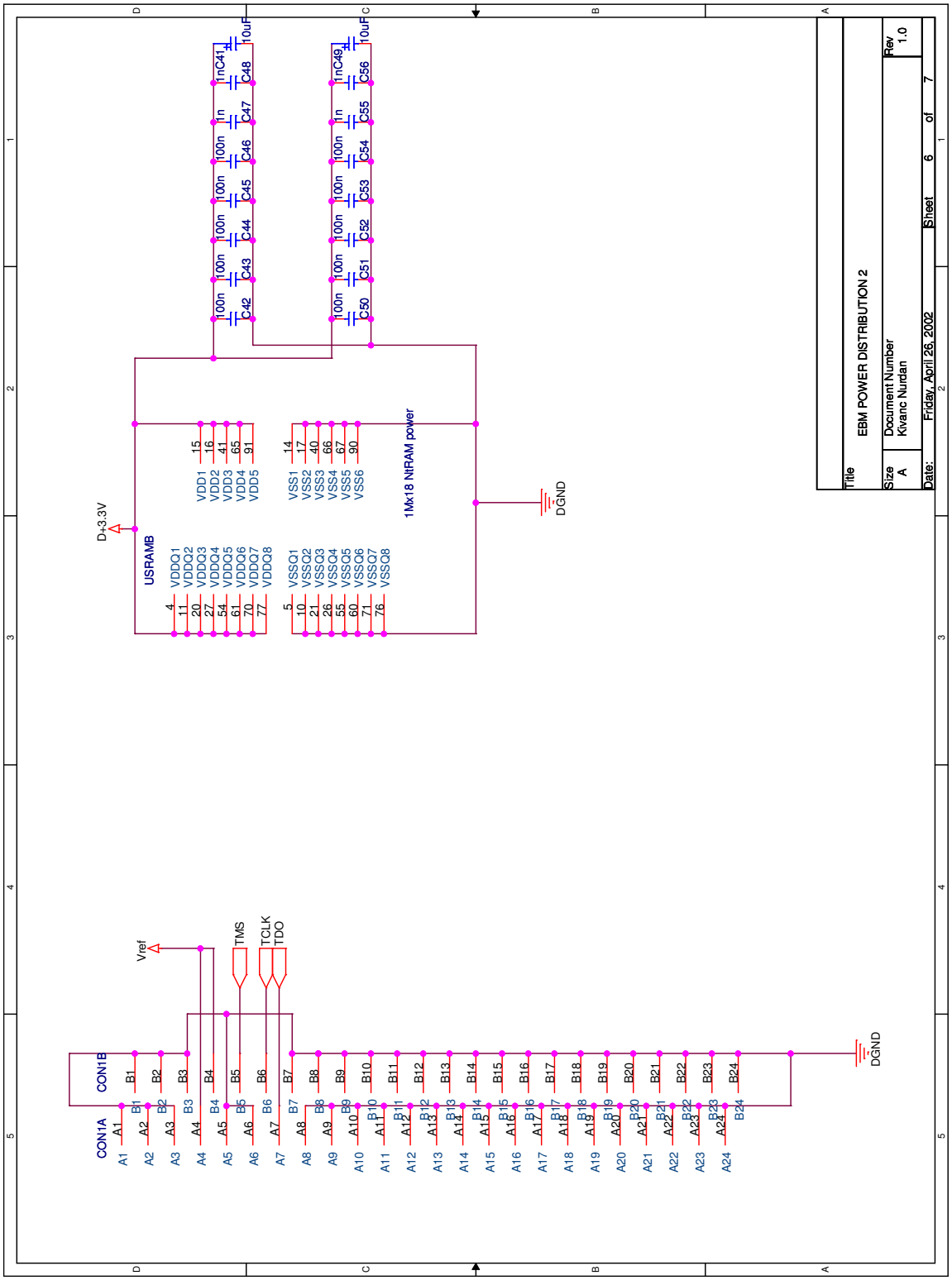

Fig. D.18: Event builder module power distribution II

Acknowledgments

This work was carried out at the Department of Physics in Siegen University. I wish to express my gratitude to electronics and mechanical workshops for the facilities and the help provided as well as their encouragement during my work.

I am most grateful to my supervisor Professor A. H. Walenta. His immense knowledge of physics as well as electronics played a great role during design and implementation stages of the Compton camera prototype. His advices concerning the arrangements of the dissertation were highly valuable.

I wish to express my gratitude to the official referees of the dissertation. I thank Prof. B. Freisleben and Prof. O. Loffeld for their friendly comments and constructive criticism on my work as well as some noteworthy and fascinating ideas for further research subjects.

I owe to my warmest gratitude to Prof. N. Pavel with whom we have spent many inspiring moments. He has taught me that scientific research can be not only rewarding and creative, but also fun.

I also warmly thank my friends and colleagues in our group: A. Brombach, D. Gebauer, D. Junge, A. Pepper. Very special thanks to M. Adamek for giving me the first trigger to enter the field of FPGAs and for numerous fruitful discussions. I am much grateful to Alan Rudge for sharing his immense experience and knowledge in the field of analog electronics (black magic!) and for proof-reading my thesis.

This work was partially supported by CEASAR (Center of Advanced European Studies and Research). I would like to express my gratitude to Prof. Hoffmann for enabling this support and also other colleagues from CAESAR for a nice working atmosphere.

I am forever indebted to my parents and my parents-in-law for their understanding, endless patience and encouragement when it was most required.

Finally, I owe my warmest thanks to “my female team”, my wife Tuba and our daughter Nurperi. My wife Tuba has encouraged me throughout the whole course of my work both scientifically and spiritually. The presence of this invaluable team has allowed me to keep my foot always firmly on the ground.

This work is dedicated to my only partner unique Tuba, the most precious light of my life Nurperi and my dear parents Doğan and Günal.

Bibliography

[AD] Analog Devices. `http://www.analog.com/`.

[Ang58] H. Anger. Scintillation Camera. *Review of Scintific Instruments*, vol. 29(3):pp. 27–33, 1958.

[ATM] Atmel Corporation. `http://www.atmel.com/`.

[Bec02] F. Beck, I. Piqueras, E. Pachoud, G. Duchêne, O. Dorvaux, P. Medina, and C. Ring. An alternative γ-tracking method using the Compton-scattering probability. In *Nuclear Structure with Large -arrays: Status and perspectives, NS 2002, Eur. Phys. J. A 20 (2004) 203*. Legnaro-Padova, Italy, 2002.

[Cas50] B. Cassen, L. Curtis, and C. Reed. A Sensitive Directional Gamma-Ray Detector. *Nucleonics*, vol. 6:pp. 78–80, 1950.

[Cas04] A. Castoldi, A. Galimberti, C. Guazzoni, L. Strüder, and A. Walenta. New Silicon Drift Detector Design for High Resolution Compton Cameras for Radiopharmaceuticals Mapping. In *IEEE Nuclear Science Symposium and Medical Imaging Conference NSS-MIC 2004, N45-7*. Rome, Italy, 2004.

[Ch.96] Ch. Gauthier and J. Goulon and E. Moguiline and A. Rogalev and P. Lechner and L. Strüder and C. Fiorini and A. Longoni and M. Sampietro and H. Besch and R. Pfitzner and H. Schenk and U. Tafelmeier and A. Walenta and K. Misiakos and S. Kavadias and D. Loukas. A High Resolution, 6 Channels, Silicon Drift Detector Array with Integrated JFET's Designed for XAFS Spectroscopy: First X-ray Fluorescence Excitation Spectra Recorded at the ESRF. *Nucl Instr Meth A*, vol. 382:pp. 524–532, 1996.

[Chi04] I. Chiosa. *New Implementation of a Compton Camera Image Reconstruction Algorithm for Biomedical Applications*. Master's thesis, University of Siegen, 2004.

[ÇN02] T. Çonka-Nurdan, K. Nurdan, F. Constantinescu, B. Freisleben, N. Pavel, and A. Walenta. Impact of the Detector Parameters on a Compton Camera. *IEEE Trans Nucl Sci*, vol. 49(3):pp. 817–821, Jun 2002.

[ÇN04a] T. Çonka-Nurdan. *High Resolution Measurements with Silicon Drift Detectors for Compton Camera Applications*. Ph.D. thesis, University of Siegen, 2004.

[ÇN04b] T. Çonka-Nurdan, K. Nurdan, K. Laihem, A. Walenta, C. Fiorini, B. Freisleben, N. Hörnel, N. Pavel, and L. Strüder. Preliminary Results on Compton Electrons in Silicon Drift Detector. *IEEE Trans Nucl Sci*, vol. 51(5):pp. 2526–2532, 2004.

[ÇN04c] T. Çonka-Nurdan, K. Nurdan, A. Walenta, H. Besch, C. Fiorini, B. Freisleben, and N. Pavel. Silicon Drift Detector Readout Electronics for a Compton Camera. *Nucl Instr Meth A*, vol. 523:pp. 435–440, 2004.

[Dai74] J. C. Dainty. *Image science*. Academic Press, London [u.a.] , 1974.

[Dor82] D. Doria and M. Singh. Comparison of Reconstruction Algorithms for an Electronically Collimated Gamma Camera. *IEEE Trans on Nucl Science*, vol. NS-29:pp. 447–451, Feb 1982.

[Eva82] R. D. Evans. *The Atomic Nucleus*. Robert E. Krieger Publishing Company, Malabar, Florida, Reprint edition of 1972 14th edn., 1982.

[Far83] W. Farr and G. Smith. Emitter followers and source followers as low noise pre-amplifiers for gas proportional detectors. *Nucl Instr Meth*, vol. 382:pp. 159–167, 1983.

[Gat84] E. Gatti and P. Rehak. Semiconductor Drift Chambers - An Application of a Novel Charge Transport Scheme. *Nucl Inst Meth in Phys Res*, vol. 225:pp. 608–614, 1984.

[Geb90] M. Gebser. *Messung der Ejektionsrichtung von Compton-Elektronen fuer die Bildrekonstruktion mit einer Compton-Kamera nach dem TEC-Prinzip*. Ph.D. thesis, University of Siegen, 1990.

[Gor74] R. Gordon. A Tutorial on ART. *IEEE Trans Nucl Sci*, vol. NS-21:pp. 78–93, Jun 1974.

[Gun03] D. Gunter. Filtered Backprojection Algorithms for Compton Cameras in Nuclear Medicine. *submitted to IEEE Transactions on Medical Imaging*, 2003.

[Hon00] A. Honma. CERN, personal communication, Oct 2000.

[Hua00a] C. Hua. *A Compton Imaging System Development and Performance Assessment*. Ph.D. thesis, University of Michigan, 2000.

[Hua00b] C. Hua, J. LeBlanc, N. Clinthorne, T. Kragh, S. Wilderman, and W. Rogers. A Data Acquisition System for a Ring Compton Camera. In *IEEE Nuclear Science Symposium and Medical Imaging Conference NSS-MIC 2000*. Lyon, France, 2000.

[ICR94] Particle counting in radioactivity measurements. ICRU Report 52, International Commision on Radiation Units and Measurements, 7910 Woodmont Avenue, Bethesda, Maryland 20814, U.S.A., Nov 1994.

[KET] KETEK GmbH Halbleiter- und Reinraumtechnik. `http://www.ketek.net`.

[Kno99] G. F. Knoll. *Radiation Detection and Measurement*. John Wiley & Sons, Inc., New York, USA, third edn., 1999.

[LeB99] J. LeBlanc. *A Compton Camera for Low Energy Gamma-Ray Imaging in Nuclear Medicine Applications*. Ph.D. thesis, University of Michigan, 1999.

[Lu05] J. Lu. *Coordinate Calibration of the Anger Camera for Compton Camera Measurements*. Master's thesis, University of Siegen, 2005.

[Mar93] J. Martin, G. Knoll, D. Wehe, N. Dogan, V. Jordanov, and N. Petrick. A Ring Compton Scatter Camera for Imaging Medium Energy Gamma Rays. *IEEE Trans Nucl Sci*, vol. 40:pp. 972–978, Aug 1993.

[Mat98] M. Matsumoto and T. Nishimura. Mersenne twister: A 623-dimensionally equidistributed uniform pseudorandom number generator. *ACM Trans on Modeling and Computer Simulations*, vol. 8:pp. 3–30, Jan 1998.

[MPI] Max-Planck-Institute Semiconductor Laboratory. `http://www.hll.mpg.de`.

[Mue73] J. Mueller. Dead-Time Problems. *Nucl Instr Meth*, vol. 112:pp. 47–57, 1973.

[Nat] National Semiconductor. `http://www.national.com/`.

[Nur03a] K. Nurdan, H. Besch, T. Çonka-Nurdan, B. Freisleben, N. Pavel, and A. Walenta. Development of a Compton Camera Data Acquisition System Using FPGAs. In *Proceedings of ISPC (International Signal Processing Conference)*. Dallas, USA, 2003.

[Nur03b] K. Nurdan, T. Çonka-Nurdan, H. Besch, B. Freisleben, N. Pavel, and A. Walenta. FPGA Based Data Acquisition System for a Compton Camera. In *Proceedings of SAMBA II (Symposium on Applications of Particle Detectors in Medicine, Biology and Astophysics)*, vol. 510, pp. 122–125. Nucl. Instr. Meth. A, Trieste, Italy, May 27-29, 2002, 2003.

[Opp89] A. V. Oppenheim and R. W. Schafer. *Discrete-Time Signal Processing*. Prentice Hall, New Jersey, 1989.

[Ort04] A. Orthen, H. Wagner, S. Martoiu, H. Amenitsch, S. Bernstorff, H. Besch, R. Menk, K. Nurdan, M. Rappolt, A. Walenta, and U. Werthenbach. Development of a two-dimensional virtual pixel X-ray imaging detector for time-resolved structure research. *J Synchrotron Rad*, vol. 11:pp. 287–301, 2004.

[Par00] L. Parra. Reconstruction of Cone-Beam Projections from Compton Scattered Data. *IEEE Trans Nucl Sci*, vol. NS-47:pp. 1543–1550, 2000.

[Pau02] J. Pauli, E. Pauli, and G. Anton. ITEM - QM Solutions for EM Problems in Image Reconstruction Exemplary for the Compton Camera. *Nucl Instr Meth A*, vol. 488:pp. 323–331, 2002.

[Pro04] D. Protić, E. Hull, T. Krings, and K. Vetter. Large-Volume Si(Li) Orthogonal-Strip Detectors for Compton Effect Based Instruments. In *IEEE Nuclear Science Symposium and Medical Imaging Conference NSS-MIC 2004, N16-197*. Rome, Italy, 2004.

[Rog88] W. Rogers, N. Clinthorne, L. Shao, P. Chiao, Y. Ding, J. Stamos, and K. Koral. SPRINT II: A Second Generation Single Photon Ring Tomograph. *IEEE Transactions on Medical Imaging*, vol. 7(4):pp. 291–297, Dec 1988.

[Sam] Samsung Semiconductor. `http://www.samsung.com/Products/Semiconductor/`.

[San88] H.-J. Sanden. *Die physikalischen Grundlagen der Energieauflösung einer Time Expansion Chamber (TEC)*. Ph.D. thesis, University of Siegen, 1988.

[Sau98] A. Sauve, A. Hero, W. Rogers, and N. Clinthorne. Hemispherical Spatial Sampling Study and 3-D Image Reconstruction using Statistical Iterative Algorithms for a Compton SPECT Camera Model. In *IEEE Nuclear Science Symposium and Medical Imaging Conference NSS-MIC 1998*. Toronto, Ont., Canada, 1998.

[Sch73] V. Schönfelder, A. Hirner, and K. Schneider. A Telescope for Soft Gamma Ray Astronomy. *Nuclear Instruments and Methods*, vol. 107:pp. 385–394, 1973.

[Sin83] M. Singh. An Electronically Collimated Gamma Camera for Single Photon Emission Computed Tomography. Part I: Theoretical Considerations and Design Criteria. *Medical Physics*, vol. 10(4):pp. 421–427, Jul/Aug 1983.

[Sin84] M. Singh and D. Doria. Germanium-Scintillation Camera Coincidence Detection Studies for Imaging Single Photon Emitters. *IEEE Trans Nucl Sci*, vol. NS-31:pp. 594–598, Feb 1984.

[Str98] L. Strüder, P. Lechner, and P. Leutenegger. Silicon Drift Detector - the key to new experiments. *Naturwissenschaften*, vol. 85:pp. 539–543, 1998.

[Str00] Strueder. NN. In *Proceedings of SAMBA (Symposium on Applications of Particle Detectors in Medicine, Biology and Astophysics)*. Nucl. Instr. Meth. A, Siegen, Germany, May 27-29, 1999, 2000.

[Tod74] R. Todd, J. Nightingale, and D. Everett. A Proposed γ Camera. *Nature*, vol. 251:pp. 132–134, Sep 1974.

[Wal81] A. Walenta and A. Brill. Project presentation to DOE at Rockville Program Review Meeting, 1981.

[Wil98] S. Wilderman, N. Clinthorne, J. Fessler, and W. Rogers. List Mode Maximum Likelihood Reconstruction of Compton Scatter Camera Images in Nuclear Medicine. *IEEE Trans Nucl Sci*, vol. 45:p. 957, 1998.

[Xil] Xilinx. `http://www.xilinx.com/`.

[Yu00] D. Yu and J. Fessler. Mean and Variance of Singles Photon Counting with Deadtime. *Phys Med Biol*, vol. 45:p. 2043, 2000.

[Yu02] D. Yu and J. Fessler. Mean and Variance of Coincidence Counting with Deadtime. *Nucl Instr Meth A*, vol. 488:pp. 362–374, 2002.

Index